Ferrule-top micromachined devices

A UNIVERSAL PLATFORM FOR OPTOMECHANICAL SENSING

Grzegorz Leszek Gruca

Reading committee:

prof.dr. Luigi Zeni, Second University of Naples (Italy)
prof.dr. Pasqualina Sarro, Delft University of Technology (The Netherlands)
prof.dr. Ole Bang, Technical University of Denmark (Denmark)
dr. Freek Ariese, VU University Amsterdam (The Netherlands)
dr. Yves Bellouard, Technische Universiteit Eindhoven (The Netherlands)

Cover design: Jakup Kwap & Agnieszka Gruca

Printed by: Ipskamp Drukkers

This work was supported by the European Research Council under the European Communitys Seventh Framework Programme (FP7/2007-2013)/ERC grant agreement number 201739.

Vrije Universiteit
Faculty of Sciences
Department of Physics and Astronomy
Condensed Matter Physics
De Boelelaan 1081
1081 HV Amsterdam
The Netherlands

ISBN XXX-XXX-XXX-XXX

VRIJE UNIVERSITEIT

Ferrule-top micromachined devices

A UNIVERSAL PLATFORM FOR OPTOMECHANICAL SENSING

ACADEMISCH PROEFSCHRIFT

ter verkrijging van de graad Doctor aan
de Vrije Universiteit Amsterdam,
op gezag van de rector magnificus
prof.dr. F.A. van der Duyn Schouten,
in het openbaar te verdedigen
ten overstaan van de promotiecommissie
van de Faculteit der Exacte Wetenschappen
op donderdag 20 februari 2014 om 13.45 uur
in de aula van de universiteit,
De Boelelaan 1105

door

Grzegorz Leszek Gruca

geboren te Wałbrzych, Polen

promotor:	prof.dr. D. Iannuzzi

Contents

Chapter 1

Introduction

Human beings are an exceptional example of creatures driven by curiosity [1]. We, as a species, have an insatiable hunger of knowledge that is manifested by the ability of asking uncountable numbers of questions regarding the surrounding world. Some of these questions can be answered nowadays, the answer for others is not even close. What is interesting, very often new questions arise as a consequence of answering others. To deal, at least partially, with this self-propelling process, mankind needs to create adequate tools able to efficiently and unambiguously describe a considered issue, problem or phenomenon. One of them is metrology - a science directly connected with practical and theoretical aspects of describing reality. Metrology is a very broad field and it is difficult to briefly describe all its aspects. Nevertheless, one can undoubtedly indicate a common feature: metrology is a science about measurements. Measurements provide the basis of our knowledge. Their accuracy, precision and other properties are limiting our cognitive abilities and set boundaries to the available knowledge. Therefore it is in our best interest to move these boundaries further by improving existing sensors, developing new ones and upgrading measurement techniques. Of course, we will face some fundamental problems and limitations [2]. Nevertheless, they should not discourage us from further improvements that are helping us to better understand the nature of physical phenomena and the surrounding world. As a great example of this process, illustrated by a tremendous progress in development of new sensors and techniques, one can indicate a broad family of optical sensors.

Over the last few decades, optical sensors have been dynamically spreading among different areas of science [3, 4]. By measuring properties of light, such as amplitude, phase, wavelength or polarisation, one can build a wide range of transducers able to transform a physical quantity into an electric signal. Some of the sensors are simple and commonly used in everyday life (like the photoresistors mounted in mobile phones); others require elaborated setups and millions of dollars of investments (like the Laser Interferometer Gravitational-Wave Observatory - LIGO). Among the broad family of optical sensors one

- High sensitivity
- High resolution
- Remote operation
- High mechanical strength
- Simple multiplexing
- Wide dynamic range
- High accuracy
- Immunity to electromagnetic interference
- Passiveness
- High temperature resistance
- Distributed sensing
- Resistance to corrosion

Table 1.1: Main advantages of optical fiber sensors.

can distinguish a subgroup that has been recently receiving more and more attention: optical fiber sensors (OFS).

OFS are being developed since the early 70's, when the biggest obstacle to a widespread use of optical fibers (large attenuation of a fiber) was eliminated. Since then, thanks to their advantages (see Tab. 1.1), optical fiber sensors have become an interesting alternative to existing solutions in many scientific and industrial applications. Taking into account their sensing abilities one can distinguish three different groups.

Distributed fiber sensing is based on one of two phenomena present, among many others, during light propagation in optical fibers. By monitoring Raman or Brillouin scattering one can perform fully distributed measurements using standard fibers, unmodified at the fabrication stage. This unique feature is especially useful in monitoring large structures such as bridges, dams, dikes or pipelines, where a single fiber can provide up to thousands of measurement points over kilometers. Currently available measurement tools allow one to reach a millimeter spatial resolution, simultaneously providing temperature and strain resolution of about 0.1 ^{o}C and 2 $\mu\varepsilon$, respectively. One has to also mention that distributed optical sensing is the most dynamically growing part of the whole fiber optic sensors family.

Semi-distributed sensors are mainly based on Fiber Bragg gratings (FBG), which were introduced in 1978 [5]. Initially FBGs were used as an in-fiber optical filter, but researchers quickly realized that the sensitivity of the reflected/transmitted wavelength to the change of external parameters can be utilized for sensing purposes. A typical FBG consists of periodic longitudinal modulations of the refractive index in the fiber core. The period of the modulation defines the characteristic wavelength of the FBG, which can be measured by acquiring either a reflection or transmission spectrum. Any external disturbance (such as change in the temperature or stress) will influence the periodic pattern and thus the characteristic wavelength that can be measured. FBGs can be fabricated in a row along the same fiber. A typical number of FBGs interrogated by a single fiber readout unit varies from 20 to 100, depending on the technique used. The resolution in strain and temperature achieved by fused silica commercial systems can reach 1 $\mu\varepsilon$ and 0.1 ^{o}C, respectively.

The last group of sensors allows to perform measurements only in one specific point. An optical fiber is used as a link between the transducer, usually placed in a close vicinity of the end of the fiber, and an interrogation unit. A typical transducer consists of a Fabry-Perot cavity where the light is reflected between two parallel surfaces. Any change in the distance or refractive index of the medium between these surfaces will then cause a change in the sensor's output signal. This technology adapts well to applications where a limited number of sensors is required - typically between 1 and 10. Multiplexing capabilities can also be implemented when more sensing points are needed. Thanks to their excellence performance, in connection with the general advantages of all-optical devices (see Tab. 1.1), point sensors are the most common representative of the OFS family in industrial and medical applications.

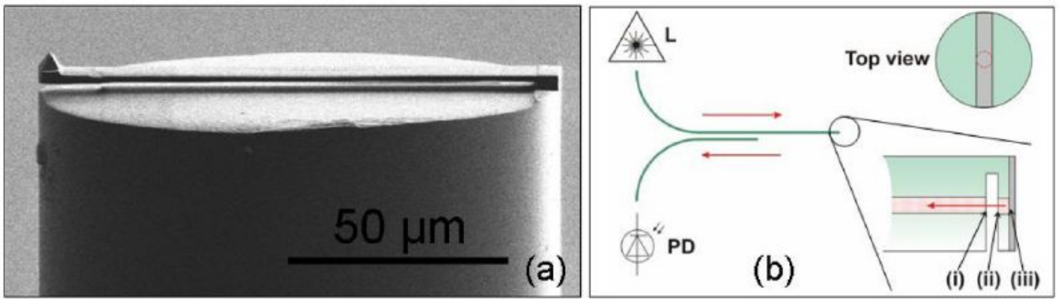

Figure 1.1: (a) Scanning electron microscope image of a fiber-top cantilever equipped with a pyramidal tip. (b) Schematic view of the readout apparatus: L=laser, PD=photodiode, (i)=fiber-to-air interface, (ii)=air-to-cantilever interface, (iii)=cantilever-to-air interface [6].

In 2006, our group proposed a new approach to combine a micromechanical cantilever and an optical fiber [7]. The new device, introduced as a *fiber-top* sensor (see Fig. 1.1), is a simple micro-electro-mechanical-system (MEMS) fabricated at the tip of a single-mode fiber. The fiber is used as a main building block of the sensor and provides the interrogation capability. Shortly after the release of the first paper a set of articles describing the technique in details and providing some examples of different fiber-top sensors was published [8–10]. The new approach presented by the authors have shown a great potential in sensing and monitoring and have become an interesting alternative for existing sensing solutions. Fiber-top devices, in fact, offer a set of unique advantages. A versatile all-optical readout allows one to use fiber-top sensors in almost all optically transparent environments. Since the readout is based on an interferometric technique that provides high sensitivity and resolution, fiber-top devices are capable of performing high quality measurements. Furthermore, they do not require any alignment and are ready to use directly after connecting them to the interrogation unit. This property makes them a fully plug-and-play solution for applications where any manipulation within the sensor is strongly unwanted or even impossible. It has been demonstrated that fiber-top technology can be successfully used as a hydrogen detector [11], refractometer [12] and probe for atomic force microscopy(AFM) [9]. However, despite all the advantages there is one issue that effectively hampered its further development. During the fabrication process a sophisticated technique, called focus ion beam (FIB) milling, has to be used. Both the accuracy and the precision provided by FIB are necessary to achieve a high quality fiber-top sensor. Unfortunately, this process is expensive and time consuming. Moreover, it is not suitable for series production (sensors have to be fabricated one by one without the possibility of batch processing).

To overcome this limitation, two different approaches have been proposed. Instead of using FIB milling during the fabrication one can try to combine glass etching and laser light exposure [13]. This procedure is faster, cost effective and adapt well to batch production. However, since the diameter of the laser beam is much larger than the diameter of the ion beam, the overall cutting resolution does not go beyond $\approx 5\mu$m, making the fabrication of high quality fiber-top transducers problematic. Additionally, the difference in the quality of the sensor surface obtained by etching (high roughness) with respect to FIB milling effectively deteriorates the signal received from the sensor and thus the performance. Since the method was not perfect, an alternative approach was suggested. Rather than by milling, the transducer can be fabricated using a photolithography process [14]. A new technology called *align-and-shine* photolithography provides the possibility of performing standard photolithography processes directly at the front facet of a cleaved optical fiber. The process, is still in the research phase and some additional efforts and experiments are required before the technology will reach a state where it could be systematically implemented. As a consequence of these drawbacks, some new ideas and different approaches had to be developed.

The new type of micromechanical sensors presented in this thesis was developed as a direct continuation of the research path started in 2006. These four years of development allowed us to introduce a new family of transducers and demonstrate their added value via a broad set of tests in different fields. The original idea of using fiber-top sensors was modified by scaling up to millimeter size devices. Instead of a transducer fabricated at the top an optical fiber, we proposed to carve the micromechanical structure out of a glass ferrule and employ the 125 μm fiber as a basis of the readout scheme. This new approach, named *ferrule-top* (FT) technology, offers numerous advantages. The fabrication procedure, based on picosecond laser ablation, can be performed in air without any additional steps. The overall dimensions of the sensor have increased therefore the limited accuracy of the ablation process is not anymore a problem. At the same time, the transducer has not lost any of the advantages characteristic for fiber-top point sensors (immunity to electromagnetic noise, remote and all-optical operation, easy to use). Furthermore, due to a larger area available for laser carving (typically 3×3 mm), fabrication of more complicated structures than a simple cantilever become possible. To fully understand the working principle of FT sensors a short introduction to mechanical properties of cantilevers and the readout scheme will be made in the next two subsections.

1.1 Micromechanical resonators

Micro-electro-mechanical transducers [15] have been providing a significant contribution to the development of new type of sensors. This trend is especially noticeable in the last decade, where high sensitivity and small dimensions are one of the main priorities during the design phase of new types of devices. As an example, one can consider a simple MEMS – a microcantilever, which become a universal platform used for various applications. The origins of using microcantilevers as transducers can be traced back to the mid 80's, when *Binnig, Auate and Gerber* introduced the first atomic force microscope (AFM)[16]. Since then, it has been proved that MEMS cantilevers are also a valuable platform for chemical and biological sensing [17, 18], with applications that range from explosives detection [19], DNA detection [20], diagnosis of prostate cancer [21] to glucose monitoring [21]. It has been further demonstrated that MEMS cantilevers can be used to monitor other parameters, including temperature [22], flow [23], or density and viscosity [24].

Typical MEMS cantilevers are made out of silicon, silicon dioxide, silicone nitride or polymer and have rectangular shape [25, 26] (see Fig. 1.2), with dimensions that vary from tens of nm to μm in thickness, tens to hundreds of μm in width, and μm to mm in length. Both factors, i.e. the type of a material and geometry, define the mechanical properties and thus the final performance of a cantilever based sensor.

Microcantilever based transducers can work in two different modes: static and dynamic. Depending on the nature of the quantity that has to be measured, one has to choose which mode is more suitable and will give a better response. The static mode is based on monitoring the deflection of the cantilever due to an external stimulus. By measuring the bending, one can infer the magnitude of the force acting on the probe. For small amplitudes, the bending is proportional to the force, which is typically applied at the tip of the cantilever (see Fig. 1.3a), and can be described using a simple equation:

$$F = k \cdot x \tag{1.1}$$

where F is the point force, x is the bending at the free hanging end and k corresponds to the spring constant. The spring constant is one of the most important parameters of a force transducer. In case of a simple rectangular

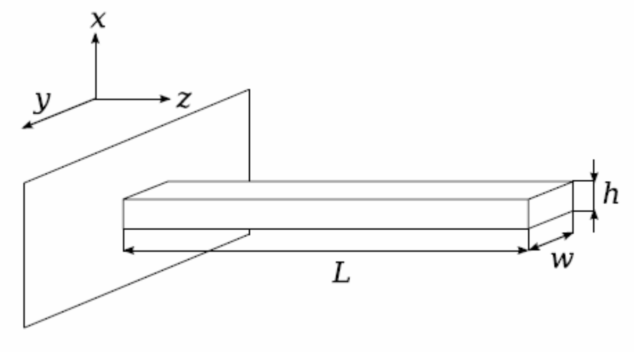

Figure 1.2: Schematic view of a simple rectangular cantilever [26].

beam as shown on Fig. 1.2 the spring constant can be defined as:

$$k = \frac{Ewh^3}{4L^3} \tag{1.2}$$

where E is the Young's modulus of the material the cantilever is made of. The spring constant of commercialised cantilevers range from ≈ 0.01 N/m (mostly used for biological applications) to several tens of N/m (mostly used for non-contact atomic force microscopy imaging). This wide range of values can be covered by scaling geometrical dimensions and changing the Young's modulus by choosing the proper cantilever material.

Static bending can be also induced by changes of the surface stress distribution along the beam - a phenomena that lies at the heart of many biochemical sensors [27, 28]. Those modifications are typically a result of molecule adsorption on the cantilever's surface or interactions between molecules and a previously coated selected sensing layer. By assuming two thin layers of negligible thickness that are covering the surface of the transducer as depicted on Fig. 1.3b, one can calculate the radius of curvature of the cantilever using the Stoney's formula[29]:

$$\frac{1}{R} = 6\left(\frac{1-\nu}{Eh^2}\right)(\Delta\sigma_1 - \Delta\sigma_2) \tag{1.3}$$

where ν is the Poisson's ratio of the cantilever material, $\Delta\sigma_1$ and $\Delta\sigma_2$ is the surface stress difference before and after the adsorption respectively at the top and bottom of the cantilever (see Fig. 1.3b). It is important to note that this equation ignores the clamping effect on the cantilever deformation and therefore introduces small errors. For an accurate measurement of the surface stress, more complete models have to be applied [30].

Every mechanical structure can be characterized in the frequency domain by acquiring a vibration spectrum. Detailed analysis of the signal then provides

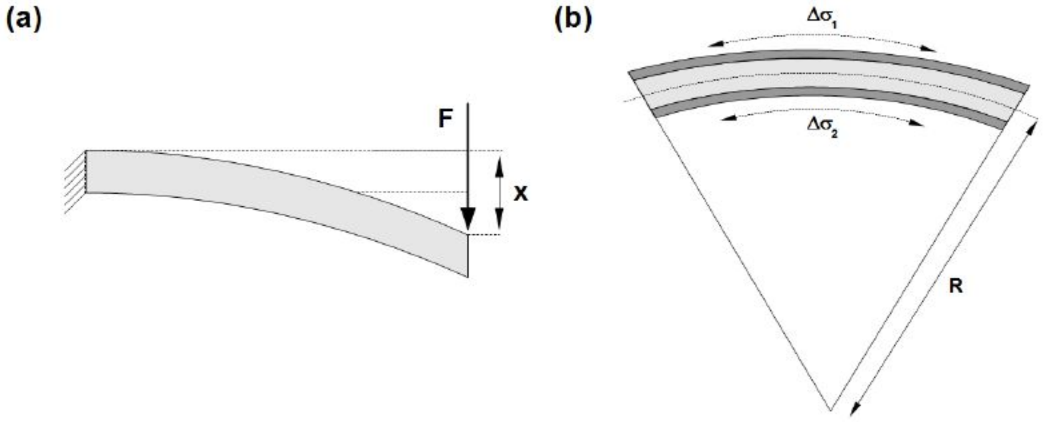

Figure 1.3: Schematic view of a cantilever bent by: (a) an external point force, (b) a modification of surface stress.

information on the properties of the structure and the surrounding environment. The dynamic measurement mode used in cantilever sensing techniques is based on monitoring changes in the dynamic parameters of the microcantilever. In first approximation, the vibrations of the microcantilever can be described using a harmonic oscillator model. However, to describe the nature of cantilever kinetics in a more precise way, one has to introduce an one-dimensional Euler-Bernoulli equation [31] (coordinate system according to Fig. 1.2):

$$EI\frac{\partial^4 g\left(z,t\right)}{\partial z^4}+\rho A\frac{\partial^2 g\left(z,t\right)}{\partial t^2}+\gamma\frac{\partial g\left(z,t\right)}{\partial t}=0 \tag{1.4}$$

where $g(z,t)$ is the cantilever displacement along the x-axis, ρ is the density of the cantilever material, $A=w\cdot h$ is the cross section area (xy plane), $I=\frac{wh^3}{12}$ is the moment of inertia along the y-axis, and γ is the damping coefficient. The damping coefficient can be expanded as:

$$\gamma=\frac{\omega\rho A}{Q} \tag{1.5}$$

where ω is the oscillation frequency and Q is the quality factor. Assuming that the cantilever is homogenous, isotropic and its deformation is fully elastic, one can separate the variables and solve the characteristic equations. As a result of these operations, a modal shape function and resonance frequency of each mode can be obtain. The resonance frequencies can be calculated from:

$$\omega_n=\alpha_n^2\sqrt{\frac{EI}{\rho A}} \tag{1.6}$$

where α_n is a dimensionless parameter calculated from the time dependent equation. The first four flexural modes along with their resonance frequencies

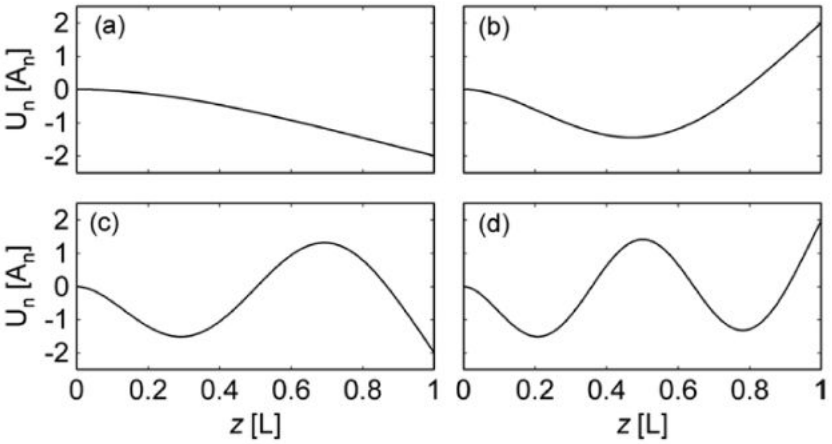

Figure 1.4: Schematic shape of the first four flexural modes of a rectangular cantilever [26]: (a) the fundamental mode with resonance frequency f_0; (b),(c) and (d) consecutive modes with resonance frequency respectively equal to: $6.27 \cdot f_0$, $17.55 \cdot f_0$ and $34.39 \cdot f_0$. The origin corresponds to the base of the cantilever.

are reported in Fig. 1.4. As one can notice from Eq. 1.5, the resonance frequency and quality factor are directly coupled to the damping coefficient. It is thus evident that any variation of the damping caused by a change in the viscosity or density of surrounding gas or an additional external force will modify these quantities. Additionally, a small mass added to a vibrating cantilever or any modification of the surface stress will also affect their values. One can thus use those phenomena to build a number of different micromechanical sensors.

Ferrule-top cantilevers can be used in both static and dynamic mode. One has to choose which is more suitable for a particular application. For topography measurements, a natural solution is to operate the prong in static mode, while for adsorption based measurements more effective operation can be achieved by following the resonance frequency of the cantilever. In some cases the two modes can be combined to achieve better performance, as we will illustrate in the next chapters.

1.2 Interferometric readout

Choosing an optimal readout scheme requires a careful look into a set of parameters (e.g. signal-to-noise ratio, dynamic range, linearity), which are crucial for the final performance of the sensor. Providing an efficient readout mechanism can potentially extend the application range of the sensor connected to it. The overall performance however is not the only parameter worth to consider. One can find examples where a readout mechanism, although very effective, did not spread outside the walls of research laboratories [32–34]. This phenomenon is often caused by the lack of technical skills and expertise among non-laboratory personnel who are not used to operate complicated setups. Alignment and calibration, for example, are typical procedures that go beyond what the final users of the sensor is willing to accept. An ideal readout should therefore not only be sensitive, accurate, stable but also easy to use.

Ferrule-top devices can act as sensors that are able to transform a physical or chemical quantity into a useful electrical signal. The fundamental principle lying at the heart of these sensors is based on monitoring minute movements of the micromechanical structure fabricated at the top of a ferrule. Taking into account the magnitude of the bending and considering the fact that the optical fiber can be easily integrated within the sensor, an implementation of an interferometric technique seems to be the optimal solution. The accuracy of the interferometer can then be provided by a stable, well defined wavelength and intensity of the laser used as a light source. All additional effects disturbing the overall performance can be minimized by a proper design of the transducer and of the interferometer itself. During the design phase one should take into account the environmental conditions of operation, including temperature variations and vibrations. All of them are directly connected with the final resolution of the setup. It has been demonstrated that an accurately designed fiber optic interferometer allows one to achieve readout resolution well below 1 nm over tens of kHz bandwidth [35]. In case of ferrule-top interferometric readout, the requirement of being easy-to-use is also fulfilled. Since the alignment is given by the design of the sensor there is no need of further manipulation of any of the components. Only the calibration has to be performed by the user. This procedure, however, is easy to perform. Therefore a fiber based interferometer fulfills almost all requirements characteristic for an ideal ferrule-top readout unit.

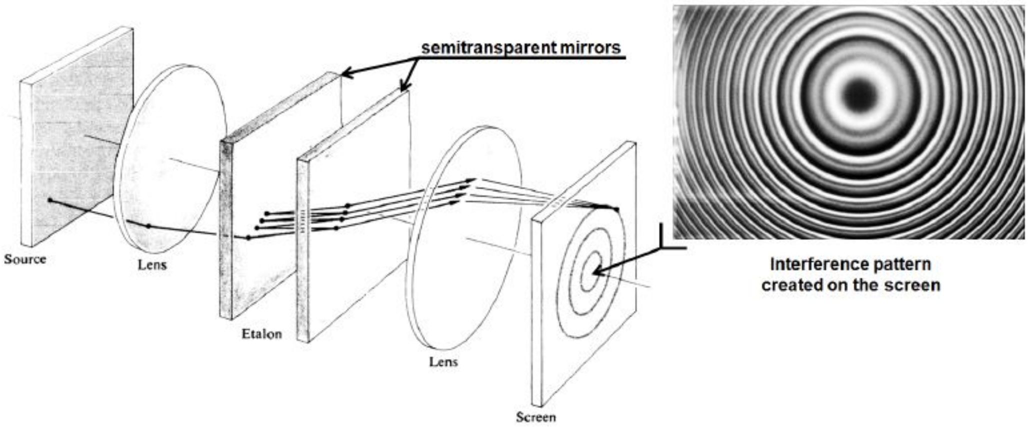

Figure 1.5: Illustration of a simple Fabry-Perot interferometer [36]

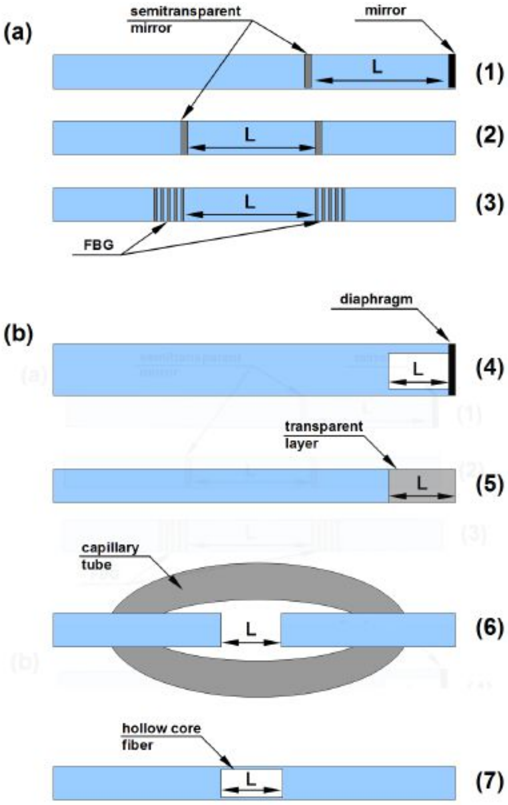

Figure 1.6: Different types of (a) intrinsic and (b) extrinsic Fabry-Perot sensors [37]: (1) cavity formed by an internal mirror and fiber end; (2) cavity formed by two internal mirrors; (3) cavity formed by two fiber Bragg gratings; (4) cavity formed by fiber and diaphragm; (5) cavity formed by thin polymer film on the end of a fiber; (6) cavity formed by two aligned fibers; (7) cavity formed by single-mode fiber ends spliced to a hollow-core fiber. In each case L is the length of the cavity.

A typical Fabry-Perot interferometer (FPI), called also FP etalon, is a simple device that consists of two parallel semitransparent mirrors [36, 38, 39]. The mirrors form an optical cavity where multiple light reflections occurs (see Fig. 1.5). The light that leaves the cavity forms a characteristic pattern caused by constructive or destructive interference. Analysing the pattern for a well known wavelength, allows one to determine the absolute size of the cavity.

In a fiber based FPI, the cavity can be created within the fiber or just next to it. Based on this criteria we can distinguish two families of sensors (see Fig. 1.6). Intrinsic FPI sensors are typically fabricated by splicing different types of fibers or fibers that are modified by etching or additional coating. One can also form a large FP cavity between fiber brag gratings operating at the same wavelength. Extrinsic FPI sensors are more diverse since the fiber is used

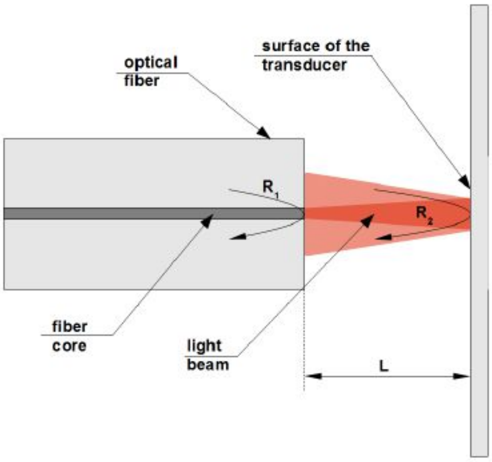

Figure 1.7: Schematic view of the light propagation between the fiber and the surface of the FT transducer. Since the FP cavity is formed outside the optical fiber, all FT devices are classified as external cavity sensors.

only as a host to guide the light to and from an external cavity. These types of sensors are more flexible and accommodate better for specific applications since the cavity can be tailored to a particular application. In both kind of sensors any change of dimensions or refractive index within the cavity caused by temperature, pressure, strain or other factor can be detected by monitoring the interference signal.

Ferrule-top devices are an external cavity FPI sensors. The cavity is formed between the cleaved end of the optical fiber and the surface of the micromechanical structure (see Fig.1.7). Part of the light is reflected from the fiber-to-air interface (Fresnel reflection) and creates the first interfering beam. The second beam is formed by the light reflected from the bottom surface of the transducer, which is coupled back into the fiber. The interference pattern formed by the two beams can be described by [40]:

$$I(\lambda) = I_0 f(\lambda)\,\alpha(\lambda)\,\frac{R_1 + \eta^2 R_2 - 2\eta\sqrt{R_1 R_2}cos\left(\frac{4\pi n(\lambda)L}{\lambda}\right)}{R_1 + \eta^2 R_1 R_2 - 2\eta\sqrt{R_1 R_2}cos\left(\frac{4\pi n(\lambda)L}{\lambda}\right)} \tag{1.7}$$

where λ corresponds to wavelength, I_0 is the intensity of the light source, $f(\lambda)$ is the spectral characteristic of the light source, $\alpha(\lambda)$ is the cavity absorption coefficient, R_1 and R_2 are respectively reflection coefficients from fiber-to-air interface and surface of the transducer, $n(\lambda)$ is the refractive index of the medium inside the cavity, L is the size of the cavity, and η is the coupling efficiency which is a direct consequence of the geometrical dimensions of the probe and can be calculated by [41]:

$$\eta = \frac{1}{\left[1 + \left(\frac{2\lambda L}{2\pi n(\lambda) w^2}\right)^2\right]} \tag{1.8}$$

where w is the mode field diameter of the optical fiber. Equation 1.7 can be simplified by assuming $R_1 = R_2$ (an influence of superimposed effects that come from light reflection and geometrical conditions) and neglecting the spectral dependence of all parameters. Under low finesse conditions [37], where the reflectivity of both interfaces is so low that multiple reflections can be neglected, one can finally describe the intensity at the output of the interferometer by:

$$I\left(\lambda\right) = I_0 \alpha R \left[1 + \eta^2 - 2\eta cos\left(\frac{4\pi n_0 L}{\lambda}\right)\right] \tag{1.9}$$

As one can easily notice the output has a periodic nature due to consecutive constructive and destructive interference. A single period of $\frac{4\pi n_0 L}{\lambda}$ is called *a fringe.*

To keep track of the interference signal (fringes) one should use an optimal scheme [37] tailored to each particular application. The most popular redout method is based on the use of a laser. Laser beams, thanks to their long coherence length, allow one to achieve high resolution measurements over short and long distances. To optimize the sensitivity of a laser based interrogation system, one has to work in close vicinity of the quadrature point (see Fig. 1.8), where a linear approximation of the interferogram can be locally applied. In that configuration, the dynamic range available to the user is typically limited to half of a fringe. To extend it, one has to eliminate the problem of fringe ambiguity. The most popular solutions are based on fringe counting, heterodyne detection or subcarrier demodulation [42] which extend the working range to multiple fringes. Readout schemes based on low coherence light sources, e.g. superluminescent diodes (SLD), can also be implemented for applications where smaller cavities have to be demodulated. Thanks to their broad spectrum, which has to be measured during the cavity interrogation, the latter are not limited to a single fringe operation and their sensitivity does not depend on the initial working point. Additionally, they allow one to measure the absolute size of the cavity. Despite all advantages, low coherent light sources in comparison with lasers, provide a moderate sensitivity and are typically used in less demanding applications.

In all applications listed in the thesis we have been using a laser as a light source. In most cases, the FT fabrication process does not provide an accuracy needed to obtain quadrature operation. Therefore, it is important to tune the wavelength of the laser and match the quadrature condition before performing measurements. This approach allowed us to reach a typical readout resolution below 1 nm for 20 kHz bandwidth.

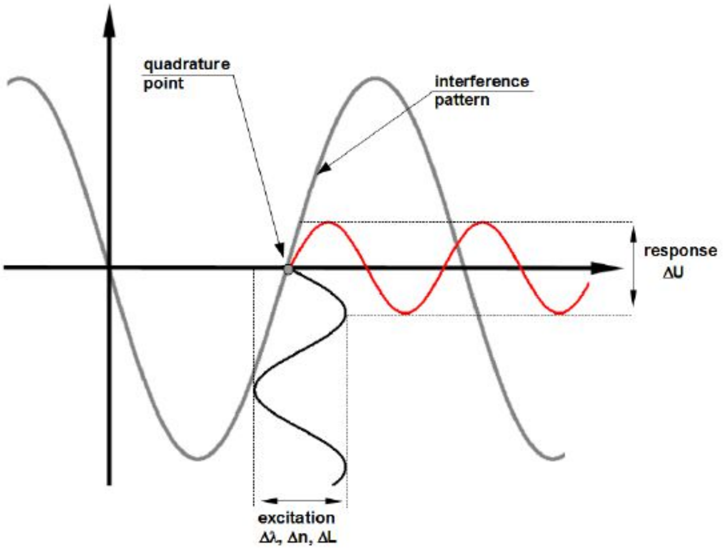

Figure 1.8: Schematic view of signal transformation in ferrule-top sensors employing FPI interrogation with laser light source. Any variation of the laser wavelength, refractive index or length of the cavity causes a change in the interferometric signal.

1.3 Outline of the thesis

This thesis focuses on ferrule-top optomechanical sensing. It illustrates the process of evolution of FT technology and shows its versatility via a series of very diverse experiments. All following chapters are based on papers that have been published during the period of study. The structure of the thesis is organized as follow:

Chapter 2 presents a first FT transducer fabricated out of 1.8 mm borosilicate glass ferrule using a picosecond laser ablation system. A detailed explanation of the fabrication procedure and preliminary tests demonstrating the static and dynamic properties of the sensor are described.

Chapter 3 includes a first demonstration of the dynamic mode capabilities. The FT sensor was used to measure the water content in a buffer atmosphere of nitrogen. Results obtained during these experiments prove that FT transducers can be used as gravimetric sensors.

Chapter 4 gives a detailed description of a major improvement regarding the dynamic mode operation. Instead of using an external piezoelement to excite vibrations of the sensor, as described in the previous chapter, a photoactuation scheme was applied. The all-optical actuation mechanism here implemented allows one to excite the vibrations and control the static bending of the FT sensor in a completely remote way. This approach allows one to extend the application range of ferrule-top sensors. As an example a set of humidity and pressure measurements have been included.

Chapter 5 investigates the properties of FT transducers as used in atomic force microscopy. In this chapter, a demonstration of topography measurements in air and liquid has been included.

Chapter 6 reports on a measurement of the Casimir force between a gold coated sphere attached to the FT sensor and a flat plate. The sensitivity achieved during this experiment allows one to conclude that FT transducers are an interesting alternative for standard setups, especially in case when electronic noise, small volume or harsh environmental conditions are present.

Chapter 7 presents a numerical simulation of air flow in the vicinity of an FT cantilever and compares them to the data acquired in a real wind tunnel. We have demonstrated that the small dimensions of the sensor in connection with all-optical operation creates an interesting alternative for commercial wind tunnel sensor. Additionally, in this chapter the performance of the sensor and its properties in comparison with other flow transducers are discussed.

Chapter 8 proves that FT transducers are very sensitive to external vibrations, thus a natural step is to use them as an advanced vibration sensors. In this chapter a new approach to landslide detection is proposed. Preliminary results show that the FT transducers are mainly sensitive to volumetric waves which makes them an attractive solution for monitoring acoustic emission in rocks.

Chapter 9 describes a unique design of an all-optical photoacoustic spectrometer based on ferrule-top technology. Sensitive detection of trace gases is an important issue in many industrial, chemical and biological applications. The chapter reports on an experiment where acetylene traces were detected reaching a minimum detectable concentration on the order of ppb.

Chapter 10 investigates the possibility of further evolution of the FT technology. Instead of carving the cantilever using differen machining techniques, a photolithography approach is proposed. The *align-and-shine* photolithography has a great potential to solve the problem of sensors batch fabrication. It can thus help to bring the technology to ordinary customers.

Chapter 11 is separated from the main part of the thesis as a general summary and outlook. Additionally it contains few new ideas regarding future applications of FT sensors.

Appendix A contains a list of publications, conference presentations and patents.

Chapter 2

Ferrule-top microdevices

2.1 Introduction

Fiber-top devices are a new generation of optical fiber sensors that combine the mechanical properties of micromechanical systems with the optical features of optical fibers [7]. This technology relies on the possibility to carve mechanical structures directly at the end a single mode optical fiber and to use the light coupled from the opposite end to detect movements of those mechanical parts in response to an external event. Thanks to this monolithic approach, it is possible to realize all-optical sensors for utilization in a wide range of applications, ranging from chemical sensing [11], refractive index measurements [12], and user-friendly atomic force microscopy [9].

In spite of the numerous advantages offered by FT sensors, the technology transfer process from prototype to market ready product has been seriously hampered by the high cost of fabrication of a single device. The manufacturing sequence, in fact, heavily relies on Focused Ion Beam (FIB) milling [7, 8]. This milling technique guarantees sufficient cutting resolution during the carving procedure, but, unfortunately, does not adapt well to cost effective series production.

An earlier attempt to replace FIB with less expensive carving techniques has been introduced in [13]. In that paper, we showed that it is possible to carve FT cantilevers using a two steps fs-laser micromachining process. Unfortunately, fs-laser machines are still quite expensive and, although may adapt better to series production, do not offer sufficient cutting resolution for most of the applications where FT sensors may be used.

An interesting alternative to carving-based fabrication processes is to switch

---

This chapter is partially based on papers:
G. Gruca, S. de Man, M. Slaman, J. H. Rector, and D. Iannuzzi *Proc. SPIE* **7503:750381**, (2009)
G. Gruca, S. de Man, M. Slaman, J. H. Rector, and D. Iannuzzi *Measurement Science and Technology* **21(9)**,094033, (2010)

to a bottom-up approach similar to that commonly used for Micro Electro-Mechanical Systems [MEMS] manufacturing, where structural and sacrificial layers are alternatively grown and patterned to achieve three-dimensional mechanical pieces [15]. The main obstacle in this process lies in the patterning procedure, as common optical lithography mask aligners are not designed for pattern transfer on the cleaved end of optical fibers. This problem was solved at the beginning of 2009 [14], when we introduced the align-and-shine technique for series production of arbitrary photolithography patterns on the cleaved end of an optical fiber. More work is currently under way to exploit this technique for bottom-up fabrication of fiber-top sensors.

In the meantime, one might still ask whether there exists any possible strategy to allow one to stick to the original approach (namely, carving structures out of the cleaved end of an optical fiber) with a cost effective technique. In the way to solve this issue, it is important to note that the main reason for which FT sensors are currently fabricated by means of FIB milling is ultimately determined by the outer diameter of the optical fiber. For most applications, FT devices are fabricated on single mode optical fibers, which have a diameter of 125 μm. The cleaved end of the fiber is thus an extremely small building block that must be carved in the form of a three dimensional structure. Machining devices over such a small area necessarily requires very high precision tools capable of carving the glass of the fiber with sub-micron resolution. To our knowledge, FIB milling is the only method that allows one to achieve such a high resolution.

On the other hand, for most of the applications where fiber-top sensors might have significant impact, the outer dimensions of the device are not too relevant. Fiber-top devices carved out of fibers with larger diameters would still be an acceptable solution. If one could use larger fibers as the building block of fiber-top devices, the typical size of the mechanical structures on top of the fiber could be scaled up to dimensions that are within the cutting resolution of less refined, and thus less expensive, carving tools. Unfortunately, commercially available single mode optical fibers only come with cladding diameter of 125 μm. One might thus ask whether there are other approaches that allow one to increase the outer diameter.

2.2 Fabrication

We present a new approach to obtain fiber-top-like micromachined devices using cost effective cutting tools that adapt well to series production (Fig. 2.1). The main idea is to use ferruled fibers as the building block of the fiber-top device. In a single mode ferruled fiber, a standard single mode optical fiber is inserted and glued into a pierced cylindrical ferrule made out of glass. The outer diameter of a ferrule is typically 1.8 mm, but differen dimensions and shapes can be straightforwardly produced and used. The diameter of the piercing hole that passes through the ferrule along the axis of the cylinder is 127 μm, i.e., just of the right dimension to host the single mode fiber. The single mode fiber is glued into the ferrule so robustly that the ferruled fiber is mechanically equivalent to a single mode optical fiber with a 1.8 mm diameter. Thanks to this property, we have been able to carve a micromachined cantilever on top of the ferruled fiber by means of a cost effective technique, namely, ps-laser ablation system. Here we describe the fabrication procedure and the tests with which we have assessed the mechanical properties of one of our first ferrule-top cantilevers.

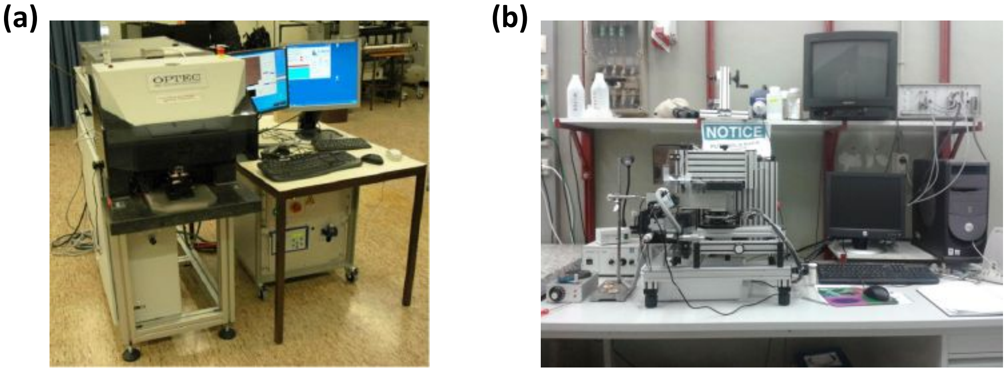

Figure 2.1: (a) The picosecond laser ablation system and (b) the precise diamond wire cutter used to fabricate ferrule-top cantilevers.

2.2.1 One-step procedure

A Duran borosilicate glass ferrule equipped with a SMF28e Corning single mode optical fiber (ThorLabs - SMPF0215) was attached to a microscope glass to facilitate handling procedure during the fabrication of the ferrule-top cantilever. The sample was mounted vertically on a X-Y stage of a 355 nm ps-laser ablation system depicted in Fig. 2.1a (Optec system with Lumera Laser Rapid source), where it was carved following the steps indicated in Fig. 2.2. The milling steps were performed with 11 ps long laser pulses at a repetition rate of 20 kHz and with an energy per pulse on the order of 100 μJ focused on a 5 μm diameter spot. To obtain the desired form, the sample was automatically moved with respect to the laser beam direction by means of a scanning motor moving at a speed of 50 mm/s in discrete steps (Fig. 2.3a). The step size was settled in such a way that two consecutive positions overlapped for 50%. Using those parameters, each laser pulses sequence produced a $\simeq$15 μm deep trench.

To carve deeper structures, multiple laser pulses were repeated on the same point before moving the stage to the next position. In Fig. 2.2d we report a microscope image of a 1.6 mm long, 200 μm wide, 30 μm thick cantilever obtained with the process described above. The entire fabrication process took 60 minutes - 40 minutes for the initial ridge (Fig. 2.2b) and 20 minutes for the undercut (Fig. 2.2c).

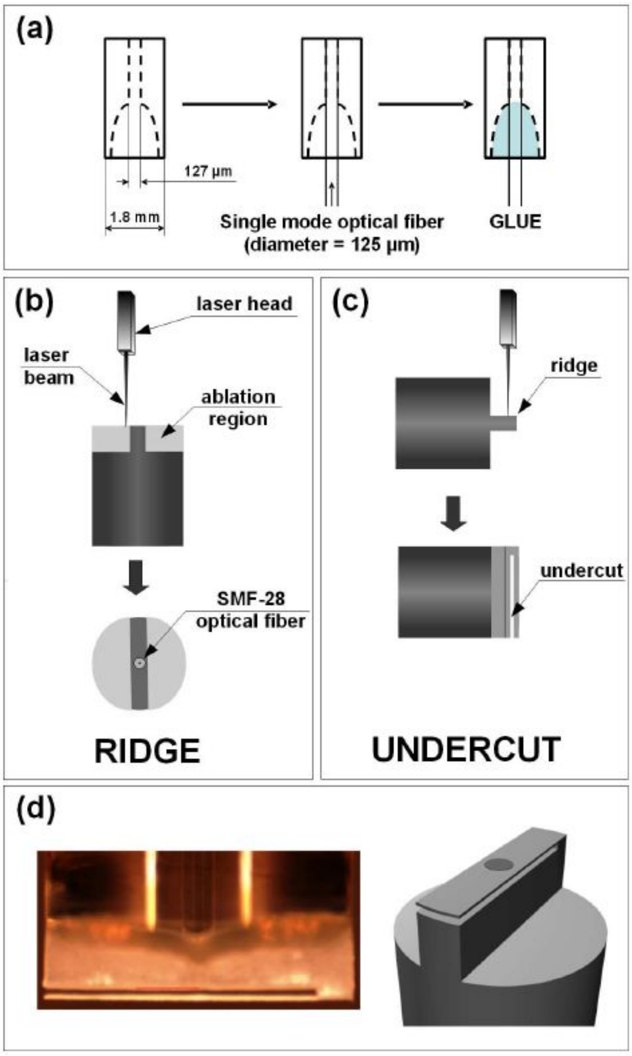

Figure 2.2: (a) Schematic view of the principle behind ferrule-top cantilevers; (b) and (c) milling steps in the fabrication of a ferrule-top cantilever; (d) microscope image (side view) and 3D model of the cantilever fabricated according to the procedure illustrated above.

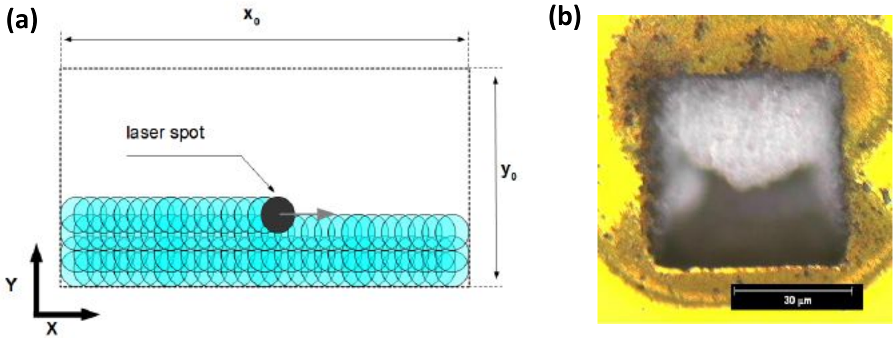

Figure 2.3: (a) Schematic view of the ablation process. The rectangle is ablated by means of line-by-line ablation within boundaries set by dimensions x_0 and y_0. (b) a $50{\times}50$ μm^2 square ablated in glass substrate (debris present inside are remains of the ablation process).

2.2.2 Two-step procedure

The procedure presented in the previous subsection is simple and straightforward. However, it has some limitations. One of the most important drawbacks is related to the limited aspect ratio achievable during the ablation process. A typical ratio between depth and width, approaching a value of about 4 for dimensions below 100 μm, effectively narrows a set of available geometries mainly to cantilevers. To extend the flexibility of the fabrication method, we have introduced an additional tool into the manufacturing scheme: a precise wire cutter (Fig. 2.1b). The wire cutter is equipped with diamond coated wire and allows one to cut the glass ferrule with micrometer accuracy. Instead of fabricating the ridge (Fig. 2.2b) by means of laser ablation, one can use the wire cutter to create an undercut at the beginning of the fabrication process (Fig. 2.4a). The typical diameter of the wire used during this operation is 250 μm, but for special cases this value can be reduced down to 80 μm. The released micromechanical structure, which looks like a tiny flap (thickness $\approx$30 μm), can be further processed and milled into a desired geometry via laser ablation. Devices fabricated according to this procedure can have much more complicated geometries as compared to those fabricated with the previous method. Therefore, multiple beams or structures connected by set of cantilevers can be taken into account in the process of designing the sensor (Fig. 2.4d). Moreover, as a direct consequence of omitting the time consuming ridge fabrication, an overall manufacturing time of the sensor have decreased.

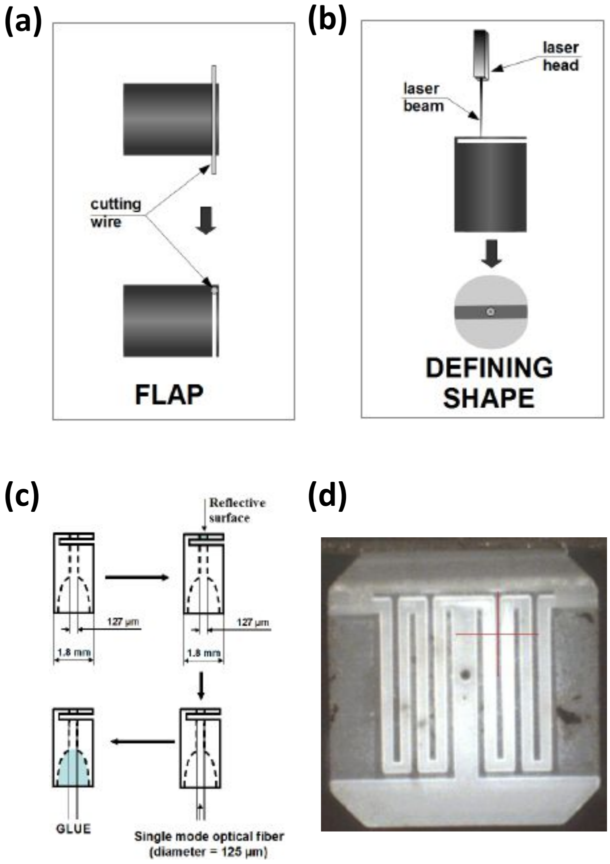

Figure 2.4: (a) Schematic view of the initial wire-cutting procedure. At the end of the process a thin, flat plate is formed; (b) laser ablation from the front allows one to define the final shape of the transducer; (c) at the end of the fabrication process a readout fiber has to be fixed inside the ferule; (d) microscope image of a sample structure obtained by two step procedure

2.3 Testing

The ferrule-top cantilever illustrated in Fig. 2.2 was coupled to the optical fiber interferometer readout sketched in Fig. 2.5 [7, 43]. The light impinging on the photodiode is the result of the optical interference of the light reflected at the fiber-to-air interface and the light reflected by the cantilever (which is the combination of the light reflected by the bottom surface of the cantilever and that reflected by the top surface of the cantilever). If multiple reflections from the cantilever are neglected, the current induced on the photodiode depends on the separation d between the fiber-to-air interface and the bottom surface of the cantilever according to the following equation[7, 43]:

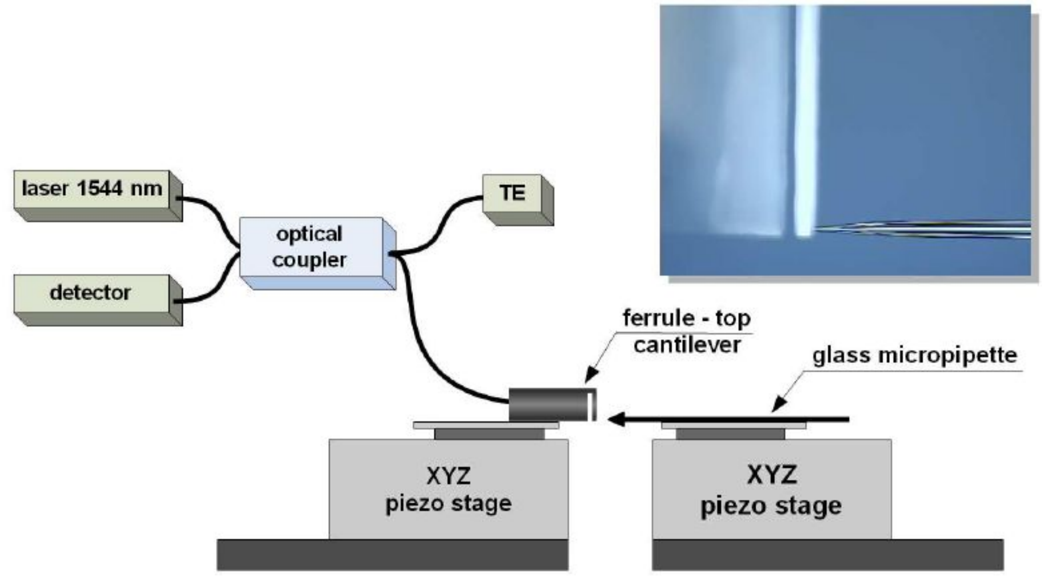

Figure 2.5: Schematic view of the setup used to test our ferrule-top devices (static bending). Inset: microscope image of the contact point between the glass micropipette and the free-hanging end of the cantilever. (TE - terminated end of the fiber).

$$I(d) = I_0 \left[1 + V \cos\left(\frac{4\pi d}{\lambda} + \varphi_0 \right) \right] \tag{2.1}$$

where φ_0 is a constant phase shift that only depends on the geometry of the cantilever, λ is the wavelength of the laser ($\lambda = 1544$ nm), and I_0 and V are, respectively, the midpoint interference signal and the fringe visibility, which are given by:

$$I_0 = \frac{I_+ + I_-}{2} \tag{2.2}$$

$$V = \frac{I_+ - I_-}{I_+ + I_-} \tag{2.3}$$

where I_+ and I_- represent the value of the current at maximum and minimum of interference. Connecting a charge amplifier to the photodiode, it is thus possible to remotely sense mechanical displacements of the ferrule-top device.

2.3.1 Static bending

To test the working principle of the device, we mounted the ferrule-top cantilever just in front of a glass micropipette anchored on a XYZ piezoelectric translation stage (Thorlabs NanoMax300) (see Fig. 2.5). A triangular voltage signal was then applied to the piezoelectric stage, previously calibrated with an optical interferometer, to linearly move the micropipette in and out of contact of the hanging end of the cantilever. In Fig. 2.6 we show the output signal of the readout system observed during three consecutive forward-backward sweeps. It is evident that the signal is constant before contact (no static movement of the cantilever). Once in contact, the linear forward movement of the cantilever end induced by the micropipette translates in a sinusoidal signal. During the linear backward motion, a similar behavior is observed, until the micropipette jumps out of contact and the signal becomes flat again. This behavior is in perfect agreement with eq. 2.1, and demonstrates that ferrule-top devices work according to design. Using the signal reported in Fig. 2.6, it is also possible to estimate the sensitivity of this particular ferrule-top device. We first note that, when the cantilever is at rest before contact, the output signal is quite close to the quadrature point ($I \simeq I_0$). In this region, one can linearize Eq. 2.1 to:

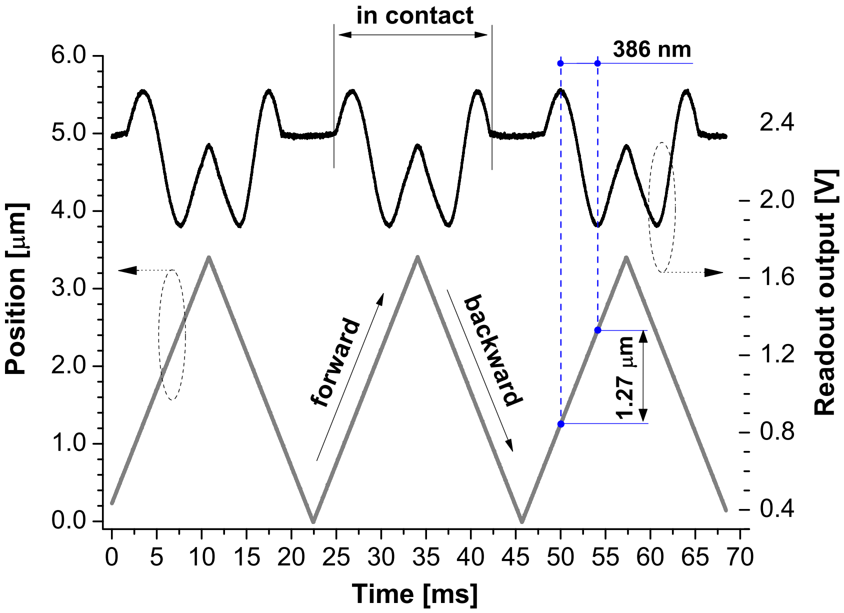

Figure 2.6: Results of the experiment to test the working principle of the ferrule-top cantilevers. The bottom line (left axis) represents the movement of the piezoelectric stage to which the micropipette was anchored and was obtained after proper calibration of the stage and corrections for hysteresis. The upper line (right axis) represents the output of the readout system. Regions where the needle were in or out of contact with the cantilever are clearly distinguishable.

$$I(d) = I_0 \left(1 + V \frac{4\pi d}{\lambda}\right). \tag{2.4}$$

According to the previous equation, the minimum detectable change of d is given by:

$$\Delta d = \frac{\lambda}{4\pi}\frac{M}{I_0 V}, \tag{2.5}$$

where M is the minimum current change detectable by the photodiode of the readout, and where we have neglected changes of λ. For the ferrule-top device presented in this paper, one can estimate the value of $\frac{M}{I_0}$ as $\frac{V_{rms}}{V_0}$, where V_{rms} and V_0 are, respectively, the noise out of contact and the midpoint output of the charge amplifier connected to the photodiode. V_{rms}, V_0, and V can be all obtained from Fig. 2.6. Using those values (V_{rms}=3.34 mV, V_0=2.23 V, V=0.17) in Eq. 2.5, one obtains $\Delta d \simeq 1$ nm (over the 100 kHz bandwidth of the charge amplifier). It is interesting to note that, in the device presented above, the deflection of the cantilever was not measured at the load point. The micropipette, in fact, was aligned at the extreme end of the cantilever, while, because of the design, the deflection was measured in correspondence of the core of the fiber, which lied 700 μm away from the anchor point (and, thus, $\simeq$900 μm from the load point). Using elementary mechanical arguments [15], one can see that, under this geometrical configuration, the deflection at the measuring point should be equal to 24.5% of the deflection at the load point. From Fig. 2.6, one can deduce that it was necessary to move the micropipette (and, thus, the extreme end of the cantilever) for approximately 1.27 μm to go from a minimum to a maximum of interference. From eq. 2.1, it is easy to see that the change in d to go from a minimum to a maximum of interference corresponds to $\frac{\lambda}{4}$, i.e., in our case, 386 nm. This corresponds to 30% of the deflection of the load point(1.27 μm), in good agreement with the expected value. The small discrepancy of the result might be due to the fact that the thickness of the cantilever is not equal over its whole length.

2.3.2 Dynamic behavior in air

To assess the mechanical properties of the ferrule-top cantilever presented above, we mounted the device on a custom made piezoelectric actuator with high resonance frequency (260 kHz). We then drove the piezoelectric actuator with sinusoidal oscillations and use a lock-in amplifier, connected to the ferrule-top readout system, to measure the amplitude of the mechanical vibrations of the cantilever induced by the movement of the piezoelectric actuator. To obtain the resonance curve, we scanned the frequency of the signal applied to the piezoelectric actuator and measured the peak-to-peak voltage that we had to supply to keep the oscillation of the cantilever always equal to a fixed value (roughly 8 nm). All measurements where conducted in air at room temperature. In Fig. 2.7 we report the result of this measurement. The two peaks illustrated in the figure correspond to the first two eigenmodes of the cantilever. Fitting those data with a Lorentzian curve, one obtains $\nu_1 = 11.7$ kHz

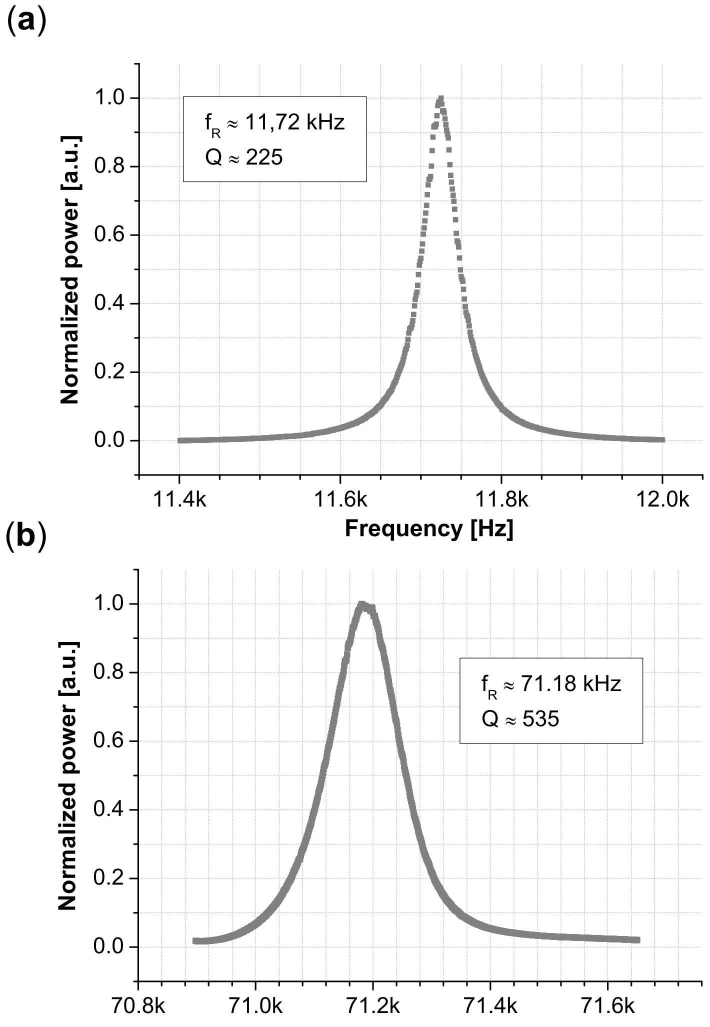

Figure 2.7: Normalized energy resonance curve of the (a) first and (b) second eigenmode. The FWHM of the curves are equal 52 Hz and 133 Hz for (a) and (b) respectively.

and $Q_1 = 225$ for the first mode, and ν_2 =71.2 kHz and Q_2=535 for the second mode. According to standard calculations for rectangular mechanical beams [44](Euler-Bernoulli equation), the theoretical value of ν_1 and ν_2 for a 1.6 mm × 200 μm × 30 μm cantilever made out of Duran (Young modulus = 64 GPa, Poisson ratio = 0.20 [45]) are, respectively, 10.3 kHz and 64.8 kHz, in agreement, within less than 15%, with the experimental values. The small discrepancy can once again be ascribed to the fact that the thickness of the cantilever is not equal over its whole length.

In Fig. 2.8 we report another independent measurement of the dynamic behavior of the same ferrule-top cantilever, where we analyzed the free oscillations of the mechanical beam excited after a sudden acceleration. To trigger the oscillations, we touched the end of the cantilever with a micropipette, as described in the previous subsection, and then quickly retracted it far from contact. The resonance curve was then obtained via Fourier Transform analysis of the readout signal during the free oscillations. The results are in good agreement with the measurements presented in Fig. 2.7. It is important to stress that the fabrication process is very reproducible. We are able, in fact, to systematically produce ferrule-top cantilever with a first mode resonance frequency of 10 ± 1 kHz.

2.4 Conclusions

Ferrule-top devices are interesting alternative to fiber-top MEMS. The fabrication of a ferrule-top device relies on ps-laser ablation - a table top affordable instrument that works in air and adopts well to series production. Some of the fabrication steps presented here could also be replaced by even more convenient approaches. For example, the initial ridge (Fig. 2.2b) can be obtained via polishing techniques, which would significally decrease the milling time.

The static performance at these devices are similar to those offered by fiber-top cantilevers [7] although the visibility of the interference fringes seems to be significally lower. We believe that the decrease of visibility is due to the fact that the gap between the fiber and the cantilever is much larger and that the surfaces are much rougher. Smaller gaps and a more refined ablation recipe might overcome this issue.

As for the fiber-top devices presented so far, the spring constant of ferrule-top cantilevers is rather large, in a range of 20–30 N/m (calculated from cantilever resonant frequency according to procedure described in [46]). To obtain more complaint devices, one can envision to either use larger ferrules (which would allow one to fabricate larger cantilevers), or to decrease the thickness of the cantilever (we succeeded to fabricate a few samples with a thickness below 20 μm), or more drastically, to abandon the cantilever geometry and use other mechanical structures that, with the same carving resolution, can give rise to lower spring constant. (e.g., a cantilever anchored to the ferrule by means of two thin torsional rods). It is also important to note that ferrule-top cantilevers offer a relatively high mechanical Q-factor when compared to smaller devices. This property might be advantageous for applications in force sensing, chemical sensing or for accelerometer purposes.

Acknowledgements – This work was supported by the European Research

Council under the European Community's Seventh Framework Programme (FP7/2007-2013)/ERC grant agreement number 201739 and by the Netherlands Organisation for Scientific Research (NWO) under the Innovational Research Incentives Scheme VIDI-680-47-209.

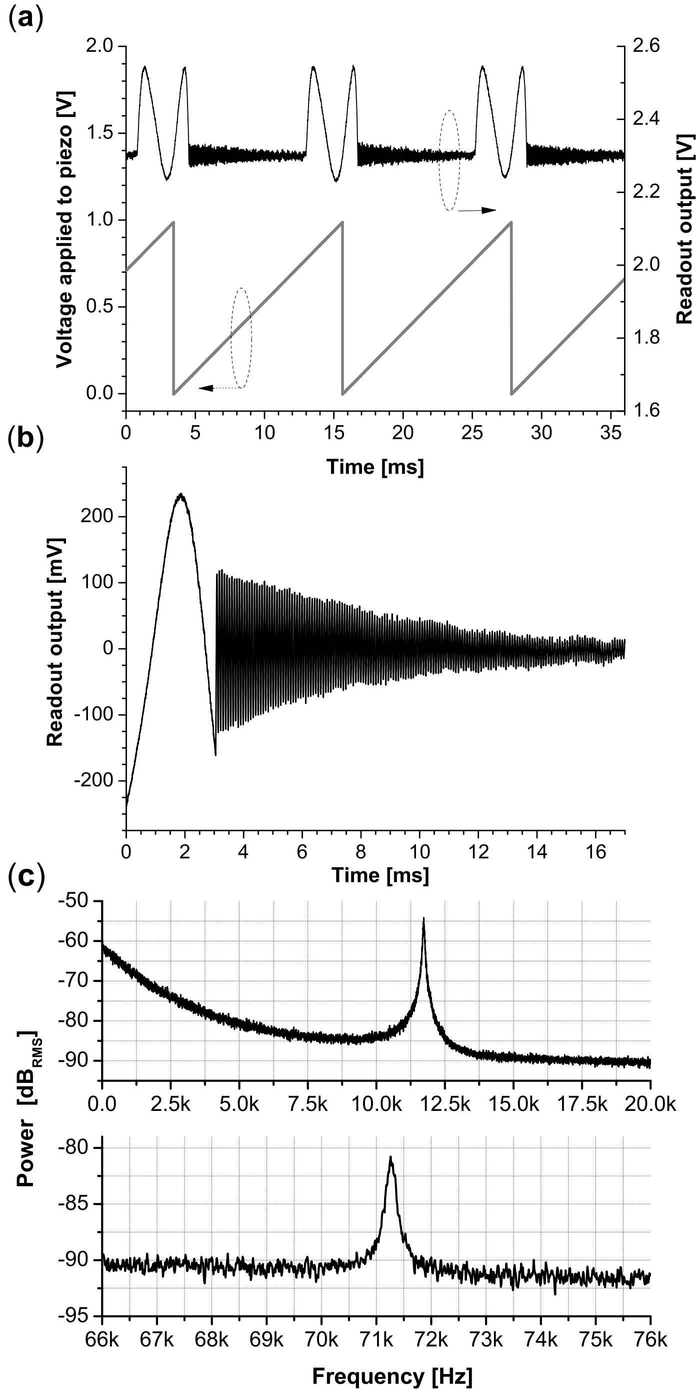

Figure 2.8: (a) snap-off experiment where the micropipette was moved to contact with the cantilever and then retracted rapidly (1 V saw tooth waveform at 82 Hz); (b) oscillations of the cantilever induced by the rapid snap-off; (c) FFT transform of the signal reported in (b).

Chapter 3

Optical fiber ferrule-top sensor for humidity measurements

We present an optical fiber ferrule-top sensor for humidity measurements. Changes in water content in a gaseous environment are detected by monitoring the resonant frequency and the quality factor of a cantilever fabricated on top of a ferruled optical fiber. Our experimental data demonstrate that the device offers high resolution and high repeatability.

This chapter is based on paper:

G. Gruca, J. Rector, K. Heeck and D. Iannuzzi, *21st International Conference on Optical Fiber Sensors; Proc. of SPIE* **7753**, 775358-4, (2011)

3.1 Introduction

Air humidity measurements are of paramount importance in many technological processes and in providing more comfortable environments in every day life. Depending on the application, humidity is typically monitored by means of, for example, quartz crystal microbalance [47], surface acoustic wave devices [48], fiber optic sensors [49], or integrated sensors [50]. In this paper we investigate whether optical fiber ferrule-top cantilevers [51] can also be used to that purpose. A ferrule-top cantilever is expected to change its frequency and mechanical quality factor in response to a change of humidity. Measuring the dynamical properties of the cantilever, it should thus be possible to monitor variations of water content in a gaseous atmosphere. Because of their reduced dimensions, high sensitivity, and all-optical design, ferrule-top humidity sensors might then become a suitable solution for applications where other sensors are less attractive.

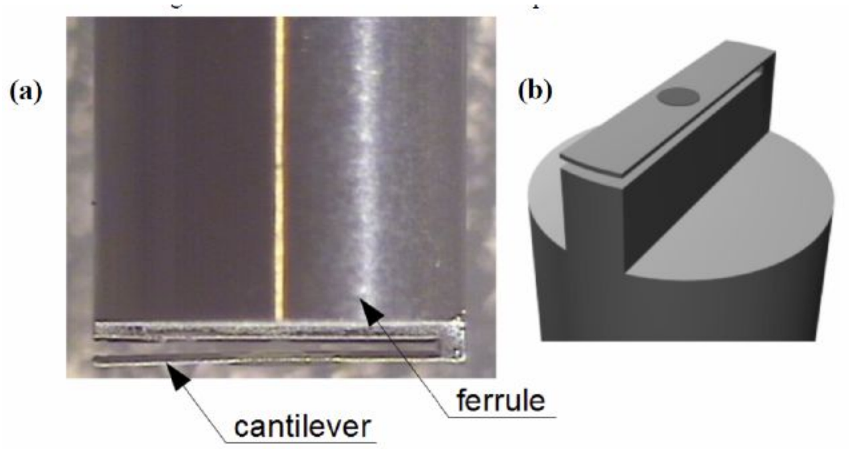

Figure 3.1: Microscope view (a) and 3D model (b) of ferrule-top cantilever.

3.2 Experimental setup

The working principle and fabrication process of ferrule-top cantilevers have been already extensively described in [51–53].In a nutshell, a ferrule-top cantilever is typically obtained by carving the end of a ferruled optical fiber in the form of a rectangular mechanical beam (see figure 3.1). Light coupled from the opposite end of the fiber allows one to detect whether the cantilever is bending via standard interferometric techniques. In figure 3.2 we report a schematic view of the measurement setup implemented to measure the resonance frequency and the mechanical quality factor of the cantilever as a function of the humidity of the surroundings. The ferrule-top sensor, which is coupled to a standard interferometric readout [51–53], is anchored to a piezoelectric block inside a chamber that is flushed with a constant flow of a wet and dry nitrogen mixture. Two computer controlled mass flow controllers allow the user to modify the ratio between the two components, and, thus, to accurately change the content of water in the atmosphere that surrounds the cantilever. The resonance curve of the cantilever is measured by sweeping the frequency of the sinusoidal excitation voltage that drives the piezoelectric block, and measuring, with a lock-in amplifier, the amplitude of the driving voltage needed to keep the amplitude of the oscillations of the cantilever constantly equal to a predefined set point.

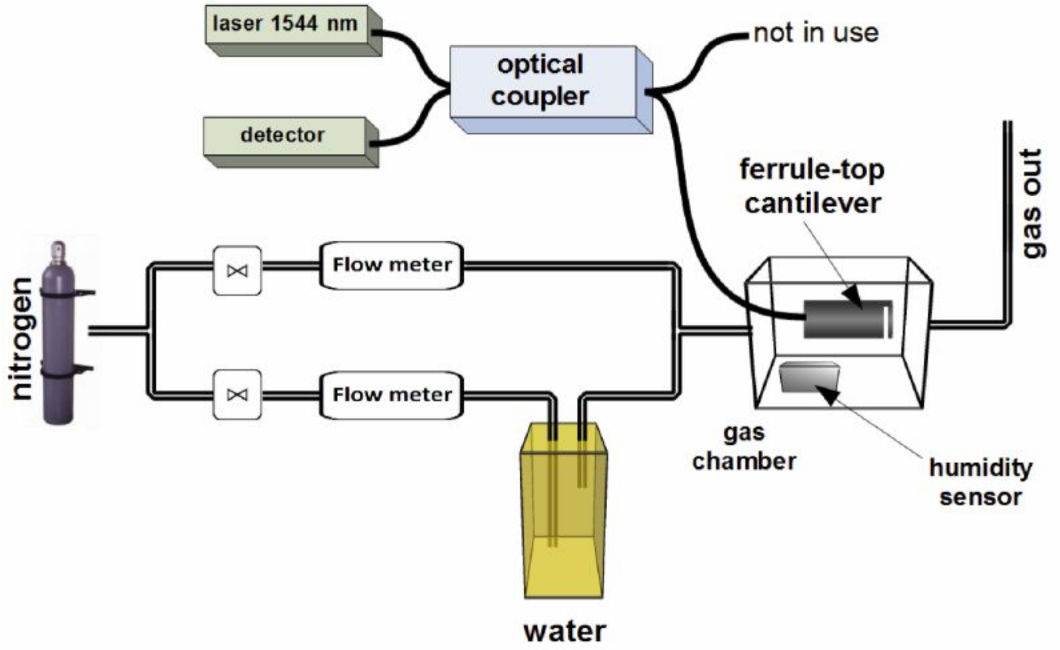

Figure 3.2: Schematic view of the measurement system. The ferrule-top cantilever is anchored to a small piezoelectric actuator inside the gas chamber (not shown).

3.3 Results

Figure 3.3 shows the results obtained with an uncoated 2050 × 200 × 30 μm ferrule-top cantilever that was fabricated on top of a 2.2 mm diameter cylindrical ferrule following the steps described in [53]. The resonance frequency and the mechanical quality factor of the ferrule-top cantilever are plotted as a function of the humidity of the surroundings as measured by a commercial humidity sensor (Sensiron SHT71) mounted close to the ferrule-top device. The overall duration of the experiment was 60 minutes. The time interval between

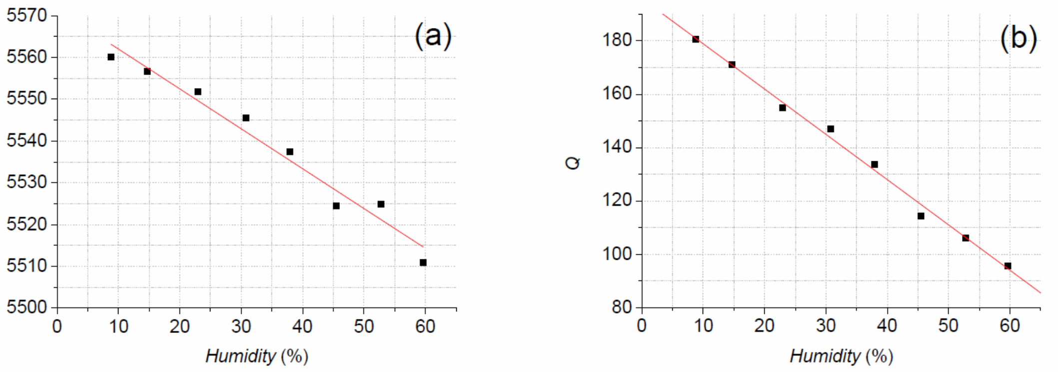

Figure 3.3: Resonance frequency (a) and quality factor (b) changes for a 2050 × 200 × 30 μm ferrule top cantilever with UV curable epoxy in central part. During measurement run, the temperature was constant within less then 0.2 ^{o}C. The line is a fit to guide the eye through the data.

each humidity set point was set to 45 s to allow the system to reach equilibrium. It is quite evident that both resonance frequency and quality factors decrease as the content of water increases. The first effect is due to the fact that, in the presence of higher humidity environments, the cantilever adsorbs more water and thus increases its mass. To understand the second effect, it is important to stress that the central part of the cantilever (the part that corresponds to the bore hole of the ferrule) is filled with UV curable epoxy. This block of glue probably absorbs more water in higher humidity environments. We speculate that when the glue is richer in water it also dissipates more mechanical energy, as observed in the experiment. Note that the absorption of water in the glue block is also expected to amplify the resonance frequency

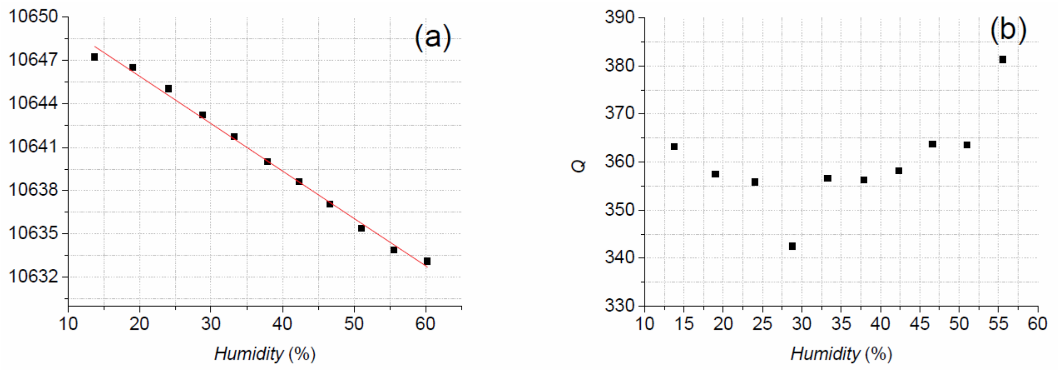

Figure 3.4: Resonance frequency (a) and quality factor (b) changes for a 1650 × 200 × 30 μm ferrule top cantilever with glass block in the central part. The line is a fit to guide the eye through the data.

shift, as the glue acts as a water sponge. Indeed, when we repeated the experiment with a 1650 × 200 × 30 μm cantilever fabricated on a 1.8 mm cylindrical ferrule with the method described in [51], where the block of glue is replaced with a block of glass, we observed that the dependence of the resonance frequency on humidity was less pronounced, while the quality factor did not show any dependence (within the experimental uncertainty) on humidity (see figure 3.4). We have demonstrated that optical fiber ferrule-top cantilevers can be used to detect humidity changes in the surrounding environment. Studies are under way to optimize sensitivity, reproducibility, and stability of this new miniaturized all-optical sensor.

Acknowledgements – This work was supported by the European Research Council under the European Communitys Seventh Framework Programme (FP7/2007-2013), ERC grant agreement 201739. The author would like to thank Dhwajal Chavan, Sven de Man and Khashayar Babaei Gavan for their support and inspiring discussions.

Chapter 4

Demonstration of an optically actuated ferrule-top device for pressure and humidity sensing

Ferrule-top micromechanical sensors are an alternative platform for point measurements in critical environments, where standard Micro-Electro-Mechanical Systems are prone to failure. To fully benefit from the all-optical character of this design, it is important to demonstrate that the mechanical pieces fabricated on top of the ferruled fiber can be actuated with light. In this paper we propose a convenient, all-optical actuation scheme that can be applied without any additional modification of the sensor design. The scheme relies on the photothermal effect, which is proven to be sufficient both for inducing significant static bending and for exciting the sensor to resonance. We also demonstrate that this mechanism can be successfully used to implement ferrule-top resonant sensors for humidity and pressure measurements.

This chapter is based on paper:

G. Gruca, D. Chavan, J. Rector, K. Heeck, D. Iannuzzi, *Sensors and Actuators A* **190**, 77-83, (2013)

4.1 Introduction

Optical fiber sensors (OFS) are widely recognized for their ability to offer high sensitivity and reliability even when operating in harsh conditions, such as electromagnetic noisy environments, high temperatures or in the presence of corrosive or explosive atmospheres [54–60]. Distributed and quasi-distributed OFS [61] have been for example successfully used in industry [62] and medical diagnosis [63–65]. Point sensors are also receiving increasing attention [66–68], as they can often measure relevant parameters in small volumes not accessible with distributed and quasi-distributed detection schemes. Furthermore, they can be designed to achieve better sensitivity as compared to the other OFS approaches. Extrinsic Fabry-Perot Interferometric (EFPI) transducers, for instance, have been proven to provide excellent temperature, acoustic waves, pressure, and vibration sensors [35, 69, 70]. It is within this category of devices that our group has recently introduced a new approach, which goes under the name of ferrule-top (FT) sensors [51]. FT sensors combine a fully-optical readout, typical of OFS, with the advantages of Micro-Electro-Mechanical Systems (MEMS). The sensing part of the sensor is a micromachined structure (typically a cantilever) fabricated at the top of a ferruled optical fiber. The optical fiber can be used to monitor the mechanical response of the micromachined structure, allowing one to build a whole range of all-optical transducers. Tipped FT cantilevers have been successfully used to implement miniaturized, easy-to-use Scanning Probe Microscopes (SPM)[71, 72]. It was also demonstrated that the pressure variations around an FT probe placed inside a wind tunnel induce deflections on the mechanical parts of the probe that can be quantitatively related to the flow of the gas [73]. In these two examples, the sensors have been used in static mode. To extend the potential field of applications, it is interesting to investigate alternative schemes based on the monitoring of dynamic parameters, such as resonance frequency or mechanical quality factor. Preliminary tests have indeed shown that FT cantilevers can provide the platform for the development of efficient dynamical vibration sensors [74, 75]. In some applications, however, the mechanical parts of the FT sensors must be set to motion via an external, controlled stimulus. In a recent paper, for instance, we exploited the dependence of the resonance frequency of a mechanical cantilever on the humidity of the surroundings to develop a humidity sensor. In that case, the vibrations were forced by means of an additional piezoelectric element attached to the ferrule [76]. That solution has a few disadvantages. The piezoelectric element may in fact introduce spurious effects that translate in a non-linear response of the sensor. Furthermore, the piezoelectric element must be driven via an additional electrical connection, hampering potential utilizations of the sensor in harsh environments. In this paper, we present an approach that eliminates this problem. The new approach relies on the use of a photothermal actuation mechanism similar to the one described in [77–79]. This approach does not need any mechanical modification of the device, eliminating the problem of non-linearity induced by the piezoelectric element. Furthermore, both actuation and detection take place via light signals a major advantage that allows one to develop truly all-optical miniaturized sensors.

4.2 Fabrication, readout, and excitation scheme

A typical FT sensor is carved from a 3 mm × 3 mm × 7 mm borosilicate glass ferrule (Vitrocom) equipped with a 125 μm bore (see [76]). A user-modified precise diamond wire saw based on Well Model 4240 is used to obtain a thin (35 μm) flap (see Fig. 4.1a). This additional step, in respect to the previously described procedure [51], allows us to shorten the fabrication time and provides much higher flexibility in the fabrication of complex geometries. After this first cutting process, the ferrule is cleaned in acetone and mounted on a ps-laser ablation system (OPTEC Laser Micromachining System), where the flap is carved in the form of a cantilever by means of line-by-line laser ablation (repetition rate 8 kHz, stage speed 20 mm/sec) (see Fig. 4.1b). To define high quality reflective surface, which is necessary for a proper readout of the sensor, a small drop of curable liquid material is applied in the hole left open

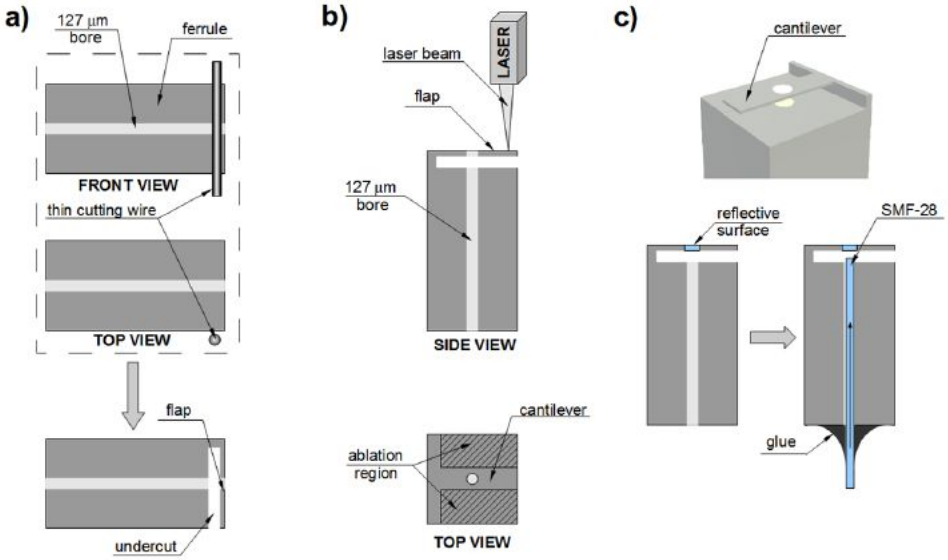

Figure 4.1: Fabrication procedure for a typical FT cantilever. As a first step, a thin flap is created by precise diamond saw equipped with 230 μm diameter wire - sketch (a). The geometry of the cantilever is then defined by means of laser ablation - sketch (b). Finally, the hole left in the cantilever is closed with a filling material and a single mode optical fiber is placed in the bore hole underneath - sketch (c).

on the cantilever. The filling material varies according to the application. To apply the drop, we first collect, by dipping, a tiny amount of filling material on a short piece of 100 μm diameter wire and then deliver it by bringing the droplet in contact with the hole. The filling drop is then cured according to the curing procedure indicated by the manufacturer. After the filling material is completely cured, a single mode optical fiber is placed in the bore hole of the ferrule and fixed with glue. Typically, the final dimensions of the cantilevers are 2800 μm × 220 μm × 35 μm (see Fig. 4.2). All the dimensions of the sensor can be tailored to the specific application [7, 80]. As a result, the mechanical properties of the cantilever, such resonance frequency or spring constant, may vary over a wide range of values. Typically, the resonance frequency can span from few hundred Hz to hundreds of kHz, while the spring constant can reach values as low as few N/m. More complicated structures, including multi-cantilever geometries and suspended seismic masses, can also be fabricated if their dimensions stay within the area of the used ferrule. The FT cantilever readout is based on Fabry-Perot (FP) interferometry [43], exploiting the cavity created between the fiber-to-air interface (where about 4% of the laser light coupled to the fiber is reflected) and the cantilever surfaces (Fig. 4.2). If the hole in the cantilever is filled with an opaque material, all the light that impinges on the cantilever is reflected from the bottom of the sensor, and the FP cavity signal is created by two interfering beams (interface A and B on Fig. 4.2b)). The situation is different in case of a transparent filling. In that case, it is more convenient to sputter an additional thin layer (~50 nm) of metal onto the cantilever to guarantee that most of the light be reflected from the top surface of the sensor (interface C on Fig. 4.2b). Because the thickness of the cantilever remains constant, the FP cavity signal can be assumed to depend only on the position of the cantilever with respect to that of the edge of the fiber. Based on this assumption one can write a general formula that

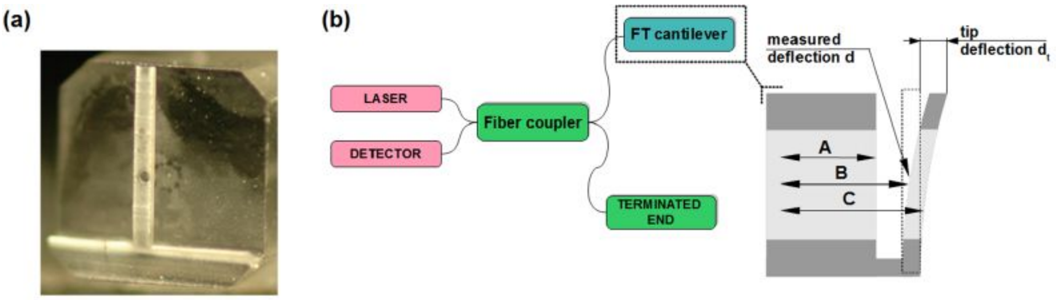

Figure 4.2: (a) Microscope image of a typical FT cantilever after the ablation process. (b) Sketch of the Fabry-Perot interferometer used to measure the deflection of the cantilever from the interference of the light reflected from three consecutive interfaces.

describes the signal at the output of the detector:

$$I(d) = I_0 \left[1 + V cos \left(\frac{4\pi d}{\lambda} + \varphi_0 \right) \right] \tag{4.1}$$

where the phase shift ϕ_0 comes from the initial geometrical conditions, λ is the wavelength of the readout laser, d is the bending of the cantilever at the measurement point, V and I_0 are the visibility and the mean value of the signal respectively. The measurement point is defined by the position of the readout fiber with respect to the cantilever and may vary for different geometries. However, in all cases the actual deflection of the tip dt can be calculated using simple mechanical theory [15]. The visibility for a cantilever with transparent filling and metallic coating is typically ≈90%, whereas in the case of non-transparent filling it reduces to 40% to 50%. To achieve optimal sensitivity and linearity, the readout is equipped with a tunable laser whose wavelength can be adjusted to match the quadrature condition. As for the actuation mechanism, in this work we have explored the possibility to rely on the local heating generated on the cantilever surface by an additional light source coupled to the readout fiber (photothermal effect [*]).

4.2.1 Static bending

To demonstrate that it is possible to use the photothermal effect to induce a controlled static deformation of ferrule-top mechanical structures, we fabricated an FT cantilever with UV-curable polymeric hole filling (NOA68 Norland), equipped with a fixed reference block at the top of the ferrule (see Fig. 4.3a). The device was aligned vertically with respect to an optical profiler measurement head (Wyko NT9100) (see Fig. 4.3). We then measured the bending of the cantilever as a function of the emission power of a 1.3 μm laser source directly coupled to the readout fiber. The results are reported in Fig. 4.3. It is clear that by varying the laser power one can control the static bending of the sensor, with maximum displacement, for this device, of 1.75 μm for 53 mW of laser power.

4.2.2 Dynamic excitation

The static bending mechanism described in the previous paragraph can be used to control the position of the cantilever within a few microns. It is however also interesting to understand whether, using the same mechanism, one

---

[*] It is important to separate the excitation mechanism here described from the more typical bimetallic effect. The ratio between the thickness of the cantilever (35 μm) and the additional metallic coating (50 nm) is so small that the bimetallic effect is negligible. The same applies to light pressure, which is expected to exert a force on the cantilever of approximately 20 pN, corresponding to pm cantilever deflections.

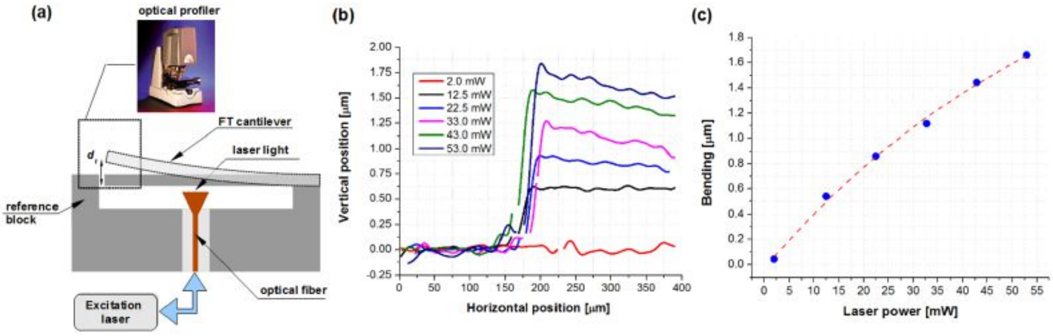

Figure 4.3: (a) Schematic view of the static bending experiment. (b) Optical profiler line passing across the cantilever (150 μm to 400 μm) and the reference block (0 μm to 150 μm) for different power values of the excitation laser. (c) Bending of the cantilever as a function of the power of the excitation laser.

can drive a dynamic excitation. In this case the intensity of the excitation laser has to be modulated. The amplitude modulation, performed at certain frequency, creates heat waves that propagate in the cantilever. These waves periodically modify the local stress in the profile of the sensor and, as a result, excite the vibrations. To test this approach, an FT cantilever with polymeric hole filling was coupled to the optical setup sketched in Fig. 4.4. The optical readout is combined with a 1.3 μm excitation laser using two wavelength division multiplexers (WDM). Each multiplexer provides at least 16 dB isolation between readout and excitation wavelengths. To create the heat waves in the cantilever profile, the intensity of the 1.3 μm laser is modulated using a square wave (amplitude modulation). The frequency of the modulation is controlled by a computer and swept close to one of the mechanical eigenfrequencies of the cantilever. During the sweep, the computer acquires the amplitude and the phase (with respect to excitation signal) of the signal emerging from the FP cavity. Both parameters are measured by a lock-in amplifier locked to the excitation source.The power of the excitation laser was set to 10 mW and the modulation depth to 100%. The amplitude response recorded for the first three eigenmodes is shown on Fig. 4.5. All measured resonances are close to the values predicted on the basis of Euler-Bernoulli beam theory [44](5.44 kHz, 34.14 kHz and 95.57 kHz, respectively).

To calculate the efficiency of the excitation mechanism, we measured the amplitude of the fundamental mode oscillations induced at resonance as a function of the excitation laser power. The results obtained both in air and vacuum (10^{-3} mbar) are reported in Fig. 4.6. It is interesting to note that, apparently, when the cantilever is in vacuum, the excitation efficiency is increasing. This behavior can be explained by considering that, in vacuum, the cantilever can dissipate heat less efficiently than in air. Therefore, due to the

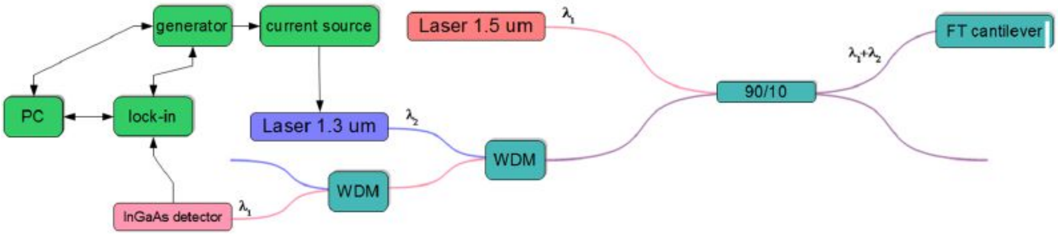

Figure 4.4: Combined setup to simultaneously measure the bending of the cantilever and to excite its vibrations. The FT sensor is connected to an arm of the optical coupler in a way that 90% of the light coming from the FP cavity is coupled into the arm where the photodetector is located. At the same time 90% of light delivered by the excitation laser impinges on the cantilever.

reduced convection, the temperature gradient (and, thus, the bending reached for the same excitation laser power) is higher in vacuum.

4.3 Humidity and pressure sensors

The dynamical mechanical properties of FT cantilevers strongly depend on variations of mass, surface stress and viscosity of the surrounding medium [81, 82]. Here we show that, combining this principle with the excitation mechanism described in the previous section, one can implement truly all-optical sensors. By way of example, we focused on two proof-of-concept tests on humidity and pressure sensing.

4.3.1 Humidity sensor

An FT cantilever, with polymeric hole filling (NOA68 Norland) and metallic coating, was connected to the optical setup shown in Fig. 4.4 and inserted in a test chamber equipped with a humidity control system. Using the excitation-detection scheme described in the previous section, we then measured the resonance curve of the fundamental mode as a function of the humidity of the gas contained in the chamber. The humidity inside the chamber was simultaneously measured, for reference, by a calibrated commercial sensor (Sensirion SHT75). During all measurements, the temperature variations inside the chamber were less than 0.5 K and had a minor influence on outcome of the experiment (estimated drift 0.5–1 Hz/°C). The results of the measurements are reported in Fig. 4.7. As one can notice, for higher humidity levels the mechanical quality factors worsens and the center of the resonance curve shifts towards lower frequencies at a rate of 7 Hz/% for the second eigenmode. It is evident that this phenomenon can be used to implement all-optical humid-

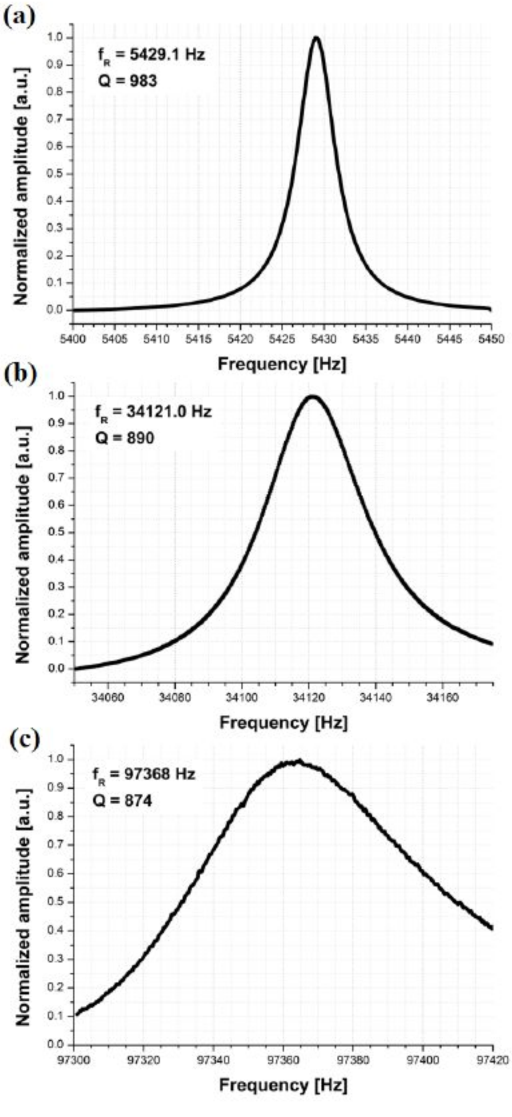

Figure 4.5: Spectrum of the first (a), second (b) and third (c) eigenmodes driven with light excitation. The measurements were performed in vacuum (10^{-3} mbar).

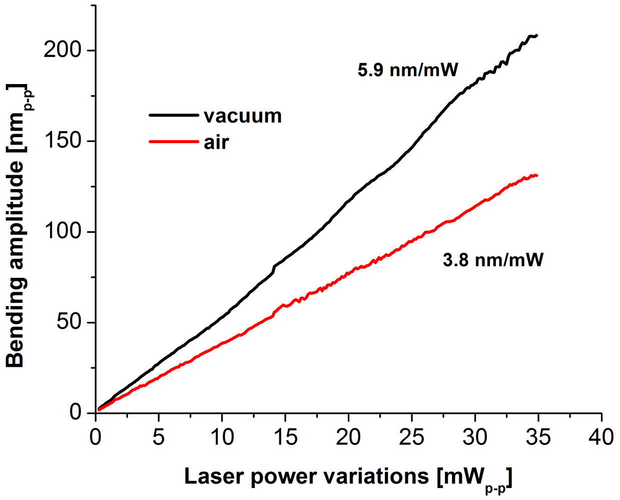

Figure 4.6: Cantilever bending amplitude as a function of excitation laser power at resonance with the fundamental frequency. Measurements were performed both in air and vacuum (10^{-3} mbar).

ity sensors. As water adsorbs on the cantilevers surfaces or is absorbed by the polymeric filling material, in fact, the mass and the spring constant of the cantilever changes. These changes can be detected by following the mechanical resonance frequency of the sensor. If one neglects the influence of temperature (which is a known performance limiting factor in moisture measurements [83]) and calculates the minimum detectable humidity change as three times the rms noise of frequency measurements, one can estimate that the resolution of our sensor is approximately 0.02%, which is comparable with present optical fiber based sensors [84, 85] and better than gravimetric transducers [86]. To further improve the sensitivity one can replace the material filling the cantilever bore hole with a more absorbing one. A proper selection of the sensing polymer, in fact, can significantly change the response of optical fiber humidity transducer [87, 88].

4.3.2 Pressure sensor

To test the capability of all-optical FT sensors to measure pressure, an FT cantilever with a non-transparent filling material (TorrSeal® resin) was enclosed inside a chamber connected to a vacuum pump and to a leak-valve. This system allowed us to reproducibly vary the pressure inside the chamber from 10^{-3} mbar to atmospheric pressure. The residual pressure was continuously monitored by a commercial pressure gauge (MKS DualTrans® 910). For this

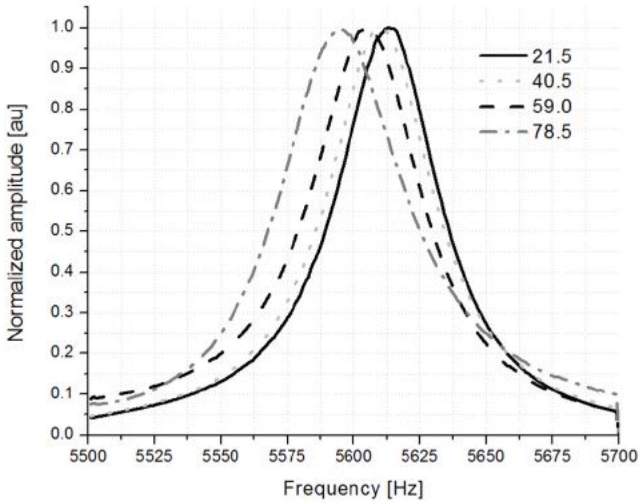

Figure 4.7: Resonance curves of the fundamental mode of an FT cantilever acquired for different humidity levels.

set of measurements, the setup was modified as depicted in Fig. 4.8. The main difference with respect to the solution shown in Fig. 4.4 lies in the electronic part, which offers now the possibility to automatically lock the light excitation frequency to the resonance frequency of the cantilever, and thus measure the latter without necessarily acquiring a complete vibration spectrum. The

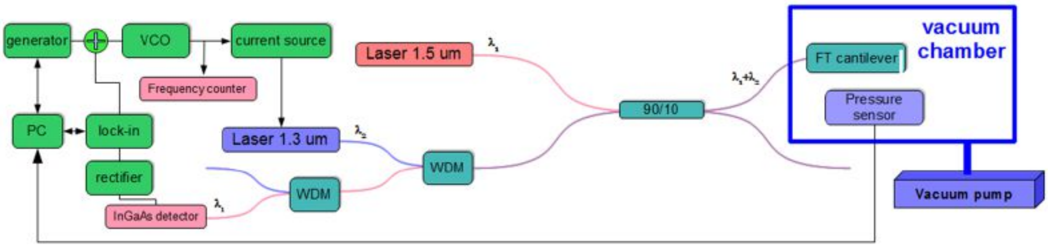

Figure 4.8: Schematic view of the readout and excitation setup for pressure measurements. The electronic part of the readout allows one to lock to the resonance curve and measure the resonance frequency of the cantilever instantaneously, without necessarily acquiring a complete vibration spectrum.

locking mechanism is based on an FM/AM technique. The carrier frequency of the excitation laser is controlled by a Voltage Controlled Oscillator (VCO). At the start of the experiment, the voltage on the input of the VCO is set to the level that corresponds to the resonance frequency f_R of the cantilever (Fig. 4.9). The carrier frequency is then swept around the resonance frequency (between points A and B of Fig. 4.9) by adding a low frequency (f_m) modulation on the VCO. As a result, the amplitude of the signal received from the photodetector of the setup is the combination of a high frequency component (due to the oscillation of the cantilever at the resonance) and a low frequency component (due to the change of the cantilever amplitude response around the resonance). The latter is isolated in a rectifier and fed into the lock-in amplifier that measures its 90 degree shifted component. The average value of this signal, which is proportional to the derivative of the curve reported in Fig. 4.9, is then used to drive a high gain loop that keeps the carrier frequency at the peak of the mechanical resonance curve. When the loop is locked, the amplitude of the low frequency component (fm) is roughly zero. At the same time its second harmonics reaches maximum.For this proof-of-concept experiment, we measured the first resonance frequency of the cantilever as a function of the pressure in the chamber, which was first evacuated to 10^{-3} mbar and then slowly filled with air up to atmospheric pressure. The time constant of the loop was set to 1 s to prevent instabilities connected with a high quality factor of the cantilever in vacuum (≈1400). The measurement took about 3 minutes. After that, we repeated the procedure while monitoring the second eigenfrequency of the sensor. The results of both experiments are reported in Fig. 4.10. An analysis of the noise of those data shows that, with this sensor, one can achieve a pressure resolution of 1 mbar and 0.5 mbar for the first and second mode respectively. In comparison, membrane-based fiber optic pressure sensors [89, 90] have typically higher resolution and sensitivity but lower pressure range. Additionally, contrary to FT sensors, they can be damaged by overpressure. On the other hand, fiber optic Bragg-grating (FBG) pressure transducers are in general less sensitive [91, 92], but cover a much wider work-

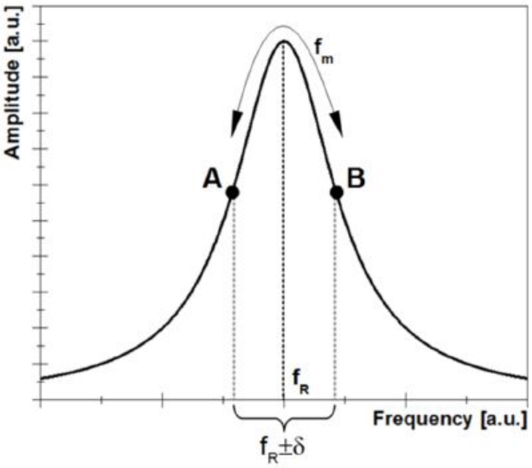

Figure 4.9: Definition of the parameters used in the description of the technique that allows instantaneous tracking of the resonance frequency of the FT cantilever (see text).

ing range. FT sensors thus seems to fill the gap between membrane-based and FBG transducers, offering a tradeoff between sensitivity and working range.

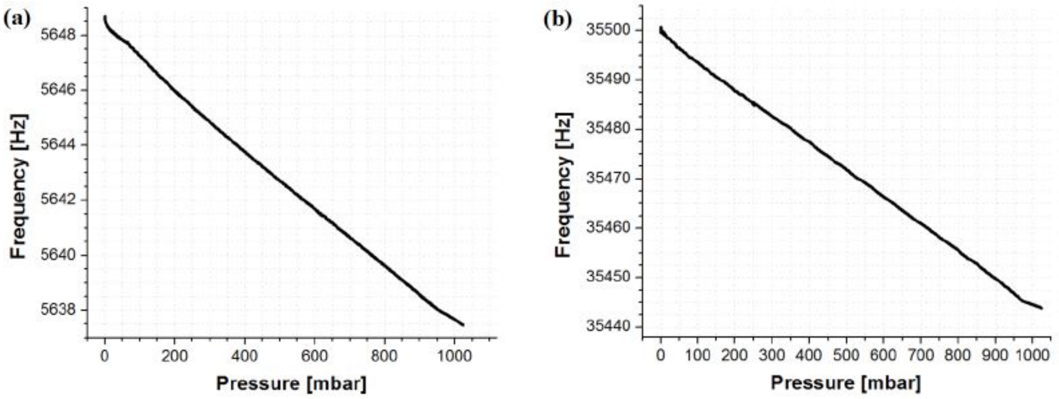

Figure 4.10: Resonance frequency of the first (graph a) and the second (graph b) mode of an FT sensor as a function of air pressure. The slope of the curves corresponds to 0.01 and 0.05 Hz/mbar for the first and second mode respectively.

4.4 Conclusions

In this paper we have proposed an all-optical excitation scheme that can be applied to actuate FT devices. The excitation light is delivered to the sensor via the same optical fiber that is simultaneously used to measure the deflection of the mechanical part fabricated on the ferrule. Therefore, the scheme can be applied without any change in the design of the device. We have demonstrated that by varying the power of the excitation laser one can control the static bending of an FT cantilever. Moreover, by introducing an amplitude modulation one can excite the vibrations of the device and measure its resonance curve, paving the way to the development of truly all-optical sensors. To demonstrate this principle, we have implemented two proof-of-concepts experiments that show the ability of this approach to measure changes in environmental humidity and pressure. The results confirm that the combination of all-optical excitation with all-optical readout is indeed possible and may be used as a new platform for point sensing in critical environments.

Acknowledgements – The authors acknowledge support from the European Research Council under the European Communitys Seventh Framework Program (FP7/2007-2013)/ERC grant agreement number 207139 and the Dutch Foundation for Fundamental Research on Matter (FOM) under a Valorization Grant.

Chapter 5

Ferrule-top atomic force microscope

Ferrule-top cantilevers are a new generation of all-optical miniaturized devices for utilization in liquids, harsh environments, and small volumes [*G. Gruca et al., Meas. Sci. Technol. 21, 094033 (2010)*]. They are obtained by carving the end of a ferruled fiber in the form of a mechanical beam. Light coupled from the opposite side of the fiber allows detection of cantilever deflections. In this paper, we demonstrate that ferrule-top cantilevers can be used to develop ultra compact AFMs for contact mode imaging in air and in liquids with sensitivity comparable to that of commercial AFMs. The probes do not require any alignment procedure and are easy to handle, favoring applications also outside research laboratories.

This chapter is based on paper:

D. Chavan, G. Gruca, S. de Man, M. Slaman, J. H. Rector, K. Heeck and D. Iannuzzi, *Rev. Sci. Instrum.* **81**, 123702, (2010)

5.1 Introduction

Since its invention in 1986 (Ref. [16]) atomic force microscopy has witnessed an ever increasing popularity. Today, the atomic force microscope (AFM) is considered a unique instrument for its ability to provide surface topology images, force measurements, and information on material properties at the nanoscale. It is thus not surprising to notice that many research groups belonging to both the academic and the industrial environment have been continuously proposing new solutions to improve the performance of their AFMs, from novel imaging modes [93, 94] to high speed [95–97] and video rate scanning [98]. In spite of this impressive progress, in most commercially available AFMs the deflection of the cantilever is still detected by means of optical triangulation. Optical triangulation, however, requires a volume of several cm^3, making further miniaturization virtually impossible. Furthermore, it does not adapt well to applications beyond research laboratories, where untrained personnel might not be comfortable with the alignment procedure necessary to bring the laser spot on the cantilever before utilization. Alternative detection schemes, like, for example, piezoresistive sensing [99], can be hardly used in liquid environments. There is thus an evident need of a compact, all-optical probe that overcomes the alignment procedure. In 2006, our group has proposed a new generation of miniaturized devices that may solve this issue: the fiber-top cantilever [7, 9]. In a fiber-top probe, the cantilever is carved at the center of the cleaved end of an optical fiber. Light coupled from the opposite side of the fiber can then be used to detect the deflection of the cantilever. The probe is extremely compact (it is machined on a 125 μm diameter fiber), all-optical, and very easy to use (the operator only needs to plug the fiber to the readout system). Unfortunately, fiber-top cantilevers are currently produced by means of a very expensive process (namely, Focused Ion Beam milling [8]). To solve this problem, at the beginning of 2010 we introduced a new approach to fiber-top probes, which now goes under the name of ferrule-top cantilevers[51, 100]. Ferrule-top cantilevers are obtained by carving a cantilever out of a ferruled optical fiber. Because the dimensions of a ferrule are more than one order of magnitude larger than those of a fiber, the fabrication process can rely on steps that adapt better to cost effective series production. In this paper, we show that it is possible to equip a ferrule-top cantilever with a sharp conical tip for AFM purposes. The ferrule-top probe is then mounted on an extremely compact AFM, where it is used for contact mode imaging in both air and water.

5.2 Ferrule-top probe: fabrication and readout

Ferrule-top tipped cantilevers are obtained via the fabrication steps illustrated in Fig. 5.1. The building block is a 2.5 mm × 2.5 mm × 7 mm pierced ferrule made out of borosilicate glass (VitroCom Inc.), with a central bore hole that has a diameter of 127 μm [Fig. 5.1(i)]. The ferrule is initially mounted on the stage of a ps-laser ablation machine (Optec System with Lumera Laser source), where, following the steps described in Refs. [51] and [100], it is machined into a 220 μm wide, 200 μm thick rectangular ridge [Fig. 5.1(ii)]. The ablation machine is then used to carve a 50 μm × 50 μm suspended square hole at the end of the ridge and a v-groove on the side of the ferrule [Figs. 5.1(iii) and 5.2]. After the ferrule is taken out of the ablation machine, a GeO_2 doped single mode silica fiber (Fibercore Ltd.), equipped with an ≈8 μm high, ≈100 nm radius conical tip[1] is laid on the v-groove, slid into the rectangular hole, and glued to the ridge [Figs. 5.1(iv) and 5.3]. The ferrule is then mounted again on the stage of the ps-laser ablation machine to carve the ridge in the form of a tipped cantilever [Figs. 5.1(v) and 5.4]. The length and the width of the cantilever can be controlled within the cutting resolution of the laser ablation system (approximately 5 μm). The thickness of the cantilever is more difficult to control, and is limited to 10 μm reproducibility. Because of those limitations, we generally carve cantilevers that are 2200–2300 μm long, 215–225 μm wide, and 20–30 μm thick, which correspond to spring constants between 8 and 20 N/m and resonance frequencies between 5 and 7 kHz. At the end of the carving process, the residual hole at the center of the cantilever is filled with ultraviolet (UV) curable glue. The probe is then put inside a sputtering system, where it is coated with a 5 nm thick Cr layer followed by a 30 nm thick Au film [Fig. 5.1(vi)]. Finally, a singlemode optical fiber (Corning SMF28-e) is slid into the bore hole of the ferrule and glued [Fig. 5.1(vii)]. At the opposite end, the fiber is plugged to a commercial optical interferometer readout (LDM1300, Attocube AG) that couples a laser source into the fiber and measures the amplitude of the signal reflected by the head of the probe [7, 43]. This signal is the result of the interference between the light reflected at the fiber-to-gap interface, the light reflected by the gap-to-cantilever interface, and the light reflected at the cantilever-to-metal interface (see Fig. 5.5), and

---

[1] To obtain the tip, we used the method described in T. Pangaribuan, K. Yamada, S. Jiang, H. Oshawa, and M. Ohtsu, Jpn. J. Appl. Phys. 31, 1302 (1992). The fiber was cleaved and immersed for 360 minutes in a buffered HF solution (NH_4F:HF:H_2O, 7:1:1 volume ratio), where, because of the different etching rate of the cladding and the core, the tip spontaneously forms. Our fibers, however, had a slight dip in the doping profile in correspondence of the most central part of the core. This detail did not allow us to produce tips with a radius smaller than 100 nm. Using a fiber with a uniform doping profile, though, one should be able to systematically produce 10 nm radius tips.

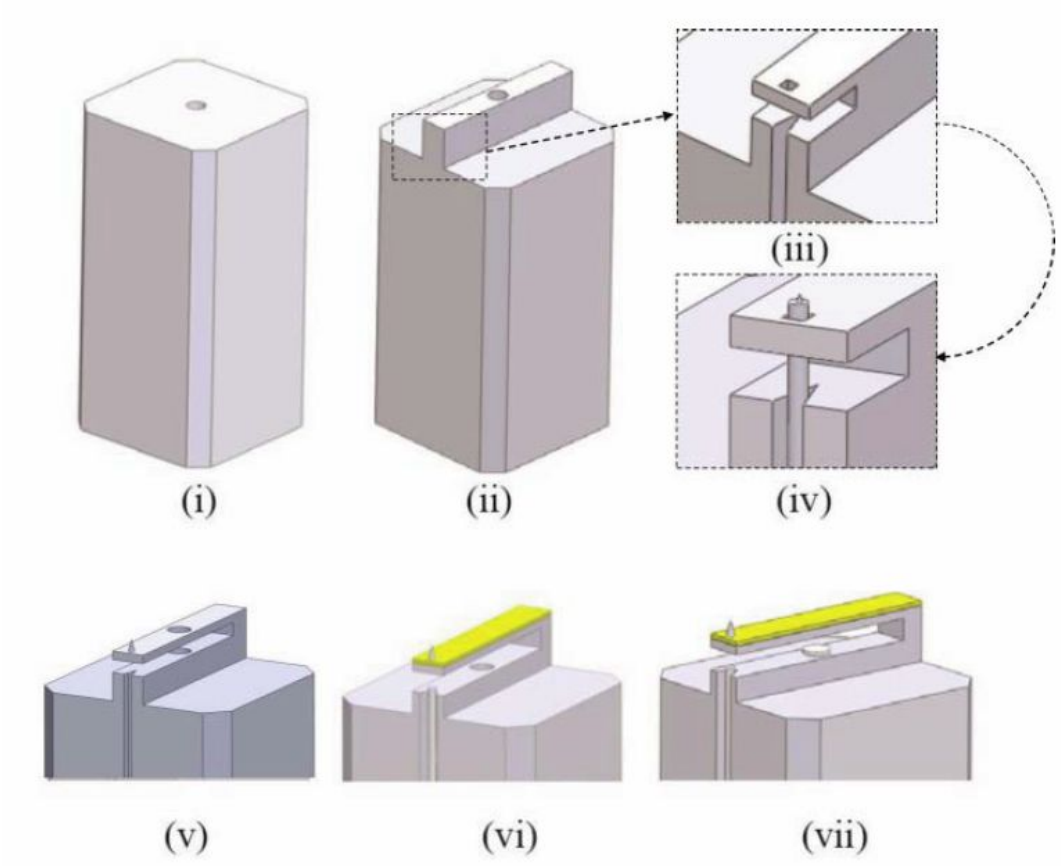

Figure 5.1: Illustration of the fabrication steps followed for the production of tipped ferrule-top cantilevers (not to scale): (i) the building block is a 2.5 mm × 2.5 mm × 7 mm pierced ferrule made out of borosilicate glass (diameter of the central bore = 127 m); (ii) the top of the ferrule is machined in a form of a 220 m wide, 200 m thick rectangular ridge; (iii) one side of the ridge is machined to host an ≈50 m diameter fiber; (iv) a ≈50 m diameter fiber with a conical sharp tip on its end is glued to the ridge; (v) the ridge is further machined in a form of a cantilever (undercut); (vi) a droplet of glue is placed inside the hole at the center of the cantilever, and the probe is coated with a thin gold layer; (vii) a standard single mode optical fiber is inserted into the bore of the ferrule and glued.

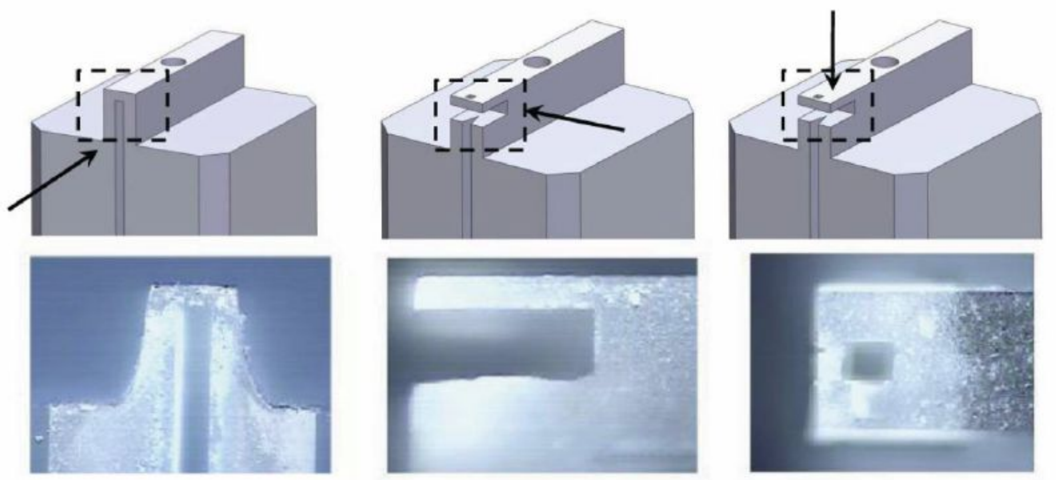

Figure 5.2: Optical microscope images of the v-groove and of the suspended rectangular hole carved to host a ≈50 μm diameter fiber. The arrows in the drawings indicate the view direction.

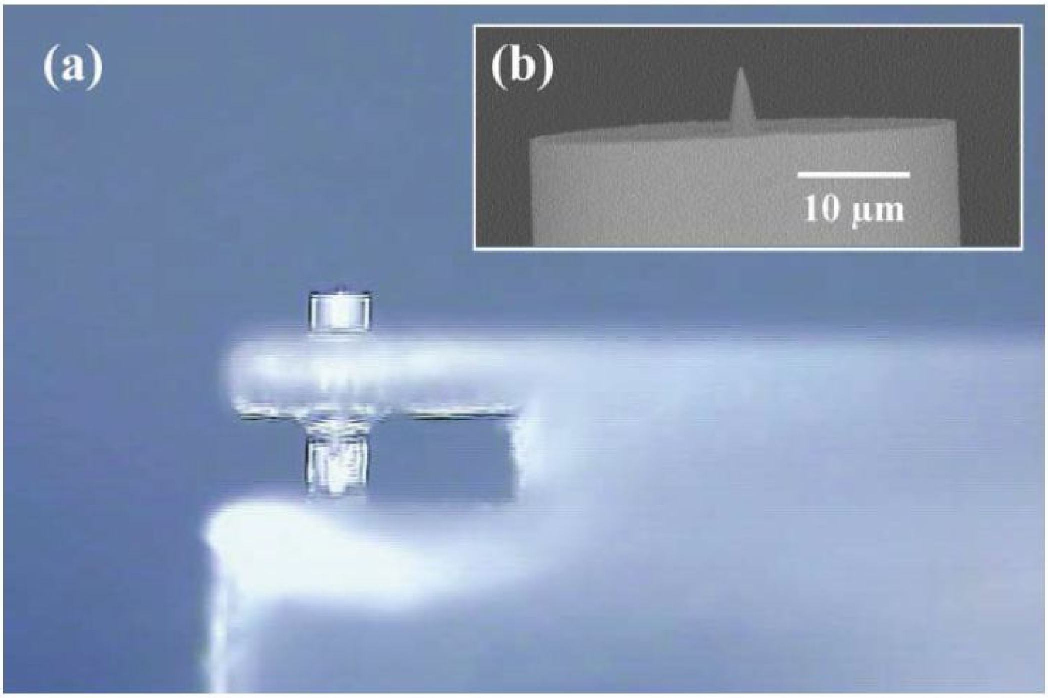

Figure 5.3: (a) Optical microscope image of the end of the ridge after step (iv) of Fig. 5.1. (b) Scanning electron microscope image of the sharp tip formed on the GeO_2 doped silica fiber by means of chemical etching in a buffered HF solution.

its amplitude is given by [7, 43]

$$W(d) = W_0 \left[1 + V \cos \left(\frac{4\pi d}{\lambda} + \varphi_0 \right) \right], \tag{5.1}$$

where d is the separation between the fiber-to-gap and the gap-to-cantilever interfaces, φ_0 is a constant phase shift that only depends on the geometry of the cantilever, λ is the wavelength of the laser ($\lambda = 1310$ nm), and W_0 and V are, respectively, the midpoint interference signal and the fringe visibility. From the signal of the readout system, it is thus possible to remotely sense mechanical displacements of the ferrule-top device [7, 9, 51, 100]. It is to note that the fabrication procedure presented here is slightly different with respect to that described in Refs. [100] and [51]. In the latter, the central fiber is glued before any carving procedure. In this way, however, the surface roughness of the fiber-to-gap and gap-to-cantilever interfaces is determined by the laser ablation process, which cannot provide optically smooth surfaces. The method described here, on the contrary, allows one to rely on optically smooth surfaces at all interfaces, increasing the fringe visibility. Thanks to this expedient, it is now possible to systematically achieve an root-mean-square (rms) deflection sensitivity on the order of 0.1 nm (and, thus, 0.3 nN rms force sensitivity for loads applied to the free hanging end of the cantilever) over the 35 kHz bandwidth of the interferometer.

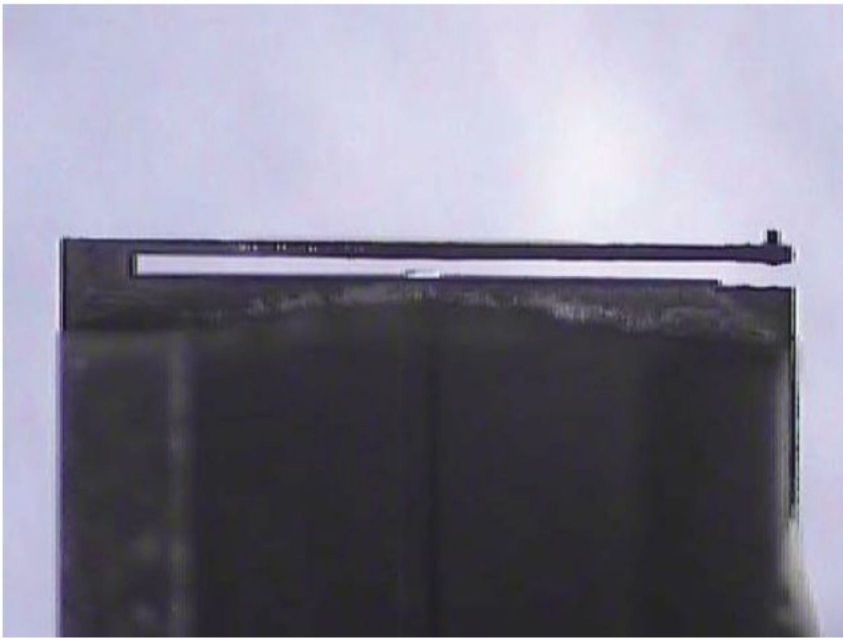

Figure 5.4: Optical microscope image of a tipped ferrule-top cantilever.

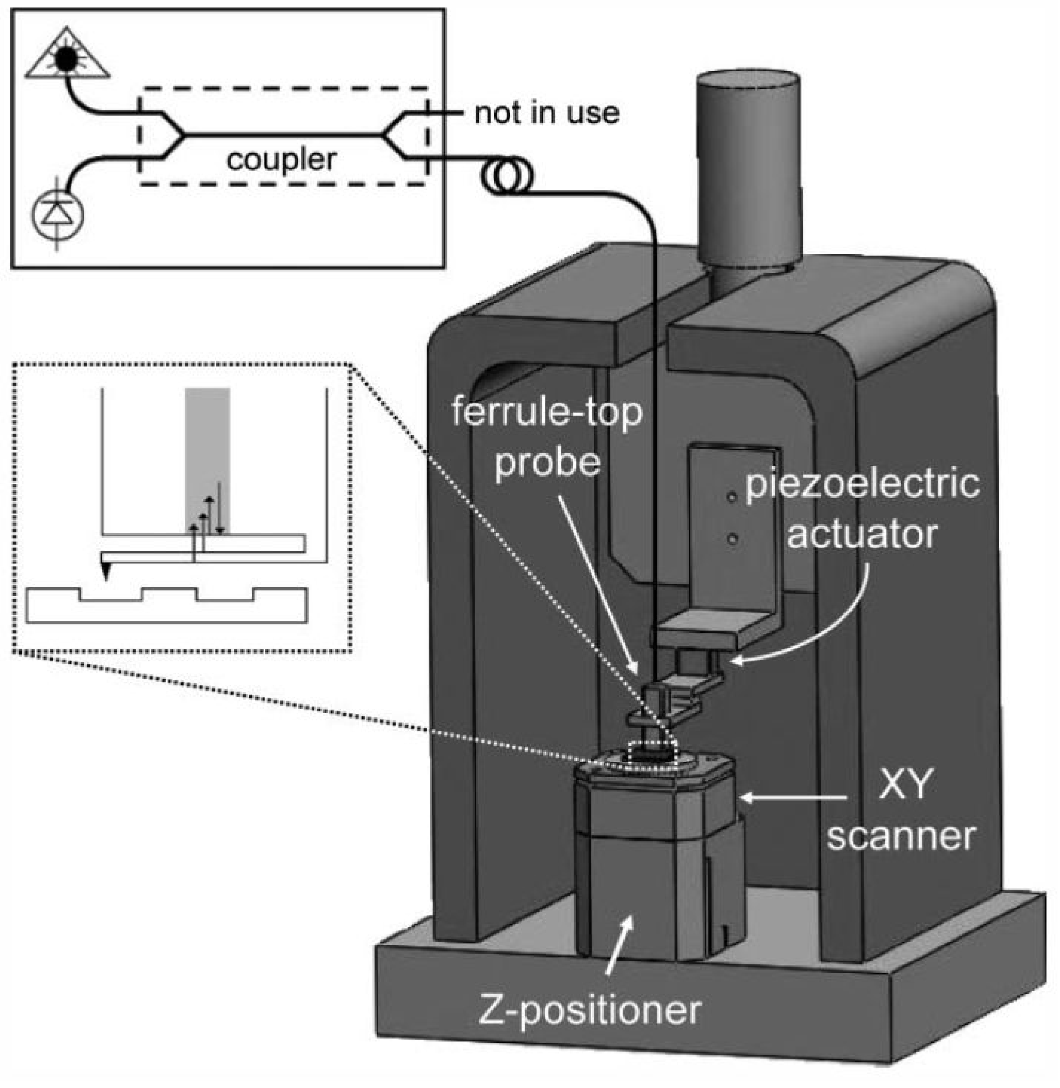

Figure 5.5: Schematic view of the ferrule-top AFM.

5.3 Experimental setup

To demonstrate the imaging capabilities of ferrule-top cantilevers, the probe described in the previous section was mounted on the setup sketched in Fig. 5, which consists of a Z-positioner (ANPz51/RES, Attocube AG) with a sample holder, mounted on a 30 μm × 30 μm range XY-scanner (ANSxy50, Attocube AG) in front of a ferrule-top probe holder equipped with a piezoelectric actuator (AE0203D04F, Thorlabs Inc.). The Z-positioner can be used in stick-slip mode (which moves the sample in discrete steps) or as a standard piezoelectric translator (which allows continuous displacement). To facilitate assembly, the probe is glued to a thin 5 mm × 10 mm iron plate, which is anchored to the holder by means of a small magnet. To reduce acoustic and seismic noise, the entire assembly is mounted on an active vibration isolation stage (Nano-20, Accurion GmbH) housed inside an anechoic box. Thanks to the combined use of ferrule-top technology and compact scanners and positioners, the whole AFM can be contained in a 5 cm × 5 cm × 7 cm volume, and, with an accurate design, can be miniaturized even further.

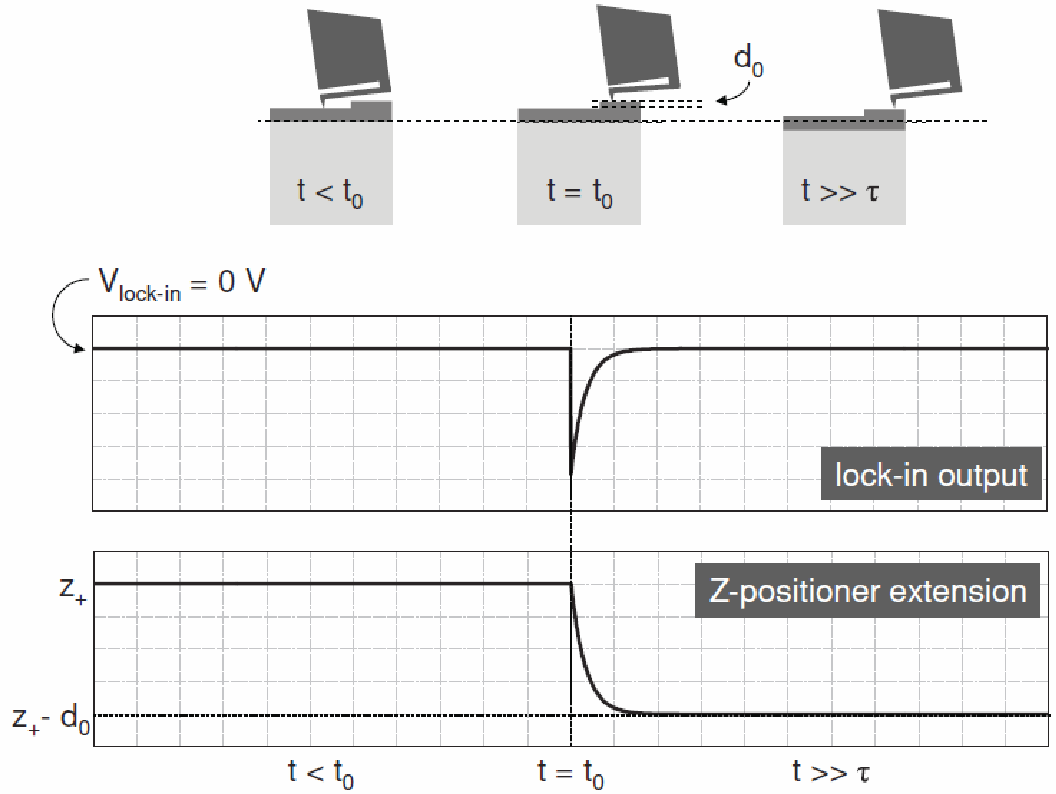

Figure 5.6: Schematic view of the working principle that lies at the heart of the high gain feedback loop used in our ferrule-top AFM.

5.4 Control system

To obtain a contact mode image, the operator first moves the Z-positioner in a series of discrete stick-slip steps that bring the sample in contact with the sharp conical tip of the ferrule-top cantilever. This procedure is extremely simple, because upon contact, the cantilever undergoes static bending, which is readily detected by the interferometer. Once in contact, the XY-scanner moves the sample underneath the tip to allow raster scan of the area of interest, while a feedback circuit keeps the cantilever deflection constant by moving the sample in the vertical direction, like in standard close loop AFMs.

To close the loop, one could simply fix the set point in correspondence to a position where the cantilever is in quadrature, and then adjust the vertical position of the sample to keep the output signal of the interferometer constant. Following this method, however, the image might be affected by spurious features that are caused by power fluctuations of the laser of the interferometer, which would give rise to signals that would mimic cantilever deflections. This systematic effect can be avoided by using a different feedback method designed to lock the set point not to quadrature but to a maximum or a minimum of interference. In this way, the set point is not defined in terms of absolute voltage output of the interferometer, but as the position where the first derivative of the signal vanishes, which is independent from the output power of the laser. To lock to a maximum or a minimum of interference, the probe is sinusoidally excited in the vertical direction by means of the piezoelectric actuator of the probe holder at a frequency below the resonance frequency of the cantilever (like in some force modulation techniques already described in the literature)[101]. The amplitude of the oscillation is much smaller than the static bending of the cantilever at the set point. Therefore, the tip never loses contact with the surface. This vertical motion is at the heart of the feedback loop that eventually allows one to obtain accurate images of the sample, as explained in detail here below (see Fig. 5.6). Lets suppose that, after contact, the Z-positioner, now working in piezoelectric scanning mode, is extended over a length equal to z_+ for which the interference signal is maximum. Lets then assume that the excitation signal of the probe holder is switched on and that, during the XY-scan, the probe initially moves on a flat surface (no change of the output signal). Lets finally imagine that at $t = t_0$ the cantilever is bent upward (or downward) of a small amount d_0 because of the presence of a step in the sample. If one neglects the inertia of the cantilever and the rising time of the readout, the output signal observed is described by [see Eq. 5.1]

$$W\left(t\right) \approx W_0\left(1+V\right) - \frac{1}{2}W_0 V\left(\frac{4\pi}{\lambda}\right)^2 \times \left(d_0 - z_+ + \delta cos(\omega t)\right)^2 \tag{5.2}$$

where ω and δ are, respectively, the angular frequency and the modulation amplitude of the cantilever in response of the oscillation of the probe holder.

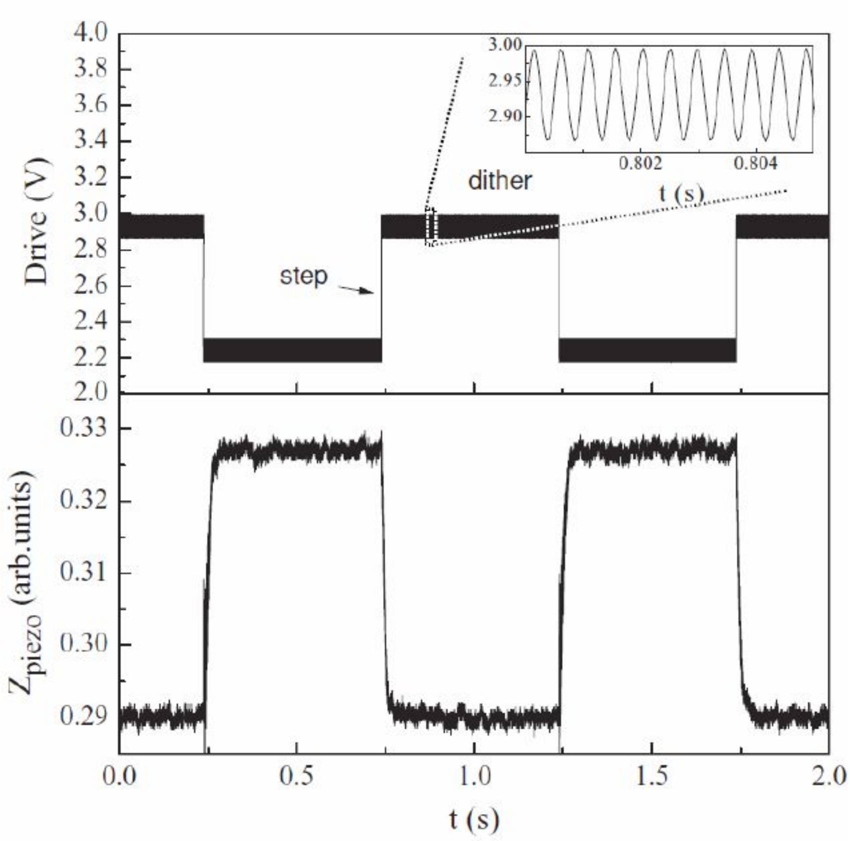

Figure 5.7: Movement of the Z-positioner in response to a driving signal that simulates an ≈25 nm sharp step.

From Eq. 5.2, one can see that $W(t)$ is the sum of one time independent term, one 1ω term, and one 2ω term.

$$W\left(t\right) \approx C_0 + C_1 d_0 cos(\omega t) + C_2 cos(2\omega t) \tag{5.3}$$

where the exact expressions of C_0 and C_2 are not relevant for the description of the method, and $C_1(d_0)$ is given by

$$C_1(d_0) = W_0 V \left(\frac{4\pi}{\lambda}\right)^2 (d_0 - z_+)\delta \tag{5.4}$$

To close the loop, the readout output is sent to a lock-in amplifier locked at frequency ω. The output of the lock-in amplifier is further amplified and sent to the power supply of the Z-positioner. The extension of the Z-positioner at a generic instant t is thus equal to

$$z(t) = \frac{G}{G+1}(z_+ - d_0(1 - e^{-\frac{(t-t_0)}{\tau}})) \tag{5.5}$$

where G is the loop gain and τ is the loop time constant. From Eq. 5.5, it is evident that with sufficiently high gain one can accurately reconstruct the image of the sample by looking at the extension of the Z-positioner as a function of the XY-coordinate, and that, in principle, high speed rates can be achieved if the time constant is sufficiently low. In our instrument, the loop gain and the time constant are set to 80 and 135 μs, respectively. However, we observed that, when driven at high frequencies, our Z-positioner suffers from severe mechanical oscillations that decrease the image quality. For this reason, we have intentionally limited the maximum output current of the amplifier that feeds the Z-positioner. This expedient decreases the scanning speed, but eliminates all the mechanical problems. For example, in Fig. 5.7 we show the movement of the Z-positioner in response to a driving signal that simulates an ≈25 nm sharp step. From that graph one can see that, indeed, the positioner does not suffer from mechanical oscillations. The response time is, however, limited by a 15 ms long rising time and a 10 ms falling time.

5.5 Contact mode imaging

In Figs. 5.8(a) and 5.8(b) we report images of a 23 nm high calibration grating (NT-MDT TGZ1) obtained in air and water, respectively. For the latter, the grating was attached to the bottom of a small Petri dish filled with water. Each image covers an area of 7 μm × 4 μm (resolution 120 pixels × 70 pixels) with scan time of ≈12 minutes. The two images were obtained with two different cantilevers, whose resonance frequencies in atmospheric conditions were independently determined to be 4.9 kHz and 6.2 kHz, respectively. Those

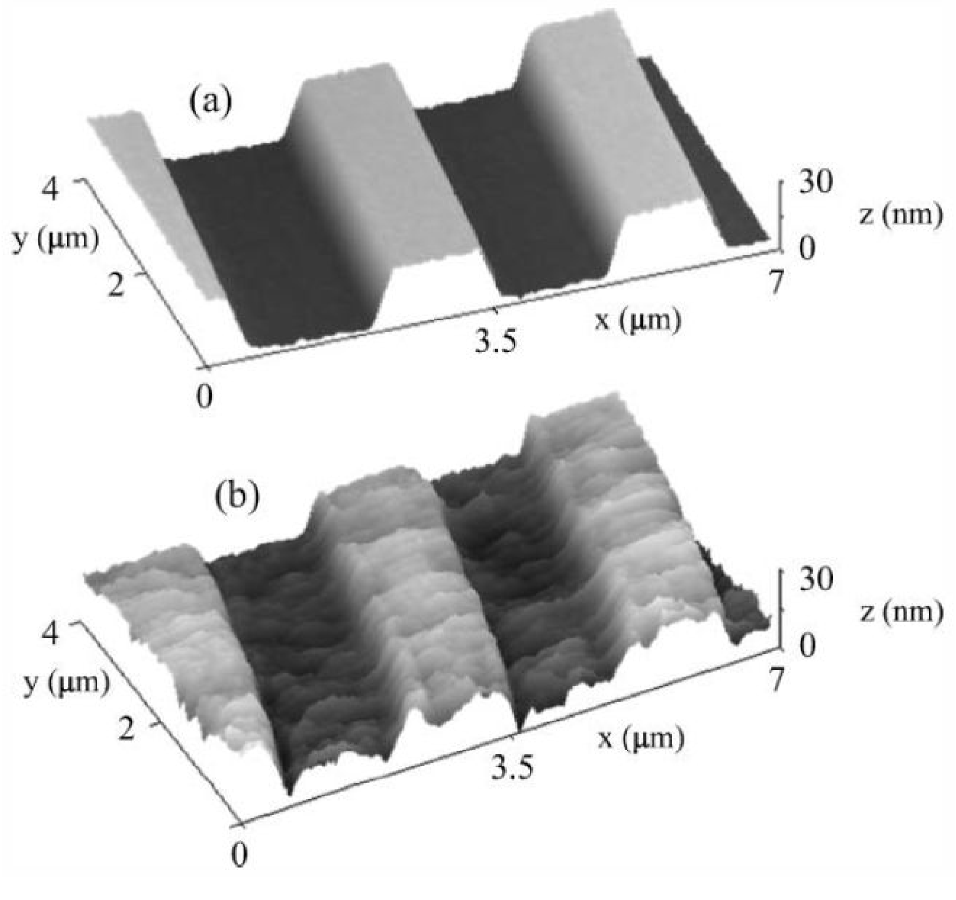

Figure 5.8: AFM images of a calibration grating obtained with our ferrule-top AFM in (a) air and (b) water. Images were processed using Gwyddion software with implementation of only standard plane leveling and line correction (see Ref. [102]).

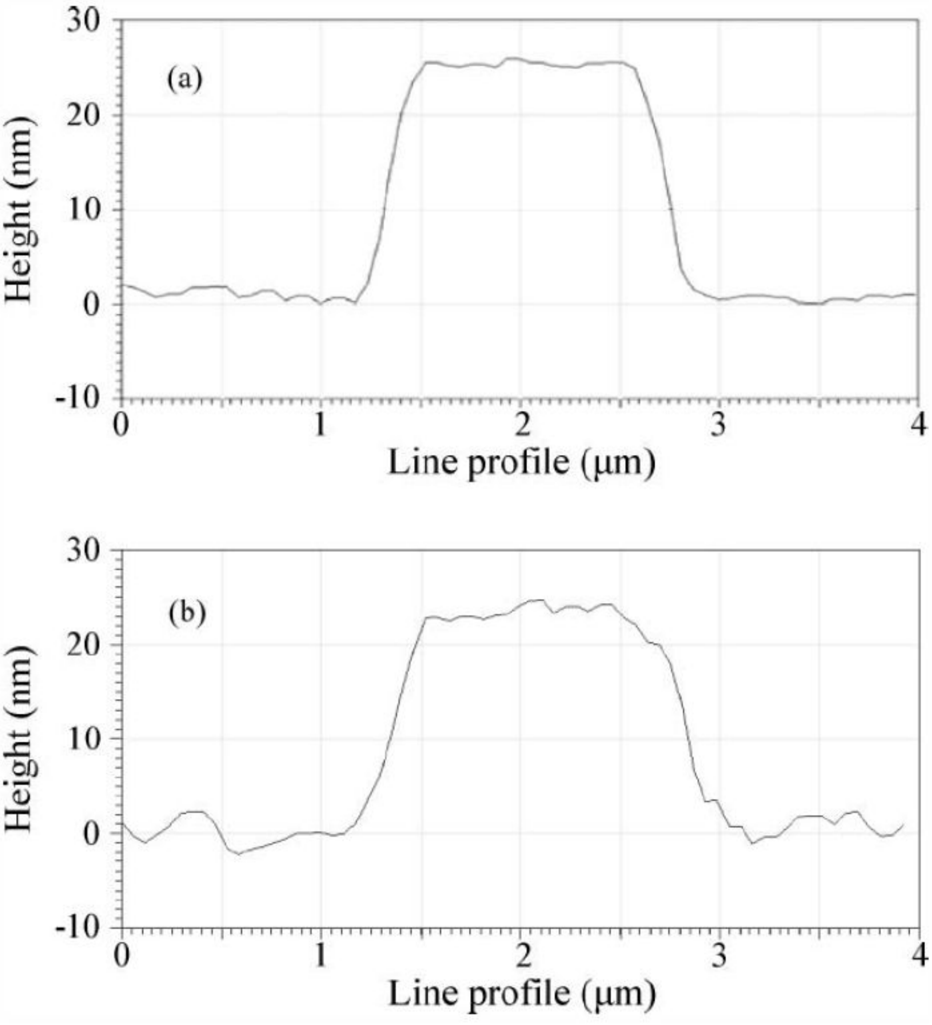

Figure 5.9: Line-scan of the AFM images reported in Fig. 5.8: (a) in air, (b) in water.

values correspond to spring constants of approximately 8 N/m and 15 N/m. Since the feedback mechanism needs, in the worst case scenario, a cantilever deflection of $\lambda/4$ to engage at a maximum or a minimum of interference, the force applied onto the sample during the scan was anyway less than 7.2 μN and 13.5 μN, respectively. The frequency of the vertical oscillation that lies at the heart of the feedback loop was set to 1.1 kHz, with amplitude equal to 15 nm in air and 35 nm in water. From the images reported in Figs. 5.8(a) and 5.8(b), it is clear that the instrument can correctly reproduce the shape of the calibration grating. The line-scans reproduced in Fig. 5.9 further confirm that the quality of the image is comparable to that of commercial AFMs. Indeed, by analyzing the data recorded while the probe was scanning a flat region of the sample, one can see that the rms of the data distribution (that include the effects of vibrations and surface roughness) is equal to 0.5 nm for the image in air and 1.8 nm for the image in water. The slightly higher value obtained in water can be attributed to the presence of small turbulence around the probe, which increases vibrations and, therefore, noise.

5.6 Conclusions

We have fabricated a tipped ferrule-top cantilever for AFM purposes. We have demonstrated that this new kind of probe allows the implementation of very compact, all-optical, triangulation-free AFMs. Thanks to the monolithic design of ferrule-top technology, the user can quickly engage the scanning tip, regardless of the environment in which the sample is immersed. The instrument can then provide high quality images in both air and liquids. We believe that our work paves the way for a new generation of AFMs that are very easy to use, and thus adapt well to utilization in as well as outside research laboratories.

Acknowledgments – This work was supported by the European Research Council under the European Communitys Seventh Framework Programme (FP7/2007-2013)/ERC grant agreement number 201739 and by the Netherlands Organisation for Scientific Research (NWO) under the Innovational Research Incentives Scheme VIDI-680-47-209.

Chapter 6

Measurement of the Casimir force with a ferrule-top sensor

We present a Casimir force setup based on an all-optical ferrule-top sensor. We demonstrate that the instrument can be used to measure the gradient of the Casimir force between a gold-coated sphere and a gold-coated plate with results that are comparable to those achieved by similar atomic force microscope experiments. Thanks to the monolithic design of the force sensor (which does not require any optical triangulation readout) and to the absence of electronics on the sensing head, the instrument represents a significant step forward for future studies of the Casimir effect under engineered conditions, where the intervening medium or the environmental conditions might be unsuitable for the use of more standard setups.

This chapter is based on paper:

P. Zuurbier, S. de Man, G. Gruca, K. Heeck and D. Iannuzzi, *New Journal of Physics* **13**, 023027, (2011)

6.1 Introduction

Long-range surface interactions are of paramount importance in the design of micro- and nanoelectromechanical systems (MEMS and NEMS), as they determine the minimum separation that two miniaturized mechanical pieces can reach before they snap to contact. It is thus not surprising that, over the last decade, an ever increasing number of groups have been drawing the attention of the scientific community to the potential relevance of the Casimir effect in nanotechnology [103, 104] and what currently goes under the name of *quantum fluctuations engineering* – the possibility of tailoring the Casimir force with a suitable choice of the shape and material properties of the interacting objects and the medium between them [105–112][1]. Driven by this trend, scientists have developed a wide variety of instruments that can assess different aspects of this interaction mechanism. Macroscopic setupscote [115–118] and micromachined torsional balances [119–121] are typically optimized for utilization in a vacuum or air, but would hardly work in liquids. Experiments in a vacuum can also be performed by means of custom-made atomic force microscopes (AFMs) [122, 123], which, after proper modification, can be also used to measure the Casimir force in gaseous environments [110] or in liquids [109]. Because AFMs rely on optical triangulation, however, it is difficult to imagine a universal measuring head that can easily adapt to different environments, ranging, for example, from low-temperature vacuum to room temperature liquids. Earlier this year, our group proposed overcoming this issue by replacing the AFM head with an all-optical micromachined torsional force sensor that adapts well to both vacuum and critical environments [124]. The sensor is based on fiber-top technology [7]. It consists of a mechanical rectangular beam carved out of the cleaved end of a standard single mode optical fiber. The beam is suspended a few microns above the rest of the fiber by means of two lateral torsional rods. The light coupled from the opposite end of the fiber allows one to measure the tilting angle of the rectangular beam and, therefore, the force that makes it tilt. Thanks to its monolithic design and the absence of electronics on the sensing element, this micro–opto–mechanical balance can in principle be used in any environment without any change of the readout mechanics, optics or electronics. Unfortunately, however, preliminary experiments show that, as soon as measurements are not carried out in a vacuum, the sensor can only be used in static mode [124]. Dynamic modes, which are typically more sensitive, are in fact disturbed by spurious effects induced by the hydrodynamic force between the mechanical beam and the fiber below (a phenomenon that goes

---

[1] Over the last 30 years, there has been much more extensive activity focused on the investigation of the van der Waals interaction in the non-retarded limit, with particular emphasis on liquid environments, and there are important examples in which the investigation has been extended to the retarded part of the interaction. A complete review of that part of the literature is beyond the scope of this paper. See [113, 114] for more details.

under the name of squeezed field air damping [125]). Furthermore, because the optical fiber is only 125 μm in diameter, fiber-top devices are typically fabricated with an expensive and time-consuming technique (such as focused ion beam (FIB) milling [8]). Fiber-top technology cannot thus be considered as a practical solution for systematic measurements, where, due to recurrent accidental damaging of the force sensor, one must rely on probes that can be easily replaced. To overcome the fabrication issue of fiber-top devices, we recently introduced a novel approach that preserves the flexibility of fiber-top technology while reducing manufacturing costs and production time: the ferrule-top cantilever [51]. To fabricate a ferrule-top cantilever, a standard single-mode optical fiber is glued inside the bore hole of a much bigger pierced ferrule. The fiber and the ferrule are so well held together by the glue that they behave like a single mechanical piece. The ferruled fiber is thus equivalent to a very large single-mode optical fiber that can now be milled in the form of a cantilever by means of more convenient techniques (e.g. laser ablation). Interestingly, because of the larger dimensions of the building block, the gap between the cantilever and the remaining part of the ferrule is typically much larger than in fiber-top devices. Ferrule-top cantilevers are thus supposed to suffer considerably less from hydrodynamic problems than fiber-top sensors. In this paper, we present a ferrule-top force setup designed to measure the Casimir attraction between a sphere and a flat plate, and we demonstrate that one can indeed perform precise measurements of the Casimir force between a sphere and a plate kept in air with a dynamic detection scheme that does not induce any spurious effects.

6.2 Introduction

The experimental setup presented in this paper is designed to measure the Casimir force between a 200 μm diameter sphere and a plate as a function of separation in a distance range between approximately 50 and 200 nm. The force sensor is realized according to the scheme sketched in figure 6.1. A pierced 2.5 mm × 2.5 mm × 7 mm rectangular ferrule, made of borosilicate glass, is initially carved by means of laser ablation in the form of a cantilever that stretches over one of the diagonals of the edge of the ferrule. At the end of the milling process, a small amount of transparent epoxy is dropped and cured inside the 127 μm diameter hole left open at the center of the cantilever, while a standard single-mode optical fiber is slid into the hole of the ferrule from the other side and glued with the cleaved end at approximately 100 μm from the bottom surface of the cantilever. A 200 μm diameter sphere is then attached to the top of the free-hanging end of the sensor by means of a small droplet of UV curable epoxy. The sensor and the sphere are finally coated with a 5 nm thick Cr adhesion layer followed by a 200 nm thick Au film. The

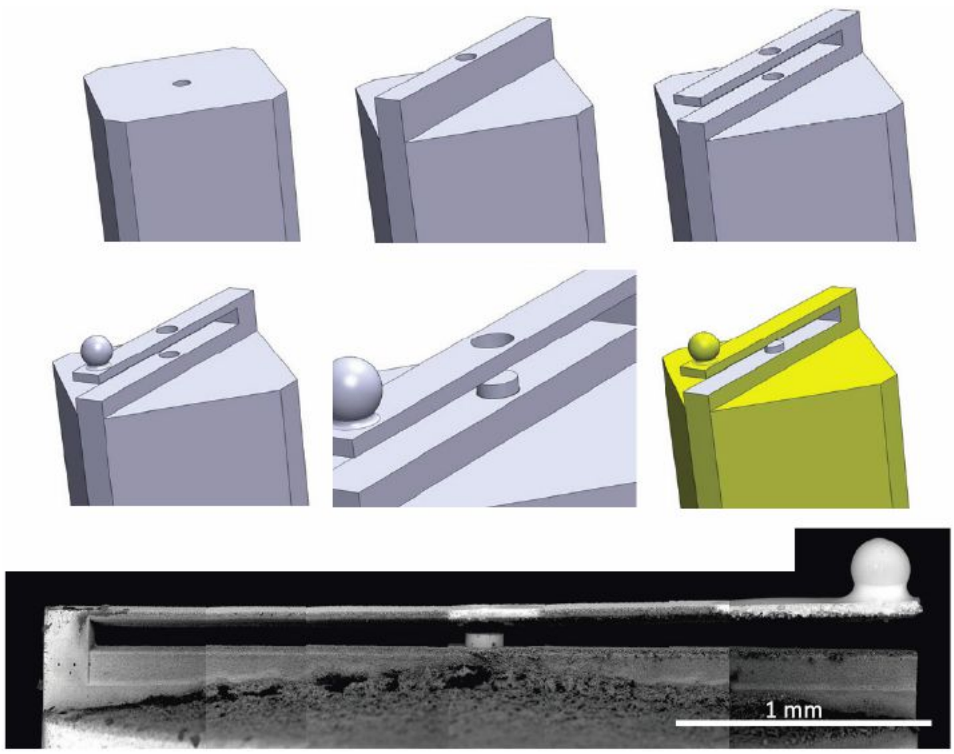

Figure 6.1: Fabrication steps followed to manufacture a ferrule-top cantilever for Casimir force measurements. The building block is a pierced 2.5 mm × 2.5 mm × 7 mm rectangular ferrule made of borosilicate glass. The ferrule is machined in the form of a rectangular cantilever, which is then equipped with a spherical bead. An optical fiber slid through the central hole and glued to the ferrule allows the detection of cantilever deflections by means of interferometric techniques. The bottom figure is a composite of six scanning electron microscope images showing the device used in the experiment described in this paper.

ferrule-top device is anchored on top of a manual translation stage, just in front of a gold-coated sapphire plate that is attached to a piezoelectric stage (see figure 6.2). The manual manipulator allows a first coarse approach of the sensor towards the plate, while the piezoelectric stage is used for the actual scanning during the force-versus-distance measurements. The translational stage also hosts a bare cleaved optical fiber, parallel to the ferrule-top sensor, that is used to measure movements of the piezoelectric stage. The setup is fixed to a block of aluminum that is kept at a fixed temperature by means of four resistors controlled via a feedback circuit. To reduce acoustic and seismic coupling to the environment, the whole instrument is mounted on a silicone pad inside an anechoic chamber on top of a marble table equipped with passive vibration damping blocks. To simultaneously measure the deflection of the ferrule-top cantilever and the motion of the piezoelectric stage, we built two fiber optic interferometers that are fed with the same laser source (Thorlabs Pro800 chassis with a WDM tunable laser module (1552.48–1554.18 nm)) (see Fig. 6.2). The laser light is split by a 50/50 optical fiber coupler into two forward branches. In both forward branches, the light is then split again by 90/10 couplers and sent toward the ferrule-top cantilever and the bare cleaved fiber. For the ferrule-top sensor, the light is reflected by the fiber-to-air, air-to-glue and glue-to-gold interfaces. The amount of light traveling backwards into the fiber is given by:

$$W\left(d_{gap}\right) = W_0\left[1 + V cos\left(\frac{4\pi d_{gap}}{\lambda} + \phi_0\right)\right] \tag{6.1}$$

where d_{gap} is the distance between the fiber end and the cantilever, W_0 is the mid-point interference signal, V is the fringe visibility, λ is the laser wavelength and ϕ_0 is a phase shift that only depends on the geometry of the cantilever [51]. This reflected light travels back into the fiber and is split again by the coupler, which sends part of the signal onto a photodetector (Thorlabs PDA10CS). Reading the current generated on the photodetector, which is proportional to $W(d_{gap})$, one can measure changes in d_{gap} (see equation 6.1) and thus the external forces that have produced those changes. The other branch of the double interferometer works identically to the ferrule-top branch, except that the reflected signal is composed of reflections from the fiber-to-air interface and from the gold mirror, allowing one to measure the relative position of the piezoelectric stage. From equation 6.1, it is clear that it is convenient to operate the force sensor in its quadrature point, where the readout is most sensitive and linear in deflection [43]. For this reason, before each experiment, we first coarsely bring d_{gap} close to quadrature by adjusting the temperature set-point of the setup, which induces differential thermal expansions on the different parts of the ferrule-top device. We then use the tunable laser wavelength to precisely

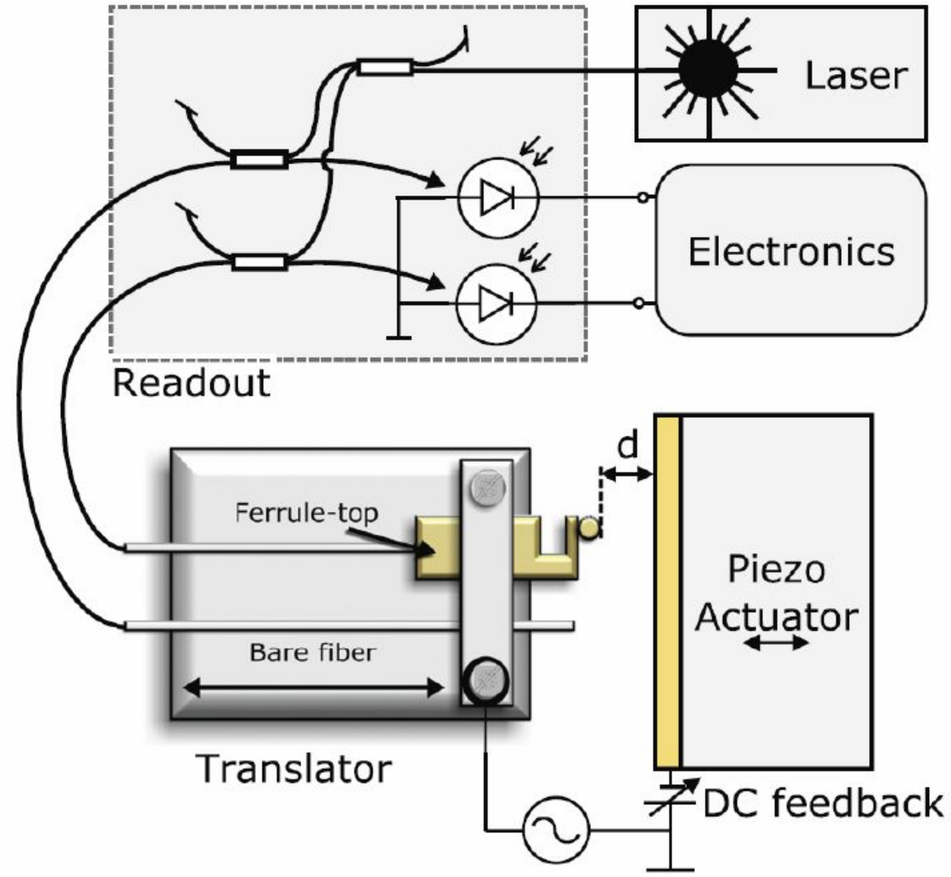

Figure 6.2: Sketch of the experimental setup used to measure the Casimir force between a plate and a sphere attached to a ferrule-top cantilever. The ferrule-top cantilever is anchored to a translational stage that allows one to coarsely move the sensor with the sphere close to the plate. The plate is attached to a piezoelectric stage for fine-tuning the separation between the two interacting surfaces. A bare fiber is anchored parallel to the force sensor and is used to measure movements of the piezoelectric actuator via interferometric techniques. An electronic circuit supplies an ac voltage between the sphere and the plate, which allows one to compensate for the residual electrostatic force and calibrate the force sensor. The setup is mounted on an aluminum block kept at a fixed temperature inside an anechoic box and isolated from the surroundings with passive vibration dampers (not shown).

tune to the quadrature point[2]. Casimir force measurements are carried out following a method similar to that described in [110, 126], which allows one to simultaneously calibrate the instrument, counterbias the electrostatic potential difference that exists between the sphere and the plate and measure the gradient of the Casimir force as a function of separation. In a nutshell, while slowly changing the separation between the sphere and the plate by means of the piezoelectric stage, we supply an ac voltage to the sphere with frequency ω_1 much smaller than the resonance frequency of the force sensor. This ac voltage gives rise to an electrostatic force that makes the cantilever oscillate. The mechanical oscillation has one component at ω_1 and one component at $2\omega_1$. The ω_1 component drives a negative feedback loop that compensates for the contact potential difference that exists between the sphere and the plate, while the $2\omega_1$ component allows one to calibrate the instrument and to measure the separation between the interacting surfaces. On top of the electrostatic force modulation, we add a small oscillatory motion to the piezoelectric stage at a frequency ω_2 that lies somewhere between ω_1 and $2\omega_1$. From the in-phase motion of the cantilever at ω_2, we can finally measure the gradient of the force between the sphere and the plate. For details of the experimental method, see [110, 126]. It is, however, important to stress that, contrary to the piezoelectric stage of the setup presented in [110, 126], the one used in this experiment is driven via an open loop circuit and is not equipped with any internal calibration sensor. For this reason, we have implemented a slightly different method to determine the separation between the two surfaces. To explain this new approach, we first note that the electrostatic force generated by the ac voltage is equal to

$$\frac{F_e}{R} = \frac{\epsilon_0 \pi \left(V_{ac} cos\left(\omega_1 t\right) + V_0\right)^2}{d} \tag{6.2}$$

where ϵ_0 is the permittivity of air, R is the radius of the sphere and V_0 is the residual potential difference. Therefore, the mechanical oscillation induced by the electrostatic force on the force sensor at $2\omega_1$ gives rise to a $2\omega_1$ signal on the photodiode of the interferometer that scales like $S_{2\omega_1} \propto V_{ac}^2/d$. The proportionality constant can be measured by looking at the output signal of the bare fiber interferometer. We know in fact that, when the bare fiber interferometer signal has moved through exactly one interference fringe, the plate has moved for exactly $\lambda/2$. Once the proportionality constant β is known, one can extract d from $d = \beta \cdot V_{ac}^2/S_{2\omega_1}$.

---

[2] The 1.7 nm wavelength variation spanned by our laser source alone is not always sufficient to adapt the laser wavelength to the actual length of the fiber-to-cantilever gap.

6.3 Results and discussion

The sensor used for the data presented below was a 3.4 mm long, 200 μm wide and 40 μm thick ferrule-top cantilever (resulting in an expected spring constant of $\approx$2 Nm^{-1}) with $\approx$100 μm ferrule-to-cantilever gap (see the scanning electron microscope image of Fig. 6.1). The resonance frequency was measured independently, and resulted to be equal to 2.7 kHz, with a Q-factor of 42. In Figs. 6.3 and 6.4, we show the results of a typical measurement run. Data were gathered during ten consecutive back-and-forth scans. Each scan had a duration of 1000 s and a stroke of 1 μm spanned by applying a driving voltage to the piezoelectric stage of the form $V_{PZT} \propto 1-|\tau_s-1|^3$, with $\tau_s = 500$ s. The frequency of the ac voltage was set to $\omega_1 = 72$ Hz. Its amplitude was continuously adjusted during the scan to keep the root mean square (rms) of the $2\omega_1$ electrostatic force component equal to roughly 230 pN at all separations (see [110, 126]). The oscillation frequency of the piezoelectric stage was set to $\omega_2 =$ 119 Hz with 7.2 nm amplitude. Signals at $2\omega_1$ and ω_2 were demodulated with two lock-in amplifiers equipped with a 24 dB low-pass filter with RC time of 200 and 100 ms, respectively. To avoid mixing of the Casimir signal with that induced by the hydrodynamic force due to the air in the gap [110], the phase of the ω_2 lock-in amplifier was aligned with the phase of the oscillatory motion by going to contact, where the plate and the cantilever move synchronously. This procedure was performed only once before starting the measurement run. Figure 6.3 shows the potential difference V_0 needed to minimize the electro-

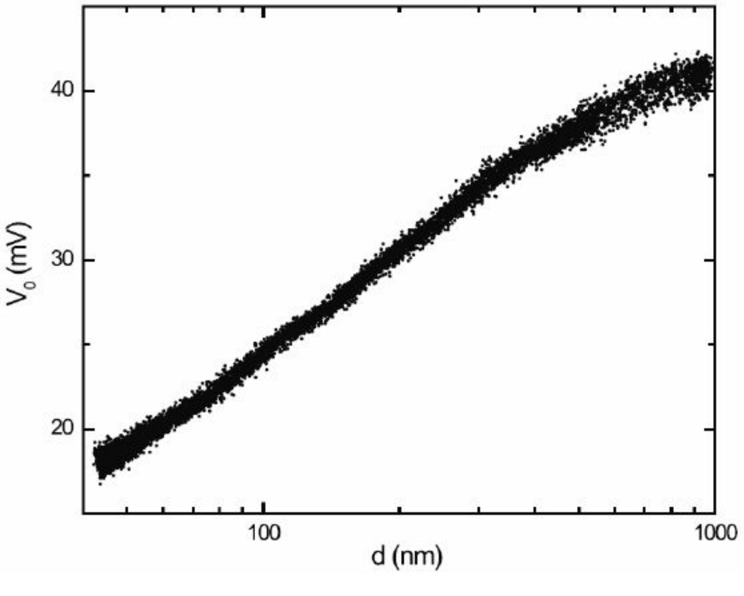

Figure 6.3: Measurement of the residual potential between the interacting surfaces as a function of separation as obtained during ten consecutive scans.

static interaction between the sphere and the plate as a function of separation d. The observed spread in the data is due to measurement noise and not to a time-related drift. It is clear that the data loosely follow a behavior like a $\log(d + b)$, as observed before in [116, 126] and [127]. This dependence is not yet fully understood. Figure 6.4 shows the Casimir force gradient as a function of separation. The data were obtained by subtracting from the original data an electrostatic contribution that arises from the calibration procedure [110]. This contribution, which scales like $1/d$, can be accurately calculated from the value of $S_{2\omega_1}$. In our experiment, this correction ranged from 15 Nm^{-2} at 200 nm to 70 Nm^{-2} at 45 nm. The gray line in the graph represents the theoretical Casimir force as computed from the Lifshitz equation, where we have assumed that the dielectric function of the gold surfaces can be obtained by combining the tabulated data of [128] with the Drude term described in [129] and where we have neglected surface roughness corrections. The theoretical result should thus not be taken too rigorously. It is known, in fact, that gold

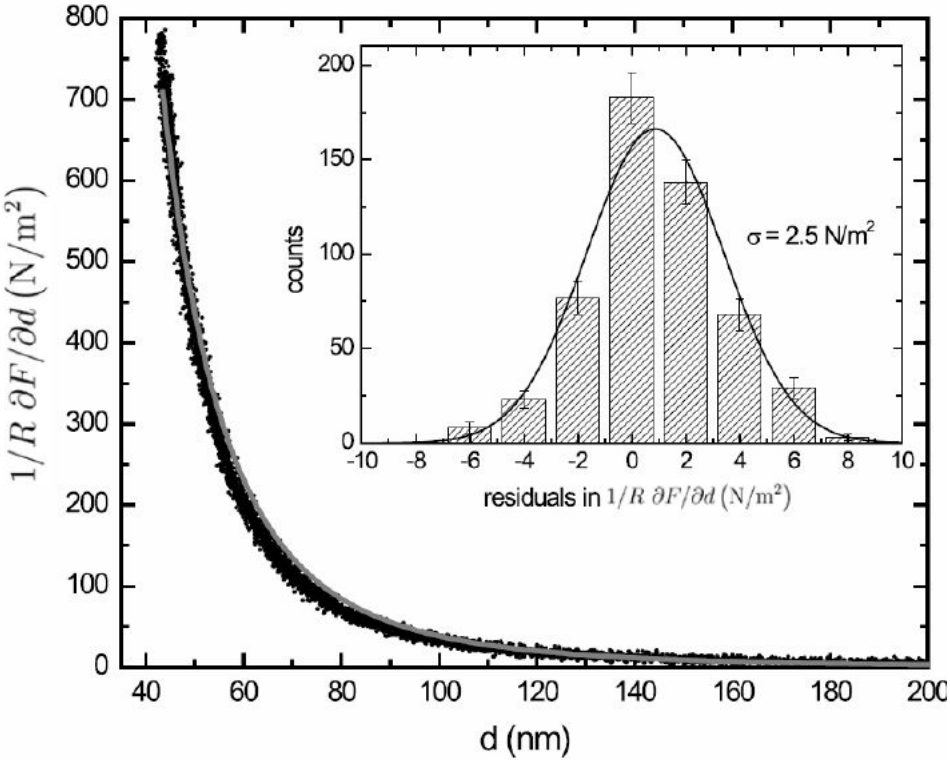

Figure 6.4: Dots: measurements of the gradient of the Casimir force between the sphere and the plate (normalized to the radius of the sphere) as a function of separation as obtained during ten consecutive scans. The gray line represents the result expected from theory. Inset: histogram of the residuals of the data between 160 and 200 nm.

layers deposited with different methods may have different optical properties, which can lead to significant differences in the resulting Casimir force [130]. Furthermore, surface roughness corrections can be as high as several tens of per cent at the closest separations. A more refined calculation of the expected force is, however, beyond our scope. The goal of this paper, in fact, is not to improve the accuracy in the comparison between theory and experiment, but to prove that ferrule-top cantilevers can be successfully used to obtain precise (i.e. low noise, small statistical error in force gradient) Casimir force measurements.

It is thus now important to discuss the statistical error in the Casimir force gradient. The inset of figure 6.4 shows a histogram of the residuals of all the Casimir force data collected in the separation range between 160 and 200 nm. The standard deviation is equal to 2.5 Nm^{-2}. For comparison, our state-of-the-art AFM for Casimir force measurements is currently capable of achieving a standard deviation of 1.75 Nm^{-2} [131] with an ω_2 oscillation amplitude a factor of 2 lower but an integration time ten times higher.

6.4 Conclusions

We have presented a ferrule-top sensor for Casimir force experiments. The sensor is based on a monolithic miniaturized cantilever that is coupled to a remote readout via optical fibers. We have demonstrated that the setup provides measurements of the Casimir force between a sphere and a plate by means of a dynamic detection scheme. The sensor can be easily fabricated with cost-effective techniques, allowing frequent substitution of the probe in systematic experiments. Furthermore, it adapts well for utilization in harsh environments, such as low temperatures, vacuum and liquids. Similar ferrule-top devices can of course be used to investigate other longrange interaction mechanisms as well. Ferrule-top technology can thus be considered as a new tool for exploring phenomena that are of relevance in the future development of MEMS and NEMS.

Acknowledgments – This project was supported by the European Research Council under the European Communitys Seventh Framework Programme (FP7/2007-2013)/ERC grant agreement number 201739 and by the Netherlands Organisation for Scientific Research (NWO) under the New Journal of Physics 13 (2011) 023027 (http://www.njp.org/)Innovational Research Incentives Scheme Vernieuwingsimpuls (VIDI-680-47-209). The authors acknowledge useful discussions within the community supported by the ESF Research Network CASIMIR.

Chapter 7

Numerical study of a ferrule-top cantilever optical fiber sensor for wind-tunnel applications and comparison with experimental results

We present a numerical analysis of an air flow velocity sensor based on a fiber-optic ferrule-top cantilever. The device forms a low-finesse Fabry-Perot interferometer, with one of the two reflecting surfaces constituted by a cantilever beam. Under the effect of the flow pressure, the cantilever bends producing a change in the cavity length of the Fabry-Perot and therefore a modification of its optical response. The numerical analysis, performed by use of finite-element method (FEM), is then compared with a set of experimental results obtained in a small wind-tunnel.

This chapter is based on paper:

A. Cipullo , G. Gruca, K. Heeck, F. De Filippis, D. Iannuzzi, A. Minardo, L. Zeni, *Sensors and Actuators A* **178**, 17-25, (2012)

7.1 Introduction

Low-speed air flow measurement is a topic of great interest in several industrial and research areas, such as aeronautics, applied fluid dynamics and turbomachinery. A significant number of well-established techniques exist to perform single-point and field measurements, either intrusively or non-intrusively. Pitot tubes, for instance, coupled with pressure transducers are rugged and easy-to-use devices, especially suited for single-point (or multiple-points, using rakes) measurements. When high bandwidths are required to detect flow turbulences, single-point techniques such as hot-wire anemometry or laser Doppler velocimetry (LDV) are commonly used. Due to their compact sensing region, both techniques are also often preferred when velocity profiles must be determined close to surfaces and walls. Contrary to hot-wire anemometry, LDV is non-intrusive. However, it normally requires the flow to be seeded with scattering particles. When field measurements (both 2D and 3D) are needed, particle image velocimetry (PIV) is a common choice. PIV is again a non-intrusive technique, but requires seeding of the flow as well. A deeper overview on the mentioned techniques can be found, for instance, in Ref. [132] and in the references therein. We propose an alternative single-point intrusive technique based on a ferrule-top cantilever optical fiber sensor. The device behaves as a low-finesse Fabry-Perot interferometer, with the cavity length changing when the cantilever bends. Air flow across the cantilever causes deformation of the cantilever, and therefore a change of the optical reflectivity of the interferometer. The main advantages of such device are the sensitivity (due to the interferometric readout), the immunity to electromagnetic interferences (it is an all-optical device) and the compactness (the device has the shape of a 1.8 mm diameter cylinder). Note that small air flow sensors are typically preferred in order for minimal obstruction of the air flow [133]. In the following, we first review the fabrication steps required to realize the sensor. We then present the working principle of the sensor and a numerical analysis of the expected performance. The result of the theoretical model are finally compared with a first set of experimental results, obtained during an earlier test campaign [134].

7.2 Fabrication process for ferrule-top cantilever flow sensor

The key steps of device fabrication, as well as a microscope image of the end result, are presented in Fig. 7.1 [51]. First, a Duran borosilicate ferrule with an outer diameter of 1.8 mm is carved in the form of a ridge (Fig. 7.1(a)). The ferrule is then rotated to shape the ridge in the form of a suspended cantilever (Fig. 7.1b). Finally, an SMF-28e Corning single-mode optical fiber (ThorLabs

SMPF0215) is glued inside the ferrule. The milling steps are performed using a 355 nm ps-laser ablation system equipped with a X-Y precision motion stage. Ferrule-top cantilevers are patented devices [135]. A more detailed description of the fabrication process and some potential applications can be found in Refs. [51–53]. The cantilever employed as flow velocity sensor in the experimental tests is 1650 μm long, 30 μm thick and 200 μm wide, while the air gap (i.e. the undercut width) is 100 μm.

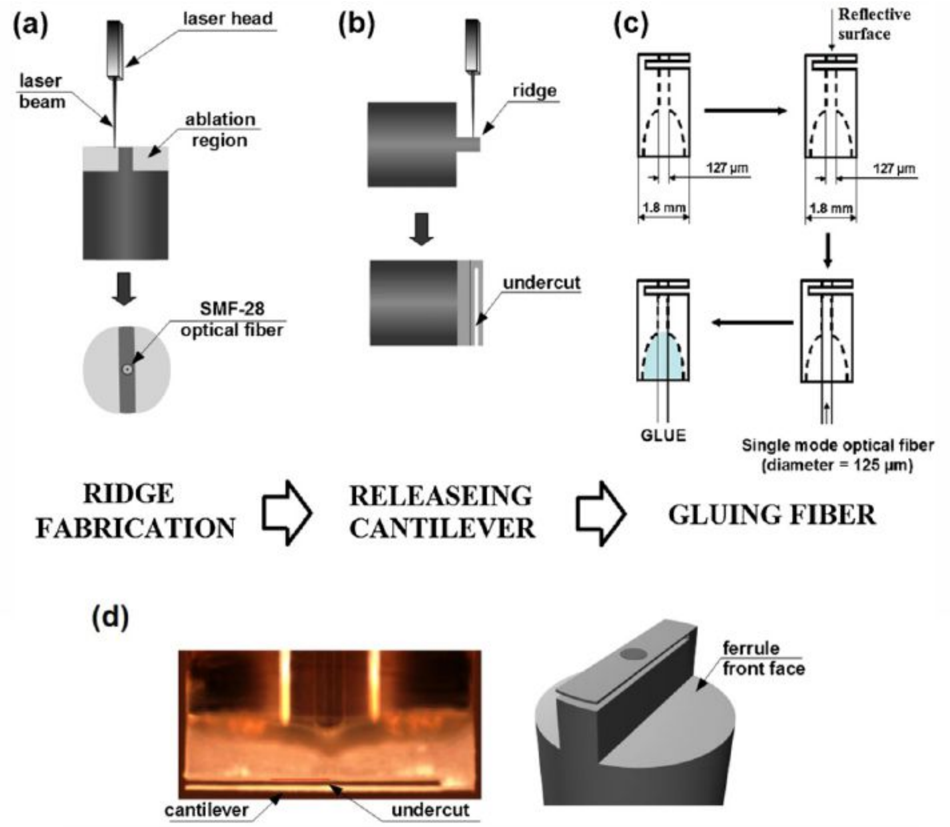

Figure 7.1: (a) and (b) milling steps for ridge and cantilever fabrication; (c) gluing of the fiber into the ferrule; (d) microscope image (side-view) and 3D model of the cantilever fabricated according to the procedure illustrated in (a-c).

7.3 Working principle

In the proposed interferometric readout system, light from a laser diode is coupled to the ferrule-top cantilever by an optical circulator. The latter is also employed to send the light reflected by the sensor device to a photodetector (Fig. 7.2). The light reflected by the ferrule-top device is the result of the optical interference between the light reflected at the fiber/air interface and the light reflected by the cantilever (which in turn is the superimposition of the light reflected by the back and front surfaces of the cantilever) [7].If multiple reflections from the cantilever are neglected, the reflected optical intensity R is a function of the air gap width d, according to the raised cosine function typical of a low-finesse Fabry-Perot interferometer:

$$R\left(d\right) = R_0 \left[1 + V cos\left(\frac{4\pi d}{\lambda}\right) + \varphi_0\right] \tag{7.1}$$

where ϕ_0 is a constant phase shift, and R_0 and V are, respectively, the midpoint interference signal and the fringe visibility [136]. They are defined as:

$$R_0 = \frac{R^+ + R^-}{2} \tag{7.2}$$

$$V = \frac{R^+ - R^-}{R^+ + R^-} \tag{7.3}$$

where R_+ and R_- represent the maximum and minimum interference signal measured by the photodetector. Neglecting polarization effects and assuming that all the reflected optical energy couples back to the input/output fiber, the midpoint reflectivity and fringe visibility can be expressed as:

$$R_0 = r_1^2 + r_2^2(1 - r_1)^4 \tag{7.4}$$

$$V = \frac{2r_1 r_2(1 - r_1^2)}{r_1^2 + r_2^2(1 - r_1)^4} \tag{7.5}$$

where r_1 and r_2 are the Fresnel reflection coefficients at the fiber/air and air/cantilever interfaces. Note that, as r_2 is the combined reflection from both faces of the cantilever, its value depends on the phase difference between the waves reflected by the two faces, being maximum at the wavelengths for which the double-pass phase delay across the cantilever width is a multiple of 2π. Therefore, also fringe visibility is wavelength-dependent: Assuming a typical Fresnel reflection coefficient of 0.2 at both fiber/air and cantilever/air interfaces and a cantilever width of 30 μm, the computed visibility is ≈ 58 % at the operating wavelength of 1.544 μm (the one used in the experiments reported below). According to Eq. 7.1, the readout system is able to remotely sense the mechanical bending (i.e. d changes) induced by the air flow pressure acting on the cantilever (Fig. 7.2), by monitoring the changes in the reflected optical intensity.

7.4 Numerical results

A finite-element-method (FEM) analysis was carried out in order to study the behavior of the cantilever immersed in a flow. In particular, a three-dimensional model of the sensor was studied under the presence of a laminar

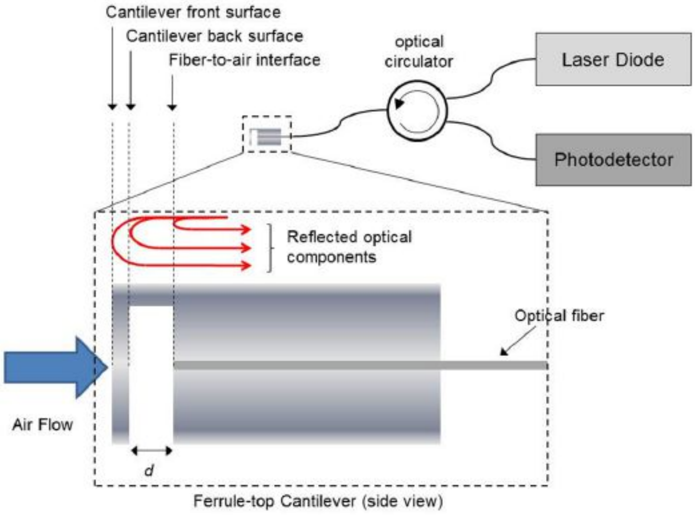

Figure 7.2: Simplified scheme illustrating the ferrule-top cantilever sensor working principle.

air inflow. The fluid dynamics problem was described by the incompressible Navier-Stokes equations, while structural deformations were solved using an elastic formulation. The simulator employed (COMSOL Multiphysics®) allowed us to perform each simulation in two steps: in the first step the fluid pressure field was computed for a given input flow velocity; in the second step the fluid pressure field previously calculated was employed to retrieve the deformations induced on the cantilever member. A preliminary study was conducted to verify that decoupling fluid dynamics from mechanics, while greatly simplifying the computational effort, did not produce any noticeable different result with respect to the coupled case, as a consequence of the relatively small deformations of the cantilever within the considered fluid velocity range (0 m/s 10 m/s). The cantilever dimensions are those of the fabricated device. The ferrule material has been modeled by assuming for Duran a Young modulus of 64 GPa, a material density of 2230 kg/m^3 and a Poissons ratio of 0.20 [137]. Air was modeled assuming a density of 1.205 kg/m^3 and a dynamic viscosity of 1.85·10^{-5} Pa·s (standard conditions of 20^{o}C and 1 atm). The simulation geometry and the unstructured mesh are presented in Fig. 7.3. The computational region is a cylinder having its axis coincident with the one of the ferrule (x-axis). The diameter of the cylinder is 12 mm and its height is 8 mm. A preliminary analysis was carried out to ensure that these dimensions were sufficient to avoid spurious effects on the cantilever behavior due to the cylinder walls. The mesh was made up of about 2·10^5 elements, being denser near the cantilever and coarser in the rest of the geometry. A parametric analysis was carried out by sweeping the air flow input velocity from 0 to 10 m/s. Note that these values refer to the centerline ($y = z = 0$) velocity of the laminar air flow

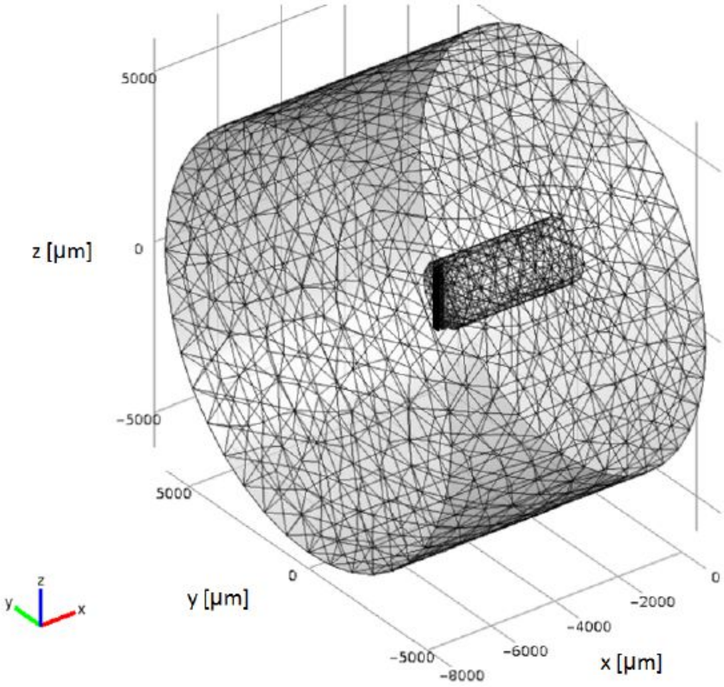

Figure 7.3: Geometry and unstructured mesh used for FEM simulations.

distribution entering the computational window, with the input flow directed toward positive values of the x-axis. As described above, we first calculated the fluid velocity and pressure fields for each fixed input flow velocity. As an example, we report in Fig. 7.4 the velocity magnitude distribution across the x-z plane for $y = 0$, calculated for an input flow centerline velocity of 2 m/s. From the detail on the right of the figure we can note that air velocity goes to zero on the cantilever borders, as a consequence of the non-slip boundary conditions imposed at the walls. Note that the diameter of the cylinder was chosen in order to have a uniform free-stream velocity across the whole cantilever front face. Next, we report in Fig. 7.5 the air pressure field on the cantilever surface and the velocity streamlines for the same input centerline velocity. It is seen that the air pressure reaches its maximum in correspondence of the cantilever front face (where the flow velocity goes to zero), with the fluid velocity streamlines being deviated by the ferrule region. It is interesting to show a zoomed view of the same picture in the region surrounding the cantilever (Fig. 7.6). It is seen that part of the fluid flow enters the undercut area, giving rise to a positive pressure on the back face of the cantilever partly contrasting the pressure at its front face. The effect of the flow entering the undercut can be further appreciated in Fig. 7.7, where the pressure distribution on the $x - z$ plane for $y = 0$ is depicted. The non-negligible pressure in the undercut region counteracts the pressure on the cantilever front face, reducing the cantilever

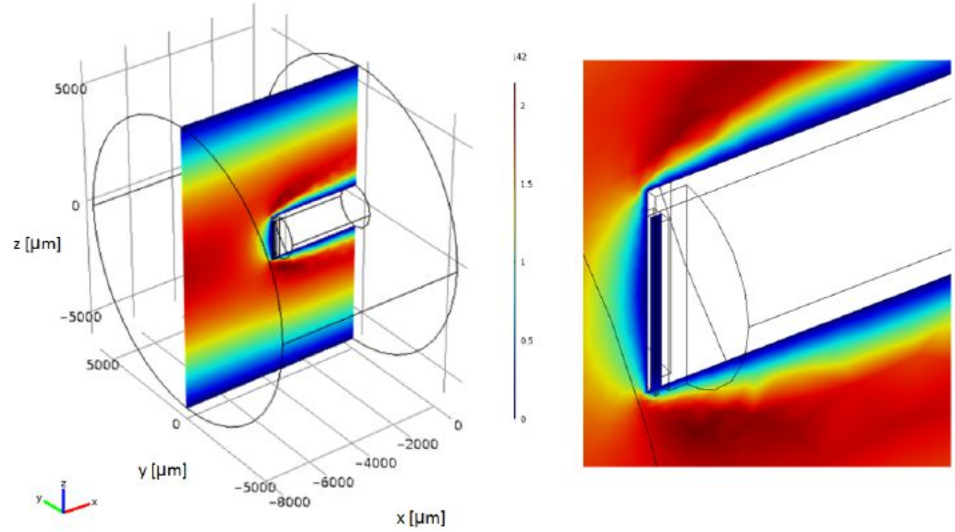

Figure 7.4: Velocity magnitude distribution across the $x - z$ plane for $y = 0$ (left) and detail of the velocity field around the cantilever (right), calculated for an input flow centerline velocity of 2 m/s. The colorbar indicates the velocity in m/s.

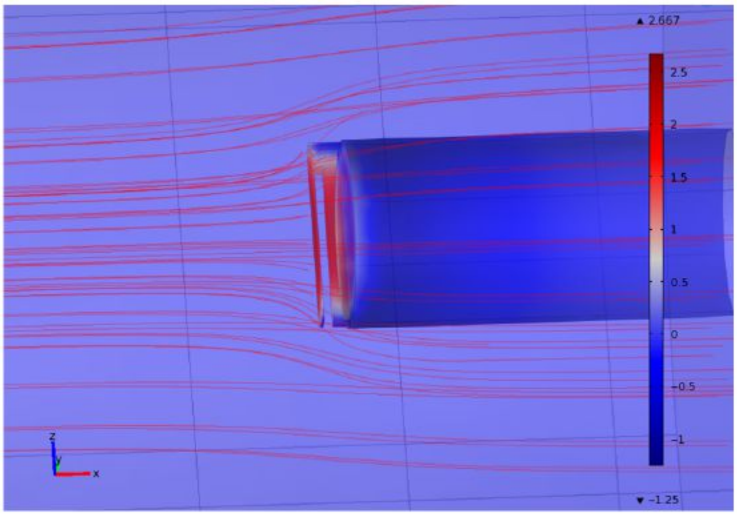

Figure 7.5: Air pressure field and velocity field streamlines computed for an input flow centerline velocity of 2 m/s. The colorbar indicates the pressure in Pa.

bending and therefore limiting the sensitivity of the sensor. In Fig. 7.8 we plot

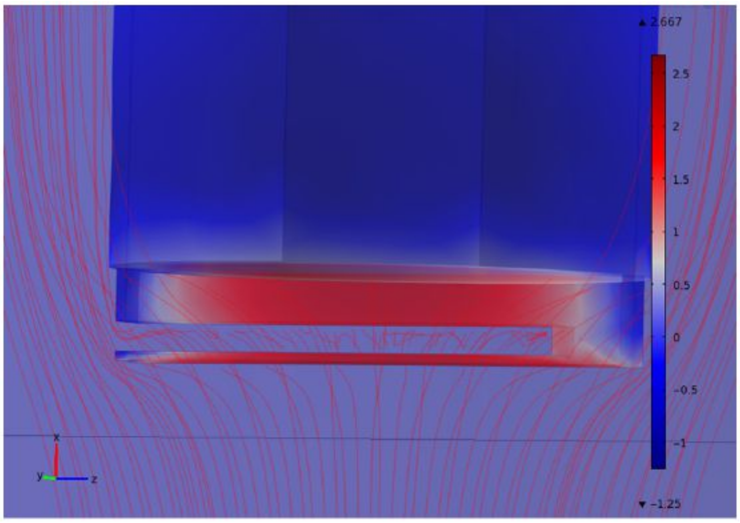

Figure 7.6: Zoomed view of the air pressure field and velocity field streamlines computed for an input flow centerline velocity of 2 m/s. The colorbar indicates the pressure in Pa.

the pressure on the front and the back faces of the cantilever at y = z = 0, as a function of the input centerline flow velocity. As expected from Bernoullis law, both pressures increase quadratically with the input velocity. The cantilever, originally designed for applications far from fluid dynamics (see Refs [51–53]), allows a significant amount of flow to enter laterally the undercut region, also because part of the flow stagnates on the ferrule front face at both sides of the ridge (see Fig. 7.1). The effect could be mitigated by either increasing the ridge length or redesigning the cantilever geometry to minimize the flow penetration. Finally, Fig. 7.9 shows the x-displacement of the cantilever in correspondence of the fiber core, calculated as a function of the centerline flow velocity. The cantilever displacement due to the embedding flow, which is proportional to the fluid pressure in the elastic regime, increases quadratically with the flow velocity. Note that the estimated cantilever displacement at its midpoint is about 30 nm for an input flow velocity of 10 m/s. As discussed in Ref. [134], the interferometric readout allows measurements of cantilever displacements as small as a few Å, corresponding to a theoretical sensitivity in terms of flow velocities in the order of a few cm/s.

7.5 Wind tunnel testing

The numerical model can be compared to the experimental results recently obtained by our group [134]. The experimental set-up used for those measure-

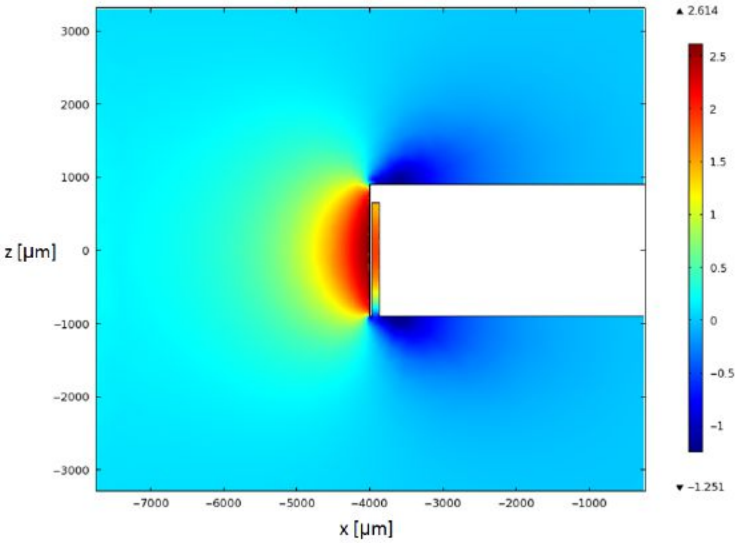

Figure 7.7: Pressure distribution on the $x - z$ plane for $y = 0$ and for an input flow centerline velocity of 2 m/s. The colorbar indicates the pressure in Pa.

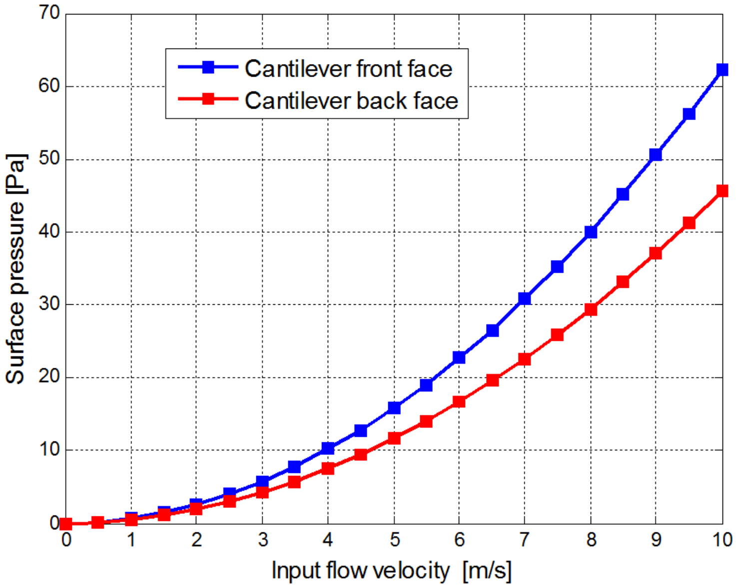

Figure 7.8: Pressure evolution with input flow centerline velocity on the cantilever front and back surfaces in correspondence of the fiber core.

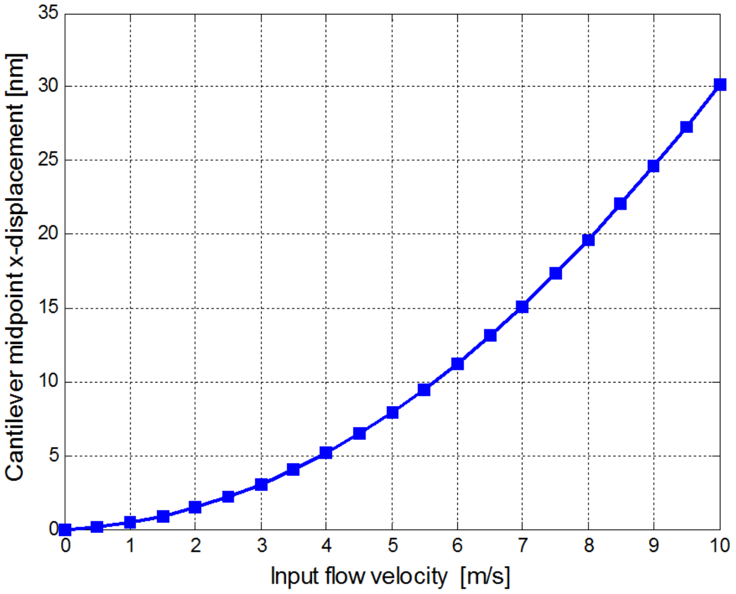

Figure 7.9: Horizontal displacement of the cantilever front face, computed as a function of the input flow centerline velocity.

ments is depicted in Fig. 7.10. A rotational speed controlled fan was placed at the end of a 2 m long wind tunnel to take up the surrounding air through the inlet and create a low-speed flow in a 50×45×50 cm^3 test chamber. The ferrule-top cantilever, after gluing on a glass support, was placed at the center of the test chamber, 5 cm above a standard Pitot tube used as a reference sensor. In this position, it can be safely assumed that the two flowmeters experience the same laminar flow velocity without interfering one each other. The total pressure hole and the static hole of the Pitot were connected to a differential pressure transducer (Sensortecnics HCXPM05D6V). The voltage output of the transducer, which is proportional to the pressure difference, was acquired through a data acquisition (DAQ) card (National Instruments USB-6009). The interferometric readout for the ferrule-top cantilever was based on a 1.544 μm laser diode (LD) and an IR photodetector (PD). The DAQ card was also employed to acquire the interferometric signal from the photodetector.The experimental characterization of the ferrule-top cantilever optical fiber sensor was carried out by setting the flow velocity between 0 m/s and ≈8 m/s (slightly below the maximum flow speed achievable in the wind tunnel). The velocity of the flow was deduced from the Pitot tube by applying the Bernoullis equation:

$$U = \sqrt{\frac{2(p_0 - p_S)}{\rho}} \quad with \quad \rho = \frac{p}{RT} \tag{7.6}$$

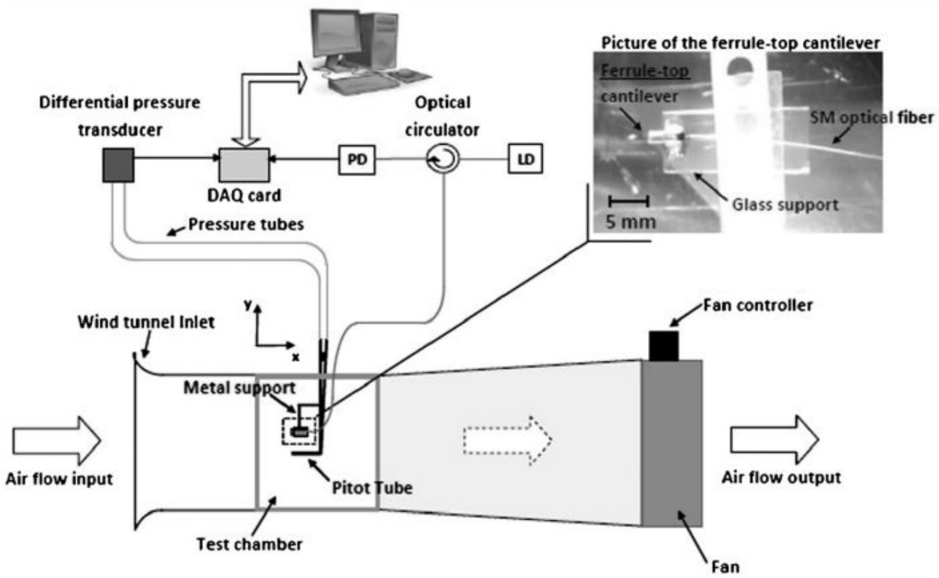

Figure 7.10: Schematic view of the experimental setup for flow velocity measurement using a ferrule-top cantilever.

where U is the flow velocity [m/s], p_0 is the total pressure [Pa], p_S is the static pressure [Pa], ρ is the density of the air [kg/m^3], p is the environmental pressure [Pa], T is the environmental temperature [K] and R is the ideal gas constant (R =287.058 J·kg^{-1}·K^{-1}) for dry air. The environmental conditions were monitored using a barometric station (Sensirion SHT71). The estimation of the error on the flow velocity measured by the Pitot tube was performed by applying the error propagation theory on Eq. 7.6 and considering the standard deviation of repeated measurements for each calibration point as well [138]. The error introduced by the ferrule-top cantilever sensor and its readout is considered negligible. To assess the level of hysteresis and short-term repeatability, the characterization was performed by scanning the flow velocity first from the lowest to the highest values, and then from the highest to the lowest (Fig. 7.11). It is evident that the two calibration curves are in agreement within the error bars, indicating no hysteresis and good short-term repeatability (the experiment was completed within 10 minutes). It is important to stress that the calibration curve is not linear. As a matter of fact, non-linearity arises from two sources: first, cantilever displacement is not linear with the air flow velocity, rather it increases quadratically; second, the intensity of the reflected optical beam is a periodic function of the cavity length (and therefore of the cantilever displacement), according to the response expressed by Eq. 7.1. To put in evidence the two non-linear contributes, we report in Fig. 7.12 the FEM-computed cantilever displacement as a function of the input flow velocity, and the corresponding optical reflectivity of the sensor. The first curve

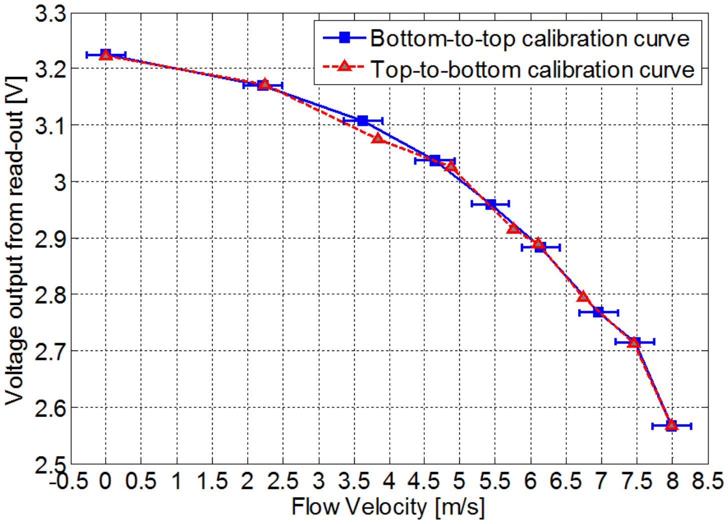

Figure 7.11: Bottom-to-top and top-to-bottom calibration curves for flow velocity measurements.

was obtained by simply inverting the axes of Fig. 7.9, while the second curve was obtained by using Eqs. 7.1 to 7.5. Note that the phase shift ϕ_0 appearing in Eq. 7.1 was chosen in order to provide best fit with the experimental curve. From Eq. 7.1 we note that the half-period of the interferometric response is $\lambda/4$, i.e., in our case, 386 nm. Figure 7.12 shows that the sensor response keeps monotone within the considered velocity range (0 m/s – 10 m/s). Also, in this range the optical response is highly linear (linearity $\approx$ 99.98%). Therefore, we can conclude that the main cause of non-linearity observed in the calibration curve arises from the pressure/velocity quadratic relation. From Eq. 7.1 we see that for large flow velocity ranges a non-monotone response is expected, due to the periodic response of the interferometer. In particular, the flow velocity for which the interferometric response of Fig. 7.12 reaches its first minimum is $\approx$30 m/s, where this value is extrapolated from the quadratic dependence of the cantilever displacement from flow velocity. On the other hand, a larger operating range may be achieved by fabricating ferrule-top sensors with a shorter cavity, at the expense of sensitivity. The two curves plotted in Fig. 7.12 can be combined in order to calculate the overall response of the sensor and compare it to the experimental results. The numerical and experimental outputs are shown in Fig. 7.13. A good agreement can be observed within the considered flow velocity range. The sensitivity of the optical fiber sensor, in terms of minimum detectable flow velocity change, can be roughly estimated by taking the calibration curve slope at the quadrature point of the optical response (corresponding in our case to an input flow velocity of $\approx$15 m/s). In that point, the slope of the curve is $\approx$100 mV/(m/s) in absolute value. Considering that

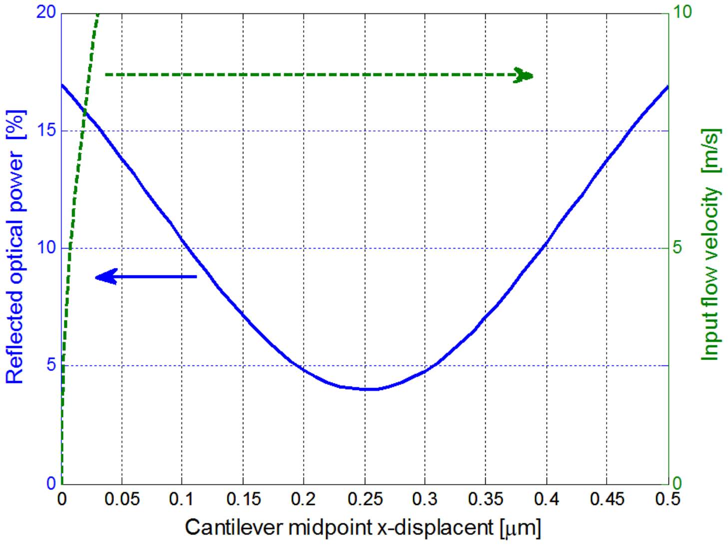

Figure 7.12: Reflected optical power (solid line) and input flow velocity (dashed line) as a function of the cantilever midpoint x-displacement.

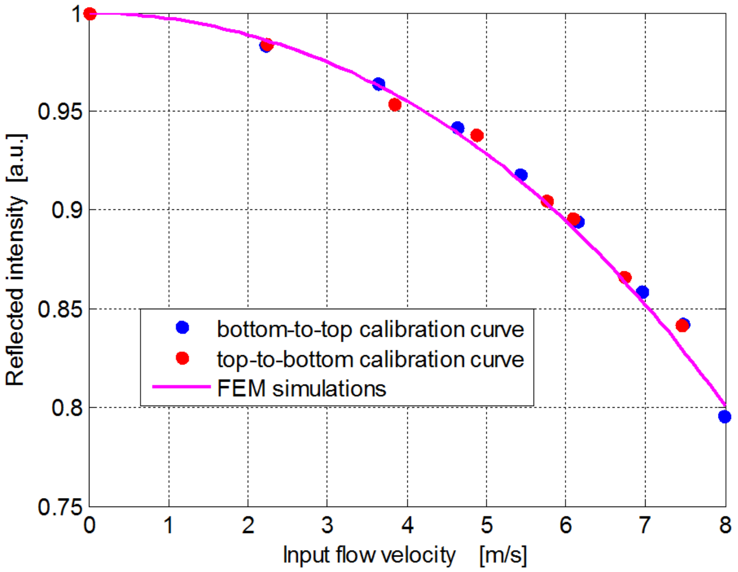

Figure 7.13: Comparison between the response of the flow sensor as calculated by FEM simulations (solid line) and experimental results (circles).

the estimated rms noise of the voltage output over the 100 kHz bandwidth of the readout system was ΔV_{rms}=7 mV, this corresponds to a minimum detectable velocity change of ≈0.07 m/s. Better sensitivities can be achieved after optimization of the readout system and of the geometrical features of the cantilever (e.g. by use of longer or thinner cantilevers). On the down-side, we have observed that ferrule-top devices are affected by non-negligible long-term drifts (10% in roughly 16 hours), which are most likely correlated to humidity and temperature changes in the surroundings [76]. A possible solution may be coating the cantilever with a proper hydrophobic layer, or employing a drift reduction scheme such as the one recently proposed based on cantilever vibration amplitude measurements [139].

7.6 Conclusions

We have performed a FEM analysis of a ferrule-top cantilever immersed in a flow to better understand its behavior when employed for air flow velocity measurements. We have then compared the results of the simulations with a first set of experimental results recently published [134]. Over the entire velocity range investigated during the experiment (0 m/s – 8 m/s), the agreement is satisfactory.

Acknowledgments – The authors acknowledge support from the European COST action TD1001 OFSESA. G. Gruca, K. Heeck and D. Iannuzzi acknowledge support from the European Research Council under the European Communitys Seventh Framework Program (FP7/2007-2013)/ERC grant agreement number 207139.

Chapter 8

Fiber optic sensors for precursory acoustic signals detection in rockfall events

Two fiber optic sensors (FOSs) for detection of precursory acoustic emissions in rockfall events are addressed and experimentally characterized. Both sensors are based on interferometric schemes, with the first one consisting of a fiber coil used as sensing element and the second one exploiting a micro-machined cantilever carved on the top of a ferrule. Preliminary comparisons with standard piezo-electric transducers shows the viability of such FOSs for acoustic emission monitoring in rock masses.

This chapter is based on paper:

L. Schenato, L. Palmieri, G. Gruca, D. Iannuzzi, G. Marcato, A. Pasuto, A. Galtarossa, *J. Europ. Opt. Soc. Rap. Public.* **7**, 12048, (2012)

8.1 Introduction

Collapses of rock masses represent a major source of hazard in mountain areas, being the cause of rapid landslides. Differently from landslides occurring in earth or debris, which are usually surveyed by directed inspection of their surface, rockslides offer few, if any, visible signs. Furthermore rockslides apparently occur all of a sudden [140], making the application of early warning procedures very urgent. Rockslides are associated to processes of stress accumulation in unstable rocks, during which part of the accumulated energy is released in small internal cracks [141]. These cracks generate acoustic emissions (AE) that can, therefore, be used as precursory signals, through which unstable rocks could be monitored. In particular, geological models and experiments have suggested that AE in the range 20-100 kHz (the lower limit being set mainly to greatly limit anthropic noise) are the most indicative to be monitored for that purpose [142, 143].

Unfortunately, the application of traditional AE sensors, such as accelerometers and piezoelectric transducers, finds serious practical limitations due to the faintness of these AEs and the hostility of typical mountain environment (with severe temperature, frequent lightning and ice storms, heavy rains and arduous access). Furthermore, the conventional method consists, basically, in the bare counting of events or of the number of times the AE signal crosses an a-priori defined detection threshold (the so called ring down count): the temporal distribution of such parameters has been considered enough, so far, to the aim of monitoring the rock stability [144, 145].

With this respect, FOSs may fill the gap, providing a reliable solution and potentially offering the following features: more robustness to electromagnetic interference, smaller form factor, multiplexing capability, longer distance range (which lead to easiness of installation), higher sensitivity. To explore this possibility, in this work we analyze two fiber-based optical sensors for AE detection in rock masses. Both sensors are interferometric. The first one uses a 100–m–long fiber coil as the sensing arm of a heterodyne Mach-Zehnder interferometer [146]. The second one is a Fabry-Perot micro-cavity obtained by carving a cantilever on the top of a fiber-bearing ferrule, according to the methodology proposed in [51].

This paper extends the results presented in [147, 148] and is organized as follows: in the Section 8.2, the two sensors are briefly introduced; their experimental characterization is described in Section 8.3 where their performances are compared with a standard piezo-electric transducer (PZT). Finally, conclusions are drawn in Section 8.4: results, while not yet conclusive, confirm that FOSs may represent a viable solution for AEs detection in unstable rock masses monitoring.

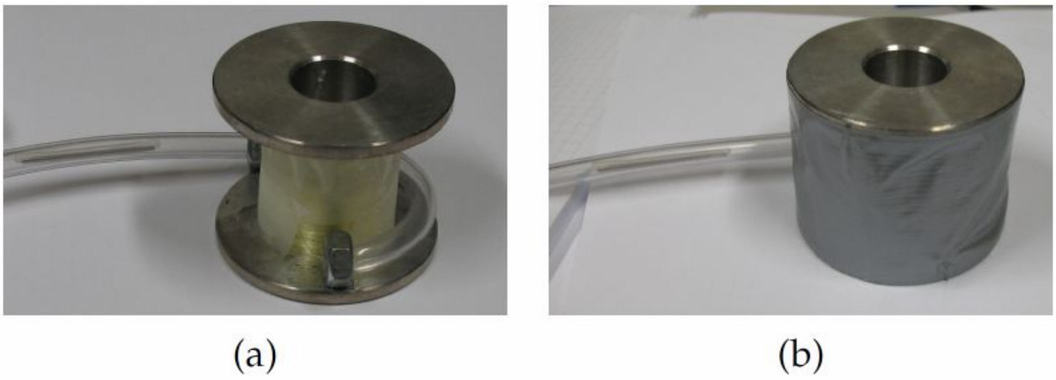

Figure 8.1: The fiber coil sensor: (a) the bare rugged sensor; (b) after it has been acoustically insulated from the environment by means of a layer of acoustic absorbing material and covered by tape.

8.2 The fiber optic sensor

The fiber optic AE sensors addressed here are interferometric devices. The first sensor is shown in Figure 8.1. It consists in approximately 100 m of G.657 optical fiber, tightly wound on an aluminum flanged hollow mandrel (inner diameter 30 mm, height 42 mm). A layer of acoustic absorbing material is applied to insulate the mandrel from the environment. The mandrel can be fastened to the rock by means of a 4–cm–long M10 screw, which acts, also, as the main acoustic coupling element between the rock and the sensor. This

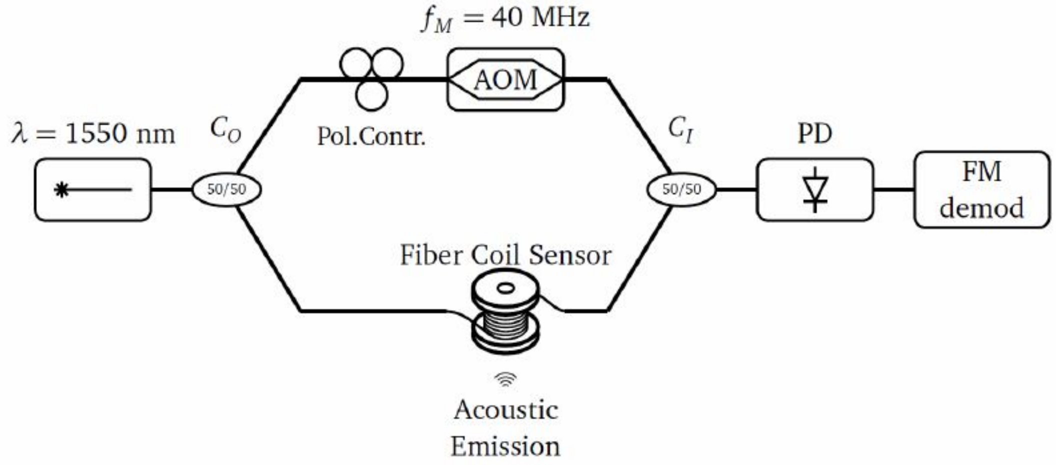

Figure 8.2: Setup of the sensing scheme for FCS: the light source is a high-coherence DFB laser at 1550 nm; AOM: acousto-optic modulator at 40 MHz; C_0 and C_1: optical coupler; PD: photodiode; FM demod: double balanced quadrature FM detector board.

fiber coil sensor (FCS) is inserted in the sensing arm of a heterodyne fiber Mach-Zehnder interferometer, represented in Figure 8.2; the interferometer is interrogated by a high-coherence laser with $l = 1550$ nm. The acousto-optic modulator in the reference arm downshifts the laser frequency by 40 MHz, thus enabling heterodyne detection at the receiver. The use of an heterodyne scheme improves the performance of the setup with respect to the standard homodyne technique: in fact, it allows (i) to reduce the amount of $1/f$ noise, (ii) to avoid the need of an accurate control of laser wavelength (and related thermal drift), and (iii) to relax constraints posed by polarization sensitivity [149]. On the other side, however, it makes the detection more complicated, because a frequency demodulator is needed to retrieve information about AE which is encoded on the phase of the detected signal. The second sensor, shown in Figure 8.3, is made of a micro cantilever carved on the top of a cylindrical silica ferrule [51]. The cantilever lays parallel to the ferrule top along its diameter with only one end attached to the ferrule: in this way the cantilever is free to oscillate under external perturbations. The ferrule houses a standard single mode fiber, and the gap between the cantilever and the fiber end face behaves as a resonating vibration-sensitive Fabry-Perot cavity. The ferrule is about 10 mm long and has a diameter of 2 mm; the cantilever, made of Duran, is about 1.25 mm long, 35 mm thick and 220 mm wide; the gap between the cantilever and the fiber is about 100 mm. In order to increase the

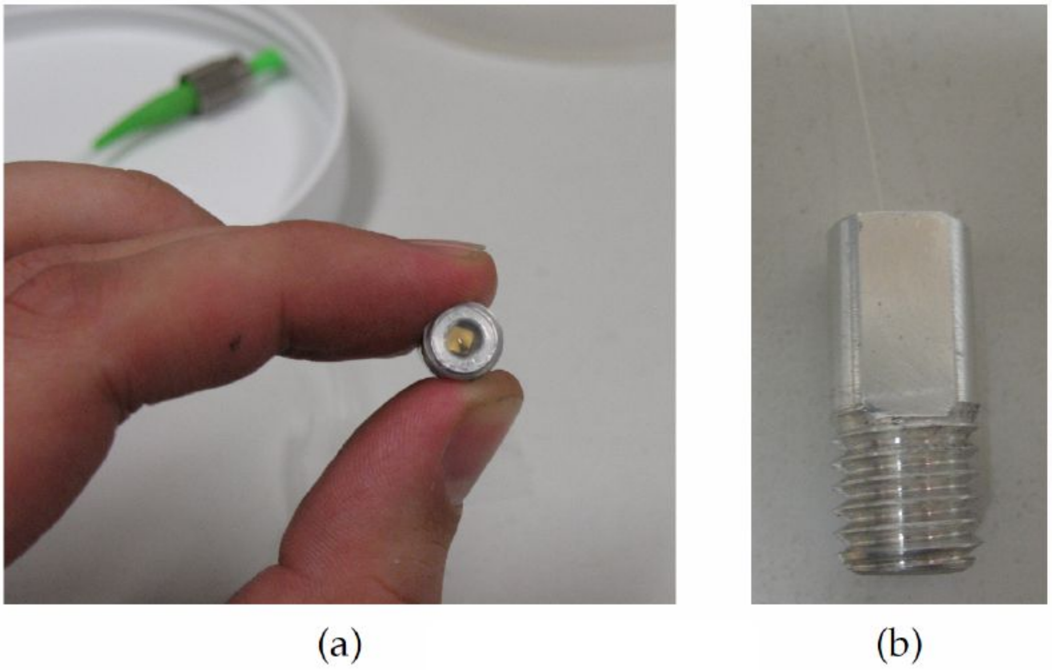
(a) (b)

Figure 8.3: The ferrule top cantilever sensor: (a) front view; (b) side view.

reflectivity of the cavity, the upper face of the cantilever is coated by a thin layer of gold. These parameters, along with the Young modulus and density of Duran, allow to calculate the first nominal mechanical resonance by means of the Euler-Bernoulli equation [150]; accordingly:

$$\upsilon = \frac{\kappa^2}{2\pi}\sqrt{\frac{E}{\rho}\frac{wt^2}{12}\frac{1}{wtL^4}} \sim 19.4\ kHz \tag{8.1}$$

where $\kappa = 1.875$, $E = 64$ Gpa and r=2.23 g/cm^3 are, respectively, Young Modulus and density of Duran and w, t and L are the width, thickness and length of the cantilever, respectively. The measured mechanical resonance is 12.5 kHz and differs significantly from the calculated one: this is actually a common problem that afflicts also commercial atomic–force–microscope probe where resonance frequency is typically within 50% from its nominal value. Ultimately, this can be imputed to several reasons: a not perfect rectangular shape, a not uniform thickness of the cantilever, presence of the thin gold layer that coats the upper cantilever face, presence of glue which fills in the bore hole on the cantilever. Finally, the Q-factor of the cantilever has been roughly estimated in 400, by measuring experimentally the relaxation time of the damped harmonic oscillation signal from the sensor [151]. A 20–mm–long M10 bored bolt housed this ferrule top cantilever sensor (FTC), while providing both protection and a suitable mean of mechanical and acoustic coupling to the rock. The reflectivity of the FP cavity, which is probed by a lowcoherence laser tuned at the quadrature point of the cavity, changes accordingly to the AEs induced vibrations, and that information is decoded with the setup shown in Figure 8.4.

8.3 Experiments

Acoustic coupling and impedance matching play a crucial role in the performance of AE sensors [152]; therefore, in order to get realistic testing conditions, we have tested the sensors on a block of Montemerlo Classic Gray Trachyte (50 × 50 × 15 cm in size, about 100 kg in weight). The FOSs were screwed in an internally threaded anchor, chemically glued in a hole at the center of one of the blocks 50 × 50 cm faces. For convenience, the block was simply supported at 4 points near the corners of the drilled face; in that way, the sensor under test was screwed in the bottom face of the block, with the top face left clear for the excitation of AEs in different positions. During the tests, an amplified PZT (VS30-SIC-46dB from Vallen Systeme GmbH, 46 dB of electrical amplification) have been used to compare its performances with those of the FOSs. Electrical signals from PZT, FTC photodiode and FCS demodulation board are eventually recorded by a digital storage oscilloscope.

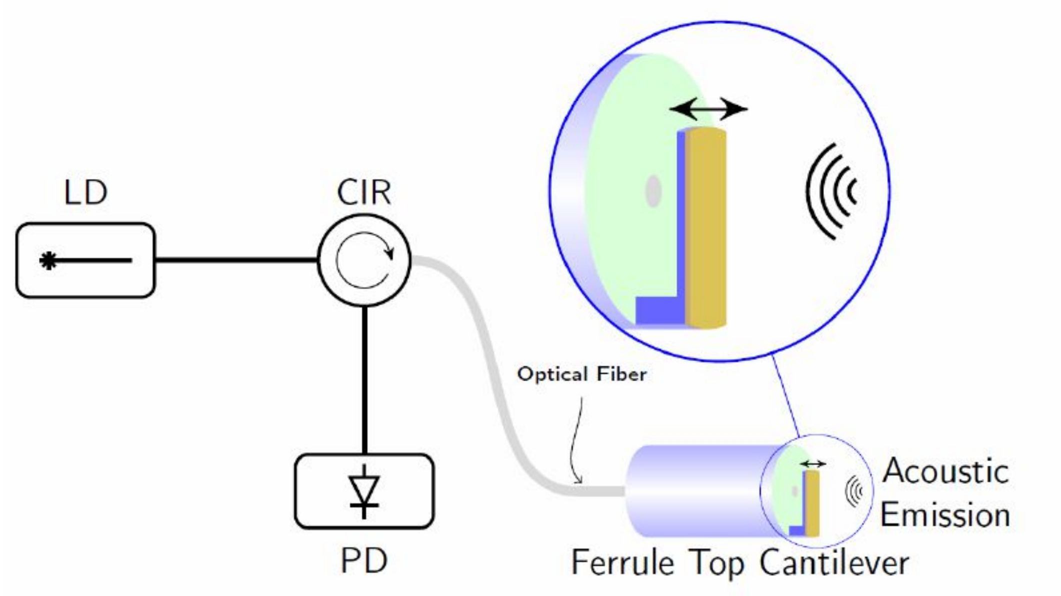

Figure 8.4: Setup of the sensing scheme for FTC: the light source is a low-coherence laser (LD: laser diode) at the quadrature wavelength of the cavity; CIR: optical circulator; PD: photodiode.

Acoustic emissions have been generated in a repeatable way by the impact of a 5–mm–diameter steel ball dropped along a steep slide, placed on the top of the block [153]. Repeatability of this method of excitation has been tested extensively and it is within 10%; moreover, it has been found that direction of impact of the ball has a negligible effect on the recorded signal. Upper part of Figure 8.5 shows, for each of the three sensors (the two FOSs and the PZT), a sample signal recorded when the ball is dropped at the center of the upper face of the trachyte block. Right below in Figure 8.5, the corresponding power spectral densities (PSD) are represented. It can be noted that, amongst the three sensors, the PZT has the most flat spectral response. As expected, the spectral response of the FTC is dominated by a peak centered at 12.5 kHz, the resonance frequency of the cantilever. Correspondingly, the time evolution of the signal recorded by the FTC is basically a damped oscillation. On the contrary, the signals recorded by the FCS and the PZT are close to the actual AE. Even though the FTC can provide very little information about the spectral content of the AE, this is not at all a limitation, since as noted in the introduction section the bare detection and counting of AE events, enabled by the FTC, is the standard methodology for the present geological application. Rather, the prolonged temporal damping of the signal from FTC, contributes in enhancing the sensitivity, although this comes at the expense of a reduced capability of resolving in time two consecutive AEs. To compare the three sensors, several tests have been performed by dropping the ball at different positions on an

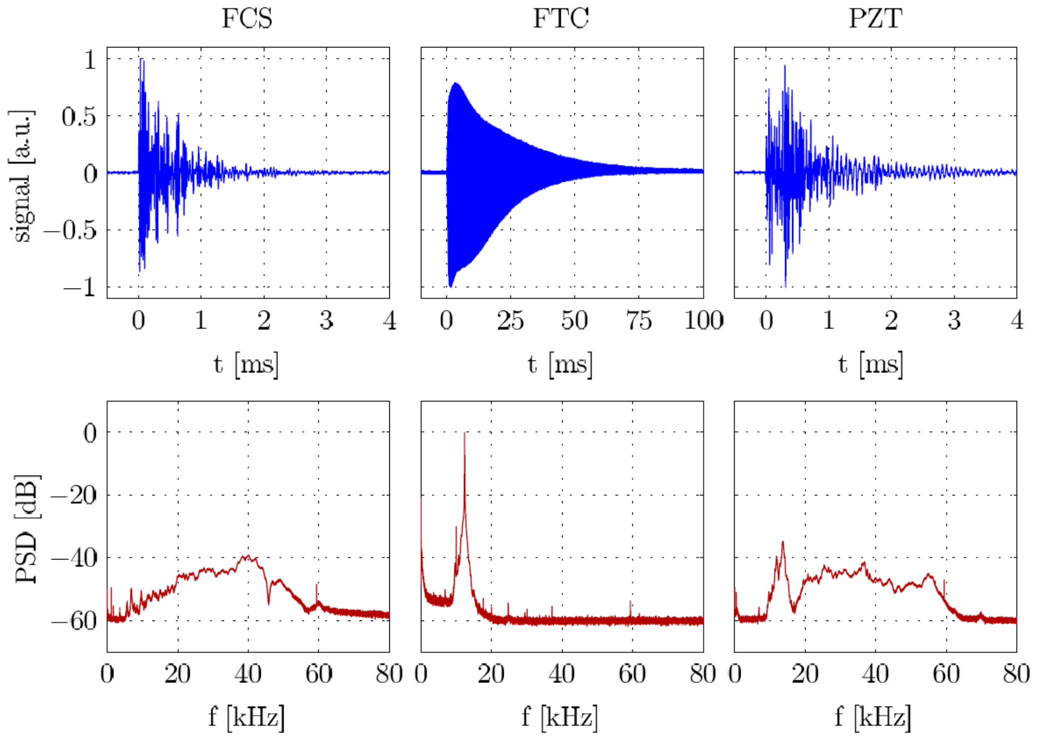

Figure 8.5: Typical signals (top row) and corresponding PSDs (bottom row) recorded by the three sensors (FCS, fiber coil sensor; FTC, ferrule-top cantilever; PZT, piezoelectric transducer).

uniform 7 × 7 grid, drawn on the top 50 × 50 cm face of the block, as in Figure 8.6. For each dropping, a signal, $y(t)$, has been recorded and the acoustic energy over an arbitrary window T defined as $Y(t) = \int_t^{t+T} y^2(\tau)d\tau$ has been calculated. The window length T has been chosen as the average length of the event, as recorded by the specific sensor. Actually, using a window longer than the event would be pointless, because it would just includes more noise in the integral. Therefore, we have set $T = 5$ ms for FCS and PZT, whereas for the FTC, owing to its damping behavior, we have set $T = 100$ ms. As stated above, this longer integration window results in a improved sensitivity but in a more realistic scenario where a sequence of AEs may occur, increasing T reduces temporal resolution, as well. Then we have defined the recorded intensity of the AE as $\max_t\{Y(t)\}$.

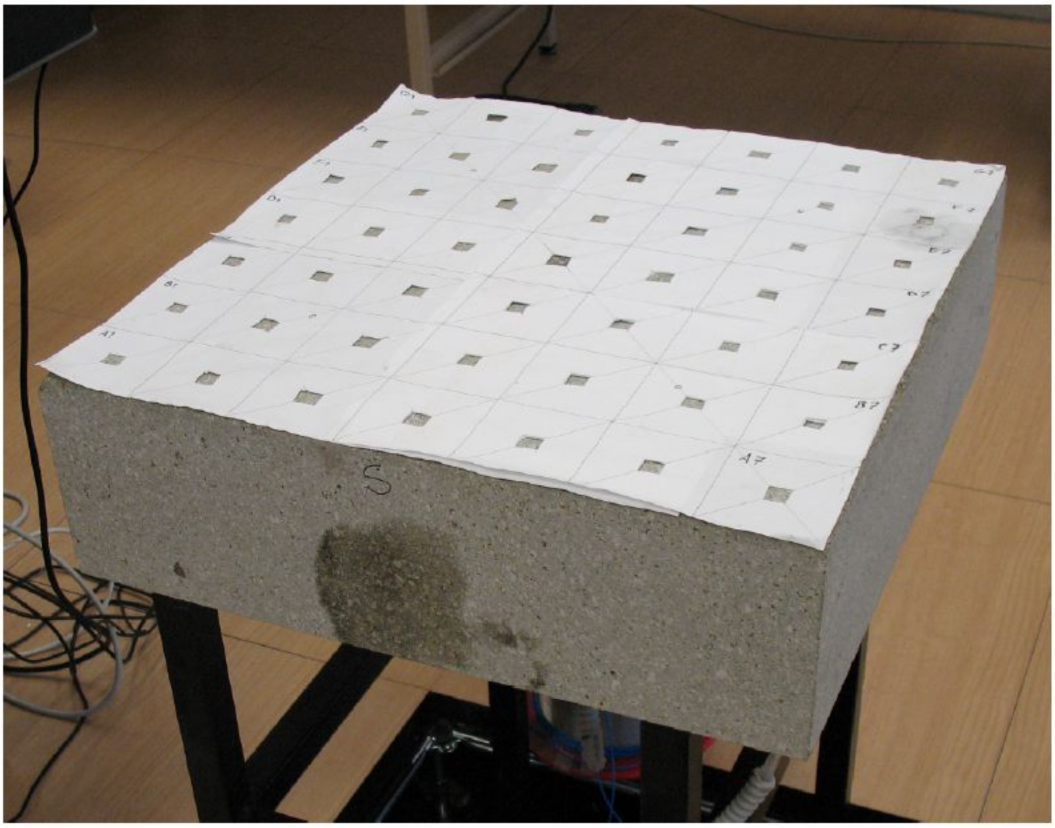

Figure 8.6: Upper face of the trachyte block with the uniform grid according to which the ball has been dropped to test the responsivity of the sensors.

The results of these tests have been plotted in the three uppermost graphs of Figure 8.7, where we have represented the intensities detected by each sensor with respect to the different dropping positions on the grid. To compare results, intensities have been normalized for each sensor independently, with respect to their maximum on the grid: as expected, the sensors mostly show higher intensities when the ball is dropped closer to the center, where sensors were screwed. Nevertheless, this correspondence is not perfect, likely because of inhomogeneities in the rock block. Moreover, it can be noticed that the more marked dependency on the excitation position is exhibited by the FTC, followed by the FCS, and then, by the PZT. We impute these differences mainly to a different sensitivity of sensors to surface waves, induced by the impact. Actually, while the PZT is coupled to the rock only by means of its flat surface, the FTC is totally inserted inside the rock and therefore it is more sensitive to volume waves. On the other side, the FCS is acoustically coupled both through the screw, and through one of the mandrel flanges that in in contact with the flat block surface. To support this argumentation, the test has been repeated by installing the PZT on a pedestal, made of a long flat-head bolt directly screwed into the block, as it happens to the FOSs. In this way, we are confident to reduce the surface coupling, and hence we expected the PZT to become more sensitive to volume waves. Results, reported in the lowermost graph of Figure 8.7, show a marked increase of the dependency on the excitation position, in agreement with our hypothesis.We remark that the intrinsic insensitivity to surface waves is a desirable feature, because noise sources (e.g. anthropic activities and meteors) acting outside real rock masses are most likely to induce surface waves, rather than volume ones. About absolute performances, the FCS is the least sensitive of the three sensors: with respect to FCS, the peak intensities of FTC and PZT are about 30 dB and 50 dB higher, respectively. Notice, however, that both FTC and PZT include at the receiver an electrical amplification of 20 dB and 46 dB, respectively; differently, electrical amplification is not exploited in the FCS. Taking that gain amplification into account, the most sensitive sensor is the FTC, although we recall that this performance comes at the expense of a twenty-fold reduction of temporal resolution. Noise performances are comparable, since the three sensors have an SNR of about 30 dB. Analogous results have been obtained by changing the position at which sensors were screwed at the bottom face of the trachyte block.

8.4 Conclusions

In this paper some preliminary experimental analyses aimed at exploring the applicability of FOSs to the monitoring of unstable rock masses have been reported. Two different interferometric sensors have been considered and compared with a standard PZT: the first sensor is based on a fiber coil, FCS, while the second one is based on a ferrule top cantilever, FTC The PZT outperforms both FOSs in term of sensitivity, yet it should be remarked that this is mainly due to its internal 46 dB electrical amplification. By taking into account the

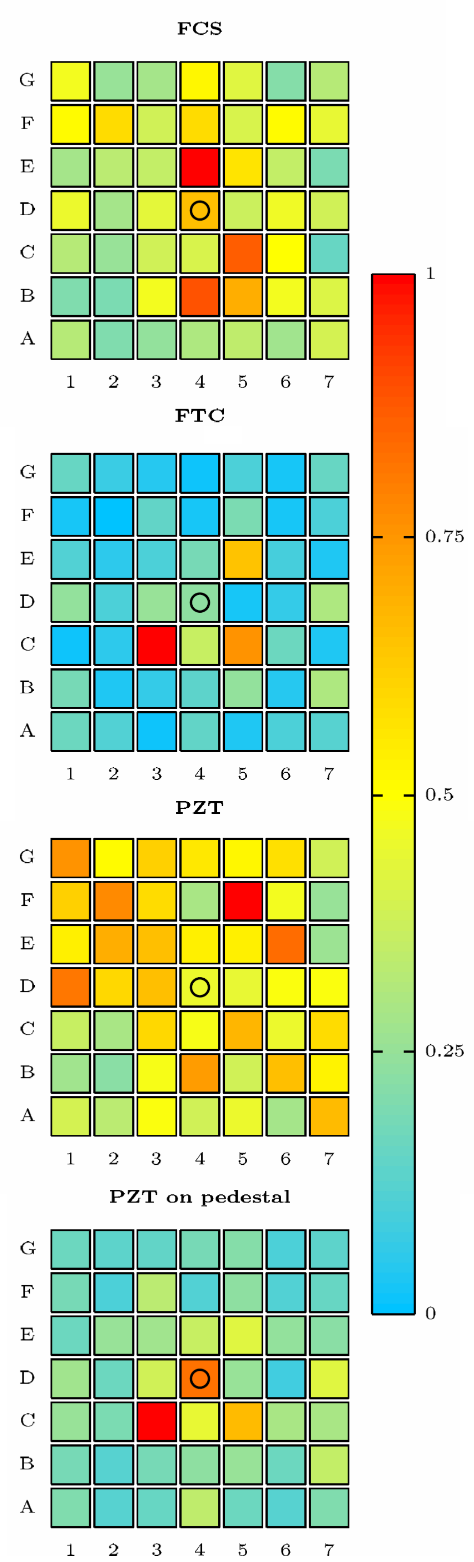

Figure 8.7: Normalized intensities recorded by the sensors as a function of the position of impact (FCS, fiber coil sensor; FTC, ferrule-top cantilever; PZT, piezoelectric transducer; empty circles indicate sensor position).

differences in electrical amplification, the FTC is the most sensitive sensor, although FTC is also the one with the least temporal resolution. Experimental results suggest also that FOSs (FTC, in particular) could be intrinsically more sensitive to volumes waves, whereas PZT appears to be more sensitive to surface waves. To the aim of rock mass monitoring, this characteristic of the FOSs is highly desirable, because surface waves are more easily triggered by environmental noise. While further developments and investigations are needed, this preliminary analysis has shown that FOSs represent a viable approach to the monitoring of unstable rock masses.

SENSORS

Rock-fall warning

J. Eur. Opt. Soc. Rapid Publ. **7,** 12048 (2012)

Rock falls are a major hazard in mountainous areas. Fortunately, it is possible to predict collapses by monitoring acoustic emissions from internal cracks in rocks. Luca Schenato and co-workers from the National Research Council of Italy, Vrije Universiteit Amsterdam in the Netherlands, and the University of Padova in Italy have now proposed a fibre-optic sensor for use in such an application. The device consists of a microcantilever on top of a cylindrical silica ferrule. The ferrule houses a standard single-mode fibre, and the gap between the cantilever and the fibre end face behaves as a resonating vibration-sensitive Fabry–Pérot cavity. The researchers measured the effect of dropping a steel ball on a trachyte block by monitoring the temporal change in the signal and its power spectral density. The spectral response was dominated by a peak centred at 12.5 kHz, which was the resonance frequency of the cantilever. The signal decayed asymptotically to a background level after about 100 ms. The ferrule top cantilever sensor was sensitive to volume waves because it was completely inserted in the rock. *NH*

Figure 8.8: The outcome of the experiment described in this chapter has been noticed in research highlights of Nature Photonics (N. Horiuchi. Sensors: Rock-fall warning. Nat Photon, **7(3)**:167167, 2013).

Acknowledgments – The research was supported by Fondazione Cassa di Risparmio di Padova e Rovigo under the project SMILAND, by the European Research Council under the European Communitys Seventh Framework Programme (FP7/2007-2013)/ERC grant agreement 201739, by the European COST Action TD1001 OFSeSa, and by the Stichting voor Fundamenteel Onderzoek der Materie (FOM) under the Valorization grant number 11VAL11C. Logistic support by Lucio Baseggio is acknowledged.

Chapter 9

Demonstration of a miniature all-optical photoacoustic spectrometer based on ferrule-top technology

We present a new miniaturized photoacoustic (PA) spectrometer obtained by carving a micromachined flexural pressure transducer directly at the top of a glass ferrule. The ferrule is equipped with two optical fibers, one for laser excitation of the gas and one for interferometric readout of the transducer. To demonstrate the working principle and assess the sensitivity of the device, we performed a set of measurements of C_2H_2 traces in an Ar buffer atmosphere. The data acquired show that our ferrule-top scheme allows one to reduce the minimum detectable concentration by more than one order of magnitude with respect to the other miniaturized PA spectrometers reported in the literature, while decreasing the integration time of a factor of 10.

This chapter is based on paper:

G. Gruca,K. Heeck, J. H. Rector and D. Iannuzzi, *Optics Letters* **38**, 10, pp. 16721674, (2013)

9.1 Introduction

The photoacoustic (PA) effect was discovered more than 130 years ago [154]. However, because of the lack of proper light sources and high resolution pressure transducers, it remained for long ignored in any practical application. In the mid 70's [155–158], scientists started to recognize that, exploiting the tremendous progress in laser technology and electromechanical sensing techniques, it was finally possible to develop extremely sensitive, highly selective PA gas spectrometers. PA spectroscopy (PAS) is nowadays recognized as an analysis technique with potential applications in microbiology, physiology and health diagnostics [159, 160]. Unfortunately, to reach ultimate performance, it

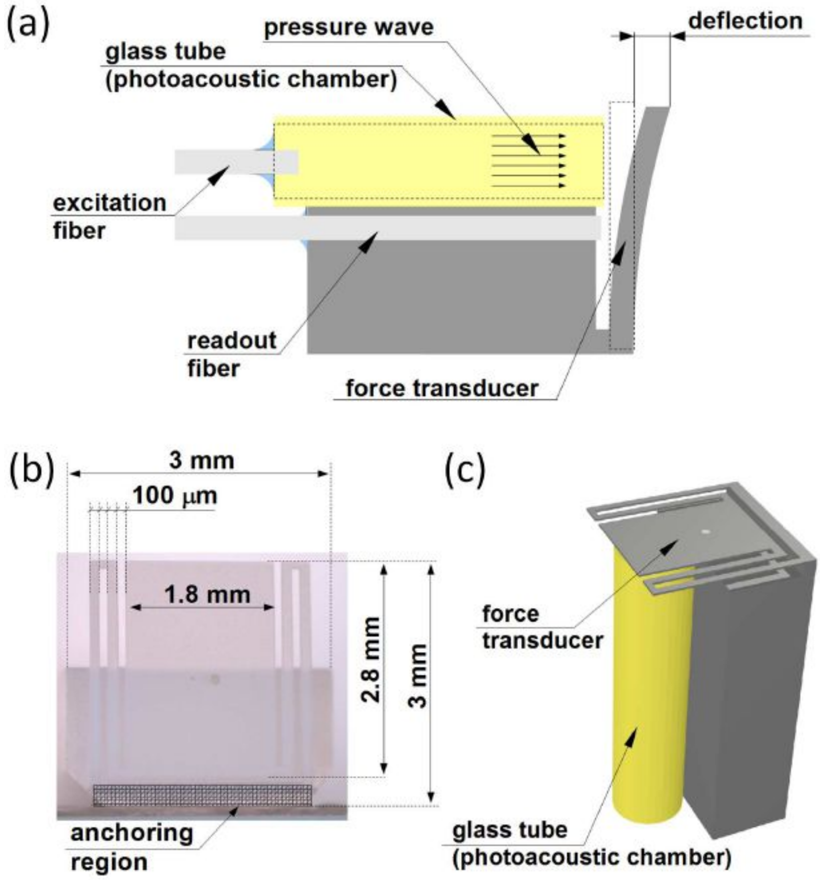

Figure 9.1: (a) Schematic view of a ferrule-top photoacoustic spectrometer. The ferrule is initially machined with a precise diamond wire saw to fabricate a thin flap at the top. Next, the flap is carved, by means of picosecond laser ablation, to define the flexural springs. Finally, a glass tube is mounted underneath the transducer and two fibers are glued to shine light into the tube (excitation fiber) and to look at the displacement of the transducer (readout fiber), respectively. (b) Optical microscope image of the transducer after the laser ablation process (top view). (c) 3D sketch of the ferrule-top photoacoustic spectrometer.

is often necessary to rely on sophisticated measurement schemes and elaborated setups. For example, one of the most sensitive PA spectrometers ever reported in the literature is based on a microcantilever based microphone equipped with a bulk optical interferometric readout [161], which requires a careful alignment procedure to operate correctly. On the other hand, for some applications, performance is not essential. Other factors, such as immunity to electromagnetic noise or ability to perform measurements from a remote position, may play an equally important role. It is thus not surprising that a significant part of the literature has focused on fiber based PAS. Integrating optical fibers directly into a standard photoacoustic cell [162], or replacing electronic microphones with their optical equivalents [163], one can assemble PA spectrometers that have no electronics in the sensing volume while keeping a low detection threshold. All these solutions still rely on quite large pieces of equipment, which do not adapt well to utilization in small volumes or in the presence of small apertures. In a very recent paper, *Y. Cao* and colleagues introduced a new setup based on the idea to put the entire PA cell on the tip of an optical fiber, which is simultaneously used to remotely interrogate the microphone mounted in the cell and excite the gas molecules [164]. The latter is as small as a few cubic millimeters. This new setup is thus both compact and adapted for remote sensing. Here we present a new scheme where we rather attach a very small cell to a micromachined force transducer. This scheme allows us to gain more than one order of magnitude with respect to the previous work while reducing the integration time to 1 s.

9.2 Working principle

Our PA spectrometer is based on ferrule-top technology [12]. The micromachined force transducer consists of a 2800 μm long, 1800 μm wide, 30 μm thick plate suspended, via a series of cantilever springs, directly over the end of a 1.6 mm × 3 mm × 7 mm borosilicate glass ferrule (see Fig. 9.1). The ferrule is equipped with a bore hole designed to host a single mode optical fiber (*readout fiber*) that looks at the flat plate of the transducer. The gas in the surroundings of the transducer (i.e., the gas that has to be analyzed) diffuses into a small tube (inner diameter = 600 μm, outer diameter = 1 mm) that is glued onto the carved side of the ferrule, just underneath the hanging end of the suspended plate (distance between the capillary end and the force transducer $\approx$100 μm). Any change of pressure inside the tube pushes the gas out, producing a force pulse that can be detected by looking, from the distal end of the optical fiber, at the Fabry-Perot signal generated between the fiber end and the flat plate. The PA excitation light is brought inside the tube via another single mode optical fiber (*excitation fiber*), which is slid into the tube from the opposite aperture and glued during probe fabrication (distance

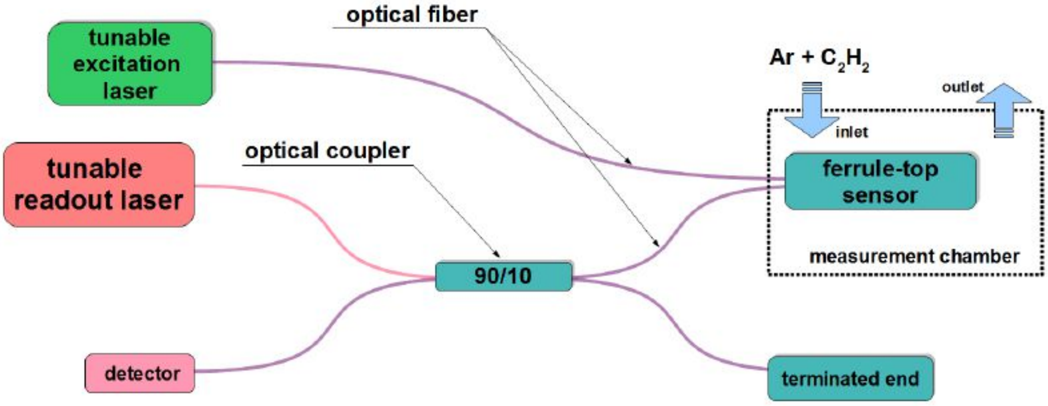

Figure 9.2: Schematic view of the readout and excitation setup. The bending of the transducer is measured from the interference signal coming back from the Fabry-Perot cavity created between the fiber end and the transducer. To achieve high sensitivity, the laser wavelength can be tuned to match the quadrature condition. Another laser, connected to the excitation fiber, is used to excite the gas molecules.

between the end of the fiber and the open end of the tube ≈2 mm). For the details of the design and fabrication process we refer the reader to the caption of Fig. 9.1 and to reference [12].

9.3 Performance evaluation

To evaluate the performance of our PA spectrometer, we mounted the probe inside a small chamber (50 ml) that was continuously flushed with a mixture of argon and acetylene at room temperature and atmospheric pressure. The total flow rate was set to 0.5 l/min. The amount of acetylene was controlled by injecting, via a calibrated mass flow controller (MKS Mass-Flo) the correct proportion of C_2H_2 in the main stream of argon. The displacement of the suspended plate was monitored with a commercial interferometer (OP1550, Optics11), whose working principle is sketched in Fig. 9.2. The interferometer is equipped with a 20 mW laser that can be tuned over 30 nm. The tuning range is sufficient to determine, after previous wavelength scan, a full spectrum of the Fabry-Perot cavity. To guarantee maximum linearity and optimal sensitivity, the wavelength was adjusted to match quadrature conditions. For the transducer used in this experiment, the visibility of the fringes of interference was measured to be equal to 95%, which allowed us to reach a displacement resolution of 0.15 nm over a 20 kHz bandwidth. To excite the PA signal, we coupled the excitation fiber to a 23 mW C-band semiconductor laser tuned around the P(9) absorption line and modulated in wavelength by injecting additional current to the driving circuit, as explained in [164]. The additional current was set to a level sufficient to reach a symmetric triangular wavelength

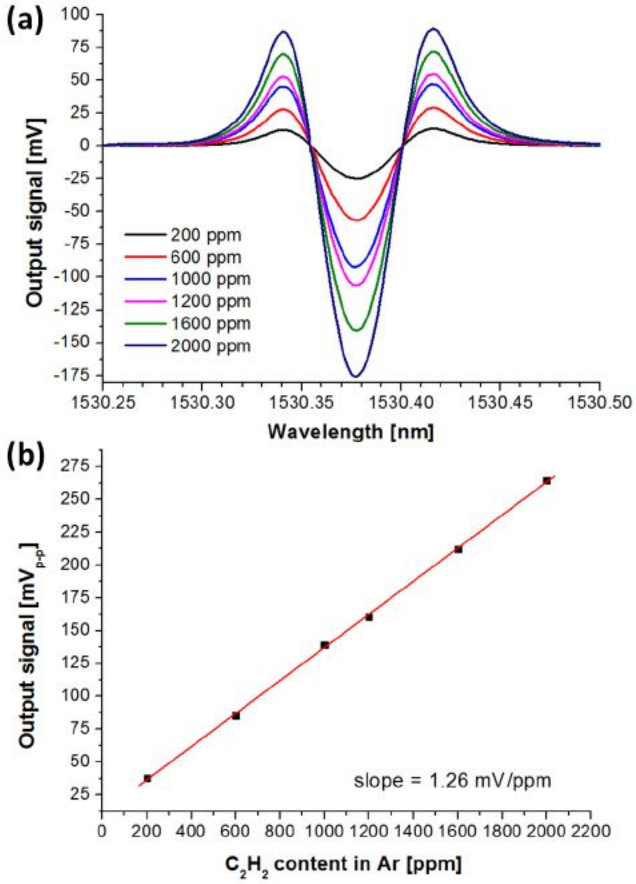

Figure 9.3: (Color online) (a) Photoacoustic signal measured for different concentration of C_2H_2 in Ar. (b) Linear fit of the data points extracted from (a). The data presented in this figure were collected with a lock-in amplifier time constant of 300 ms. From this graph, it is clear that our spectrometer has a linear response within the range investigated.

modulation (WM) of 150 pm. Although the mechanical quality factor of the transducer was not particularly high ($Q = 32$ at atmospheric pressure and room temperature), to increase the signal level, we set the modulation frequency of the excitation laser to 457 Hz, a half of the mechanical resonance of the transducer. The output of the readout was then sent to a lock-in amplifier locked to the second harmonic of the modulation frequency. In Fig. 9.3(a) we show the in-phase oscillation amplitude of the transducer as recorded at the exit of the lock-in amplifier, plotted as a function of the central wavelength of the modulated laser. The different lines correspond to the different concentrations of C_2H_2 present in the chamber, and were obtained setting the time constant of the lock-in amplifier to 300 ms. The graphs resemble those already reported in literature for WM-PA [165]. Fig. 9.3(b) shows the peak-to-valley values as a function of C_2H_2 concentration. It is evident that our PA spec-

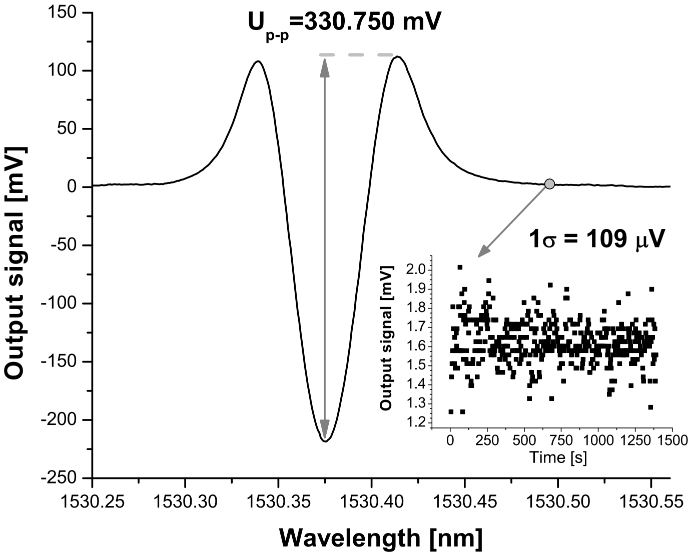

Figure 9.4: Photoacoustic signal obtained when the measurement chamber was filled with a gas mixture containing 0.1% of C_2H_2 in Ar. In the inset: output signal of the lock-in amplifier acquired outside the absorption range of C_2H_2 over a prolonged time interval.

trometer offers a linear response over the range of concentrations explored. It is to note that, throughout the whole measurement period, we never changed the excitation frequency. It is thus clear that, in our experiment, the drift of the resonance frequency of the transducer was negligible. To estimate the minimum detectable concentration (MDC) of our spectrometer, following the approach used in reference [164], we divided the peak-to-peak amplitude of the signal by the standard deviation (1σ) measured in a region where no absorption was noticed. With this method, we obtained an MDC equal to 551 ppb. Increasing the time constant to 1 s, and improving the gain of the photodetector, we could further reduce the MDC to 330 ppb (Fig. 9.4), which is more than one order of magnitude better than the value of 4.3 ppm reported in [164], even though our integration time was 10 times smaller. However, we would like to point out that this method is rigorously correct only to compare the performance of different sensors and cannot be taken as representative for general working conditions, where external acoustic noise and flow variations can effectively deteriorate the MDC to $\approx$1.5 ppm (see Fig. 9.5)

Acknowledgments – We are indebted with *L. de Maria*, who has encouraged our group to enter this field and has contributed with enlightening discussions.

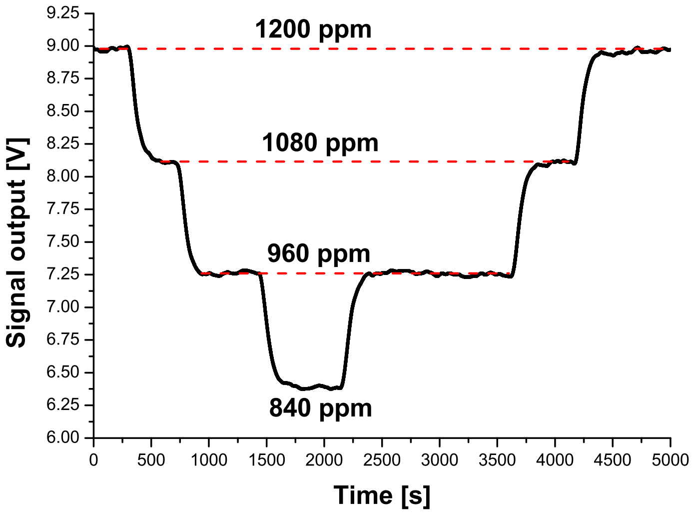

Figure 9.5: Photoacoustic signal measured at the output of the lock-in amplifier in non-ideal (noisy) laboratory conditions. The excitation laser was tuned to the maximum of the P(9) absorption line and the lock-in integration time was set to 300 ms. The variation of the signal at the flat parts of the figure mainly comes from acoustic noise coupled into the chamber and from small flow variations in the vicinity of the sensor.

We also acknowledge the support of the COST Action TD1001 OFSESA, which has allowed us to discuss our ideas with a large number of colleagues. We finally acknowledge support from the ERC (StG (FP7/2007-2013) grant agreement number 201739) and the Dutch Foundation for Fundamental Research on Matter (FOM - Valorization grant).

Chapter 10

Top-down approach to fiber-top cantilevers

Taking inspiration from conventional top-down micromachining techniques, we have fabricated a low mass gold fiber-top cantilever via align-and-shine photolithography. The cantilever is characterized by measuring its resonance frequency and mechanical quality factor. Our results show that the device grants mass sensitivity comparable to that reported for similar standard cantilevers. This proof-of-concept paves the way to series production of highly sensitive fiber-top devices for remote detection of biochemical substances.

This chapter is based on paper:

K. B. Gavan, J. H. Rector, K. Heeck, D. Chavan, G. Gruca, T. H. Oosterkamp and D. Iannuzzi, *Optics Letters* **36(15)**, 2898-2900, (2011)

10.1 Introduction

Over the last decade, several groups have demonstrated that an array of miniaturized cantilevers, individually coated with suitable chosen layers, can provide a unique platform for ultrasensitive detection of biochemical species [166–169], with potential applications in, among others, early cancer diagnosis [21]. Those instruments rely on the fact that, in the presence of one of the substances that have to be detected, it is possible to observe a static deflection or a resonance frequency shift of one of the cantilevers, whose positions are continuously monitored by means of optical triangulation [170] or electronic readouts [171, 172]. Unfortunately, optical triangulation techniques are unsuitable for utilization in small volumes or remote sensing. Furthermore, they require severe technical efforts to be inserted in a user-friendly automated system. Electronic readouts, on the other hand, are generally less sensitive, less stable, and they are prone to failure when used in liquids, electromagnetic noisy environments, explosive gases, or extreme temperatures. To alleviate the readout problem, it has been proposed to fit each cantilever on the cleaved end of an optical fiber tip [7, 11, 173]. Light coupled from the opposite end of the fiber can then be used to measure the displacement of the cantilever remotely. This solution, however, relies on unconventional fabrication processes that make those devices too expensive for any practical application. Still, it is evident that the implementation of a more convenient approach for the fabrication of cantilevers on optical fibers would open up unprecedented opportunities in the field of mechanical detection of biochemical substances.

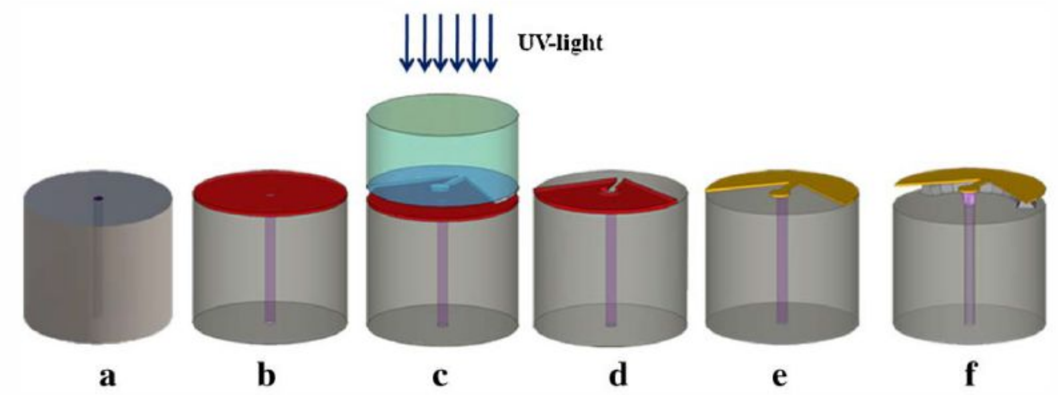

Figure 10.1: Schematic view of the steps followed for top-down fabrication of fiber-top cantilevers (not to scale). (a) A cleaved optical fiber, (b) coating of the optical fiber with photoresist, (c) pattern transfer via align-and-shine photolithography [14], (d) resist development, (e) deposition of a chromium-gold bilayer and lift off of the photoresist, (f) wet etch release of the cantilever.

10.2 Fabrication and readout

In this Letter, we introduce a method that, taking inspiration from conventional top-down micromachining, allows growing, patterning, and mechanical suspension of a fiber-top cantilever via a series of steps that adapt well to batch production. Top-down machining is widely recognized as the most cost effective approach in the fabrication of microelectromechanical systems. The approach is based on the possibility to grow and pattern alternate layers of structural and sacrificial materials on a flat substrate. Dissolving the sacrificial layers with a wet etching process, one can then obtain suspended three-dimensional mechanical parts that are free to move in response to an external event [15]. To demonstrate that a similar top-down approach can be used for the fabrication of fiber-top cantilevers, we have followed the steps illustrated in Fig. 10.1. The cleaved end of a single-mode silicon dioxide optical fiber (Fig. 10.1(a)) is dipped in positive tone photoresist. The thin, flat photoresist layer that remains attached at the end of the dipping step is then hardened

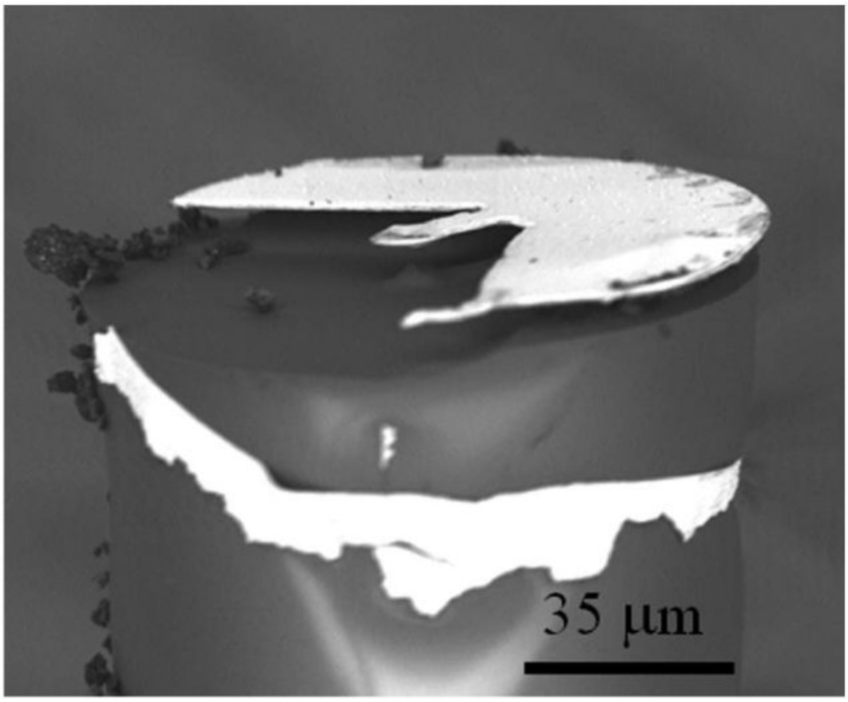

Figure 10.2: Scanning electron micrograph of a fiber-top cantilever fabricated with a top-down approach. The dimensions are: thickness = 350 nm, overall length cantilever paddle 22 μm, width = 7 μm, and diameter of the paddle = 11 μm.

by keeping the fiber at 105^{o}C for 10 minutes (Fig. 10.1(b)) and exposed to UV light through a patterned mask fiber via align–and–shine photolithography [14] (Figs. 10.1(c) and 10.1(d)). After removal of the exposed photoresist areas (resist development), the fiber is mounted vertically on a deposition system, where it is coated with a thin chromium-gold bilayer. The remaining photoresist film and the metal deposited on its top are then rinsed away with methanol (lift off) (Fig. 10.1(e)), leaving behind a chromium-gold pattern that has the shape of a paddled cantilever. Finally, the fiber end is immersed for 50 minutes in buffered oxide etch to isotropically remove a few micrometers of silicon dioxide from all the areas that are not protected by the chromium-gold bilayer. This last step frees the cantilever, which remains anchored to the fiber by means of a metallic base that is large enough to prevent complete underetching (Fig. 10.1(f)). Figure 10.2 shows a scanning electron micrograph of one of the cantilevers that was fabricated following the steps described above. It consists of a metallic structure machined out of a 350 nm thick metallic layer (30 nm chromium plus 320 nm gold) that was deposited on top of a 125 μm diameter fiber. The cantilever itself is 11 μm long and 7 μm wide. Its free hanging end is equipped with an 11 μm diameter paddle that, by design, is aligned with the core of the fiber. To demonstrate that the device works

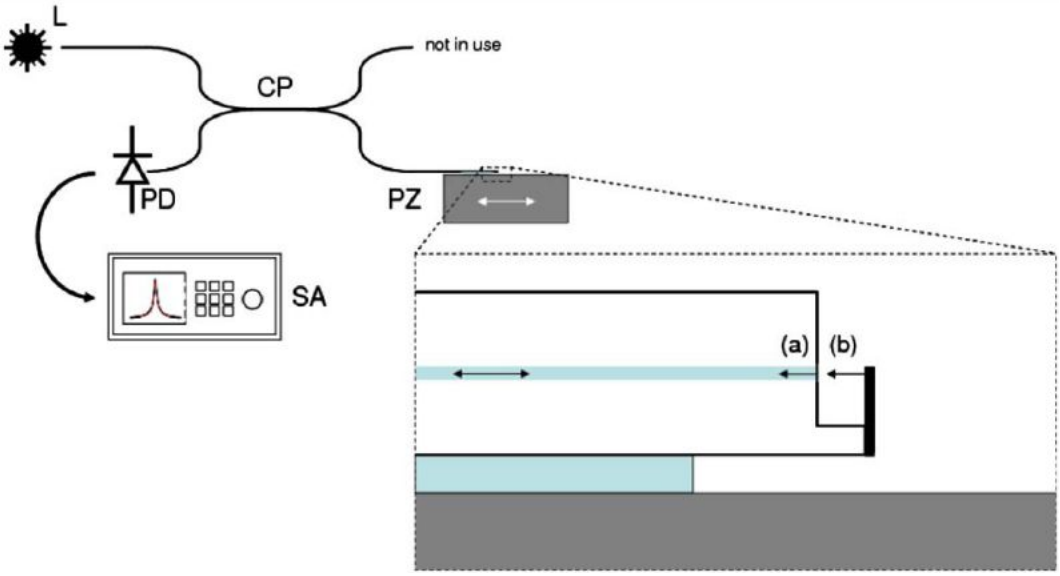

Figure 10.3: Sketch of the experimental setup used to measure the resonance frequency of the fiber-top cantilever shown in Fig. 10.2. L: laser, CP: coupler, PZ: piezoelectric transducer, PD: photodiode, SA: spectrum analyzer. Inset: sketch of the interferometric principle used to detect the bending of the cantilever. Arrows (a) and (b) indicate the light reflected by the fiber-to-air interface and by the cantilever, respectively.

according to design, we mounted the device in the setup sketched in Fig. 10.3. The machined end of the fiber is anchored to a piezoelectric transducer that is driven with a random noise voltage input. The other end of the fiber is plugged to an optical fiber interferometer that couples a laser source into the fiber and measures the amplitude of the interference between the light reflected by the fiberto- air interface and that is reflected by the cantilever. From the interference signal, which depends on the separation between the two reflecting points, one can remotely detect the amplitude of the cantilevers bending with precision, comparable to that obtained with optical triangulation techniques [7, 43]. In our experiment, the output of the interferometer is directly coupled to a spectrum analyzer which is used to localize the mechanical resonance frequency of the cantilever.

10.3 Performance

In Fig. 10.4, we report the result of the measurement obtained under ambient conditions. The resonance curve peaks at 447 kHz, with a mechanical quality factor of 98. Because the weight of the cantilever is approximately equal to 1:1 pg (volume × density with density gold = 19300 kg/m^3, density chromium = 7140 kg/m^3, volume gold cantilever = 24.6 μm^3, volume chromium cantilever = 2.3 μm^3, volume gold paddle = 30.4 μm^3, volume chromium paddle = 2.8 μm^3), one obtains a mass sensitivity of about 5 ag/Hz. This result is comparable with those obtained with similar cantilevers [174]. We believe that the approach suggested in this Letter can be successfully used as a cost effective method for series production of metallic cantilevers on top of an optical fiber. Similar steps can be followed to produce cantilevers of different dimensions and materials. Using techniques developed in the telecommunication industry, the readout can be multiplexed to interrogate arrays of sensorsa major requirement in most cantilever based biochemical sensors [169]. This work thus paves the way for the development of a new platform of all-optical, user-friendly biochemical detectors for remote sensing in critical environments. For the latter application, it might be interesting to explore whether it is possible to excite the cantilever optically (see for example [175]), avoiding in this way the use of the piezoelectric element.

Acknowledgements – The authors acknowledge Anahita Sadeghzadeh for providing part of the drawings. This work was supported by the European Research Council under the European Community's Seventh Framework Programme (FP7/2007–2013)/ERC grant agreement 201739.

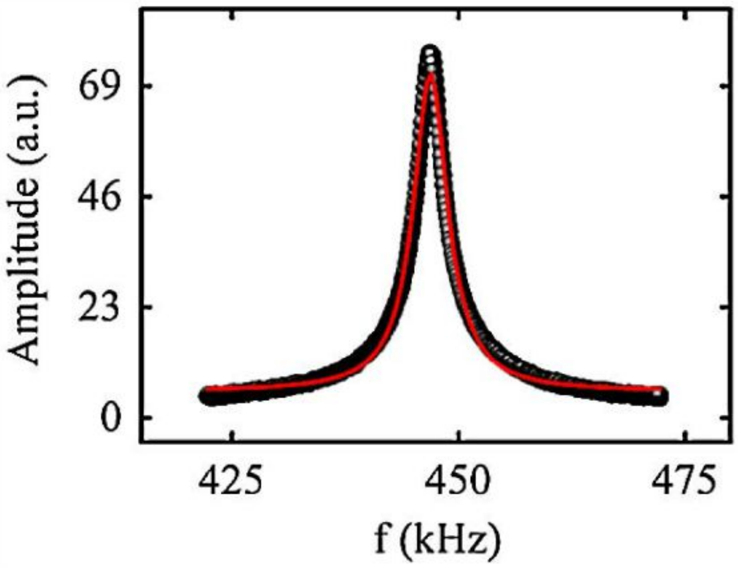

Figure 10.4: Measured spectrum of the resonance curve (in air) of a fiber-top cantilever fabricated with a topdown approach. The red curve represents a Lorentzian fit through the data. The resonance frequency is 447 kHz, and the mechanical quality factor is 98.

Chapter 11

Summary and outlook

11.1 Fiber-top and ferrule-top cantilevers for atomic force microscopy and scanning near field optical microscopy

Fiber-top and ferrule-top cantilevers (FTC) are a new generation of all optical, monolithic, self-aligned microdevices. They are obtained by carving a cantilever on the cleaved end of an optical fiber (fiber-top) or on a ferrule terminated fiber (ferrule-top). FTCs rely on Fabry-Perot interferometry to measure the deflection of the cantilever with subnanometer deflection sensitivity. FTCs specially developed for scanning probe microscopy are equipped with a sharp tip that has the dual function of probing the topography and collecting/emitting light. We perform the scanning probe microscopy using these probes in air, liquid and at low temperature (12 K). The light emission/collection functionality of FTC probes also allows one to combine scanning near field optical microscopy (SNOM) and optical transmission microscopy with contact and non-contact mode atomic force microscopy (AFM). This makes FTCs ideal for AFM+SNOM on soft samples, polymers and biological specimens, where bent fiber probes and tuning fork based systems would not be recommended because of the high stiffness of those probes. We demonstrate here the capability of fiber-top cantilevers to measure deflection and collect near field optical signal, and also the capability of ferrule-top cantilevers for simultaneous optical transmission microscopy and topography of SNOM gratings. Thanks to their unique features, FTCs also open up possibilities for UV nanolithography and on-demand optical excitation at nanoscale.

This part is based on paper:

D. Chavan, G. Gruca, T. van de Watering, K. Heeck, J. Rector, M. Slaman, D. Andres, B. Tiribilli, G. Margheri and D. Iannuzzi, *Proc. SPIE 8430, Optical Micro- and Nanometrology IV* **8430**, 84300Z, (2012)

11.1.1 Introduction

The Atomic force microscope (AFM)[16], which falls under the category of scanning probe microscope, has become an indispensable tool for imaging as well as for the characterization of the physical, chemical, electrical, electrochemical and optical properties of materials at nanoscale. The last decade witnessed the development of novel methods for sample scanning [93, 94, 176], new probe geometries [177, 178] and control electronics [96, 98], which contributed towards improved performance, resolution and speed of imaging. In spite of this tremendous development the use of AFMs outside the research laboratories has been hampered by its operational complexity. Most AFMs rely on optical triangulation techniques to measure the deflection of the cantilever, but the procedure to align the laser spot required before operating it might prove complex for an untrained professional from outside the research laboratory. Furthermore, the use of AFMs for imaging samples in liquids needs much expertise and even proves challenging for trained users. On the other hand alternative detection schemes, like piezoresistive sensing, can be used, but put limitations on imaging in liquids. Hence a need is evident for an all optical, user friendly, compact atomic force microscope. In 2006, Iannuzzi et al, presented a new device, called fiber-top cantilever[7], obtained by carving a cantilever on top of a cleaved 125 μm diameter optical fiber by focused ion beam milling (FIB). Light shone from the other end of this fiber detects the deflection of the cantilever with nanometer resolution. Applications of fiber-top cantilever probes were demonstrated for sensing [11] and atomic force microscopy[9]. Unfortunately, fiber-top cantilever probes are fabricated by focused ion beam milling, an extremely expensive and time intensive technique. To address this problem, in 2010 we proposed to fabricate a cantilever on top of a glass ferrule (3 × 3 × 7 mm), which has dimensions one order of magnitude bigger than the optical fiber. This new device, called ferrule-top cantilever probe [51], retains all the advantages of fiber-top cantilever probes with the major benefit of cost effective fabrication and possibility of series production. With a small modification to the fabrication process, the optic fiber tip that scans the sample for topological information for fiber-top and ferrule-top probes can also simultaneously collect/emit light at nanoscale. Hence these probes can be in principle used for scanning near field microscopy and have advantages over current techniques (e.g. bent fiber and tuning fork) in terms of simplicity of operation, stiffness and force resolution. Here we present the fabrication process of ferrule-top cantilever probes, readout for ferrule-top probe, setup for atomic force microscopy and atomic force microscopy combined with optical transmission microscopy.

11.1.2 Ferrule-top probe fabrication

Ferrule-top cantilever [51] probes are obtained by carving a cantilever on top of a glass ferrule (VitroCom Inc.). Previously we reported methods to entirely carve the cantilever using a laser ablation system (Optec System with Lumera Laser source)[51, 52, 71]. Here we present an alternative fabrication process that minimizes the use of laser ablation and instead uses a wire cutter for bulk material removal. Some of the important steps of ferrule-top fabrication processes are shown in Fig. 11.1. The building block for a ferrule-top probe is a glass ferrule (3 × 3 × 7 mm) with two bore holes of 125 μm and 50 μm diameter (Fig. 11.1(i)). As a first step for fabrication, the glass ferrule is mounted on the wire cutter (Well Diamantdrahtsagen GmbH) to obtain a flap like structure on top of the glass ferrule (Fig. 11.1(ii)). The thickness of this flap determines the thickness of the cantilever. With this method of fabrication, one can obtain cantilevers with thickness of 45 μm onwards. The ferrule with flap is then mounted on the laser ablation system to cut the portions of the flap to obtain a cantilever of desired shape and dimensions as shown in FIG. 11.1(iii). A

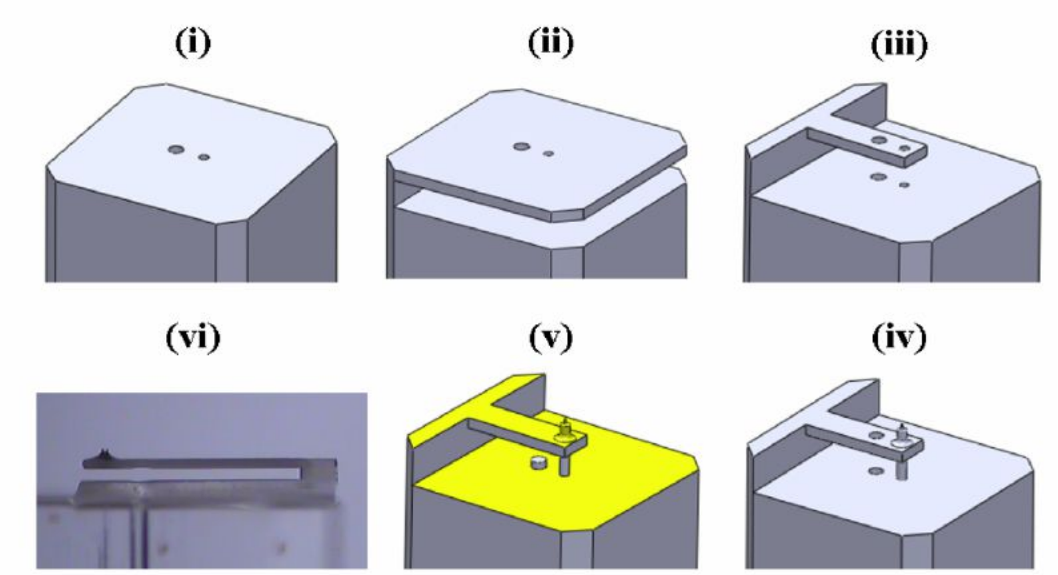

Figure 11.1: Fabrication process for ferrule-top probe for atomic force microscopy (not to scale): (i) glass ferrule 3 × 3 × 7 mm with two bore holes of 125 μm and 50 μm diameter; (ii) flap of thickness ∼45 μm created by using wire cutter; (iii) carving of cantilever from the flap by laser ablation; (iv) gluing of tipped fiber in 50 μm bore hole; (v) filling the 125 μm hole in cantilever with UV curable glue, sputtering the entire probe with chromium+gold and inserting detection fiber; (vi) optical image of ferrule-top cantilever probe with etched fiber ablated off to release the cantilever.

tipped optical fiber [179] is then slid in to the 50 μm bore hole and fixed as shown in Fig. 11.1(iv). The hole in the cantilever is filled with UV curable glue and the probe is then coated with Chromium (10 nm) + Gold (50 nm) in a sputtering system (FIG. 11.1(v)). The tipped fiber base is then ablated off by laser ablation to release the cantilever. At this point a cleaved optical fiber is slid into the 125 μm hole, which forms the detection fiber to measure the deflection of the cantilever. The other end of this detection fiber is connected to the readout explained in next section. The stiffness (k) and resonance frequency (f) of the probe can be tuned by controlling the dimensions of the cantilever during fabrication. For the probe presented here, the length of the cantilever was 1550±10 μm, width 220±10 μm and thickness of 45±5 μm.

11.1.3 Ferrule-top readout

The readout of fiber-top and ferrule-top cantilever probe records the deflection of the cantilever based on Fabry-Perot interferometry. The readout scheme used for the ferrule-top probe is shown in Fig. 11.2. An infrared laser is connected to an optic fiber coupler, wherein one arm is connected to the detection fiber and the other arm is not in use. The photodiode gives the intensity of the light reflected back from the cantilever. Thus the photodiode output is the result of interference between the light reflected at fiber-to-gap interface, the light reflected by gap-to-cantilever interface, and the light reflected at the cantilever-to-metal interface and its amplitude is given by[11]:

$$W\left(d\right) = W_0 \left[1 + V cos\left(\frac{4\pi d}{\lambda} + \varphi_0\right)\right], \tag{11.1}$$

where d is the separation between the fiber-to-gap and the gap-to-cantilever interfaces, ϕ_0 is a constant phase shift that only depends on the geometry of the cantilever, λ is the wavelength of the laser, W_0 is the midpoint interference signal and V is the fringe visibility. Figure 11.3 shows the photodiode output while bending the cantilever by pressing it against the glass sample surface. As seen in Fig. 11.3, the photodiode output $W(d)$ is at the center of the interference fringe and varies in accordance with Eq. 11.1 as the separation distance d changes with bending of the cantilever. The initial photodiode output $W(d_i)$ depends on the geometry of the probe and wavelength of the laser. Depending upon the measurement requirement and mode of imaging (contact mode or non-contact mode) one might need to tune the initial photodiode output to the desirable location on the interference fringe. At this point, the geometry of the probe is not a possible parameter to control as the dimensions and gap distance d are fixed during fabrication. Hence, one can consider a tunable wavelength laser source for adjusting the initial photodiode output. The importance of tunable wavelength laser source is explained more in detail in the next section.

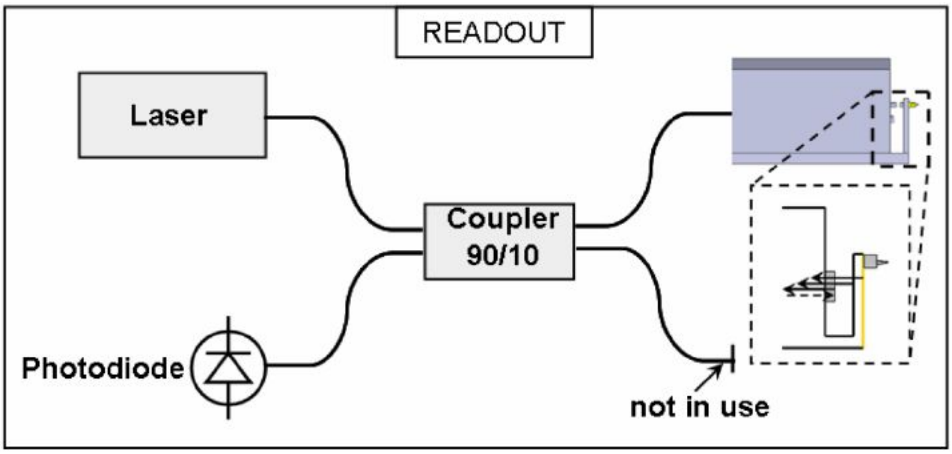

Figure 11.2: Detection scheme for the ferrule-top cantilever probe.

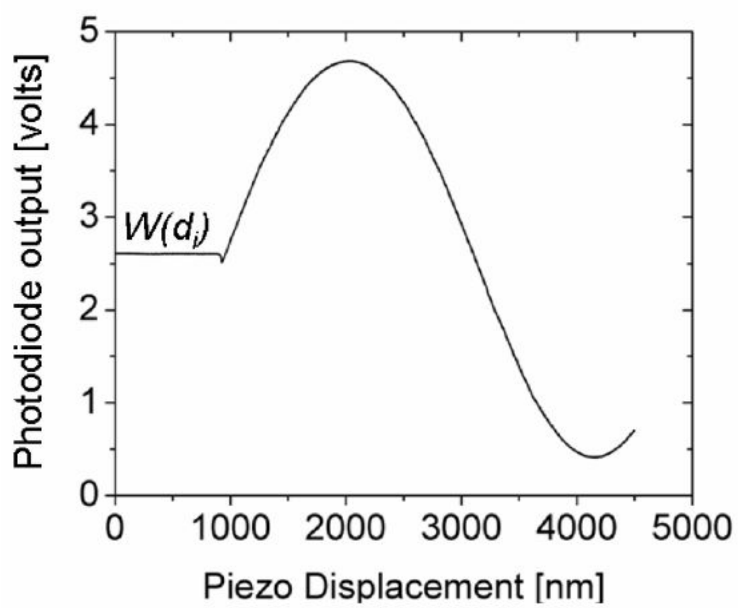

Figure 11.3: Photodiode output upon cantilever deflection.

11.1.4 Ferrule-top atomic force microscope

We demonstrate here the imaging capability of ferrule-top cantilever probe in three different environments-air, water and at low temperature (12 K). The ferrule top probe was mounted on our atomic force microscope setup for imaging in water, on a commercial atomic force microscope from ElbaTech Srl for imaging in air and on an atomic force microscopy system AttoAFM Ixs from Attocube Systems AG for imaging at low temperature (12 K). The schematic of our atomic force microscope system used for contact mode imaging in liquid is shown in Fig. 11.4. As seen in Fig. 11.4, the ferrule-top cantilever probe is attached to a small metal piece, which is attached to a piezoelectric actuator (AE0203D04F, Thorlabs Inc.) by a small magnet. The sample to be imaged is a standard calibration grating with a step size of 20±1.5 nm (TGZ1, NT-MDT). The sample is glued at the bottom of a petri dish which is mounted on XY scanner (ANSxy50, Attocube AG) for raster scanning during the imaging. This XY scanner is mounted on top of Z-positioner (ANPz51/RES, Attocube AG) that can be operated in slip-stick and scanner mode. The slip-stick mode

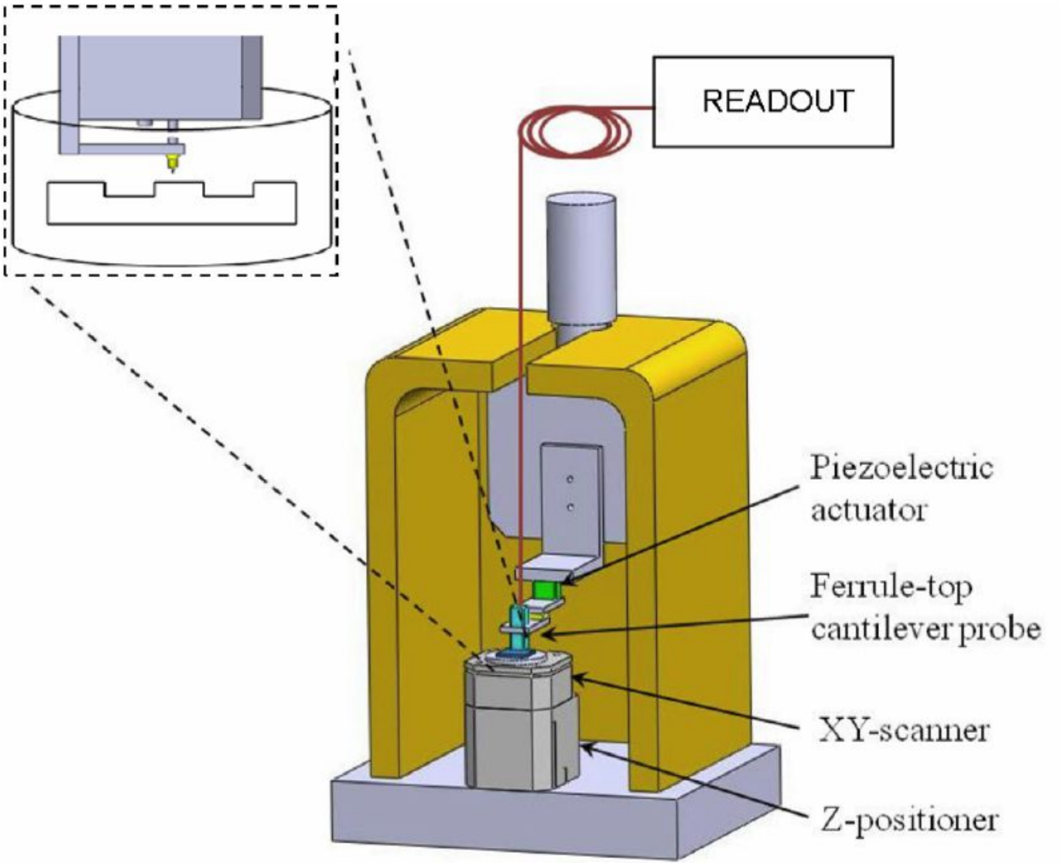

Figure 11.4: Schematic of our atomic force microscope used for imaging in liquid

of the Z-positioner is used for coarse positioning to engage the probe and the sample. The scanner mode of the Z-positioner is used to close the feedback loop to keep the cantilever deflection constant while imaging. In this experiment we used a fixed wavelength laser ($\lambda = 1310$ nm), which sets limitations on the setpoint force applied during contact mode imaging. For detailed explanation about the control system used for imaging on this setup, we refer the reader to Ref. [52]. One such image obtained for contact mode scanning in liquid is shown in Fig. 11.5(II). To demonstrate plug-and-play capability of the ferrule-top cantilever probe, we performed contact mode imaging in air on a commercial atomic force microscope system from ElbaTech Srl, Italy. In this experiment we used a tunable wavelength laser source that comprises a broadband SLD source (Thorlabs Inc.) and a tunable optic fiber filter (Agiltron Inc.). Apart from this tunable laser source, the readout schematic remains exactly the same as mentioned earlier. In case of fixed wavelength laser source, the initial photodiode output can range anywhere on the interference fringe depending on the geometry of the cantilever and gap size. Now, for the closed loop operation one needs to fix the setpoint which could either be a maxima (or minima) of the interference fringe for control technique described in Ref. [52], or midpoint of the interference fringe. To achieve this desired setpoint position on interference fringe, one needs to bend the cantilever till the desired setpoint is reached. On the other hand, for tunable wavelength laser source, the desired setpoint on the interference fringe can be achieved by tuning the wavelength, instead of bending the cantilever. This gives the tunable wave-

I IN AIR	II IN WATER	III AT LOW TEMP. (12 K)
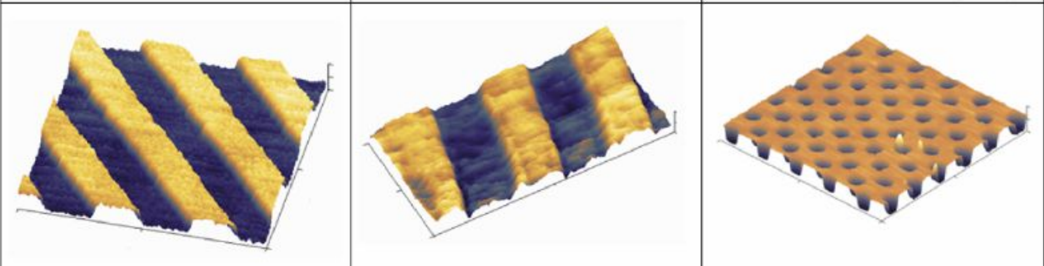		
Scan size: 10 X 10 μm	**Scan size: 7.5 X 3.7 μm**	**Scan size: 8.7 X 8.7 μm**
Step height: 20 nm ± 1.5	**Step height: 20 nm ± 1.5**	**Step height: 20 nm ± 2**
Resolution : 256 X 256 pixel	**Resolution : 128 X 63 pixel**	**Resolution : 150 X 150 pixel**

Figure 11.5: Contact mode imaging of grating sample using ferrule-top cantilever probe: (I) Contact mode image in air for probe mounted on Elbatech AFM system; (II) Contact mode image in water for probe mounted on our AFM system; (III) Contact mode image at low temperature (12 K) for probe mounted on AttoAFM Ixs system from Attocube AG.

length laser readout a better setpoint force resolution during the measurement with respect to the non-tunable readout. The contact mode image obtained for this experiment is shown in Fig. 11.5(I).For imaging at low temperature (12 K) the ferrule-top probe was mounted on AttoAFM Ixs from Attocube Systems AG. For the details of this experiment, we refer the reader to Ref. [71]. The contact mode image obtained at low temperature is shown in Fig. 11.5(III). Contact mode topography images (shown in Fig. 11.5) obtained by ferrule-top cantilever probes clearly demonstrates the capability of the probe to operate in different environments and its adaptability to commercial AFM systems. The topography image quality obtained is consistent and comparable to that of a commercial silicon/silicon nitride cantilever probe. The contact mode image in liquid (Fig. 11.5(II)) shows higher noise due to a problem in the mechanical attachment of the sample in the petri dish. The sharpness of the image is presently limited by the tip radius which is in order of ∼100 nm. This can be addressed in future by use of customized optical fiber that produce much sharper tips upon etching.

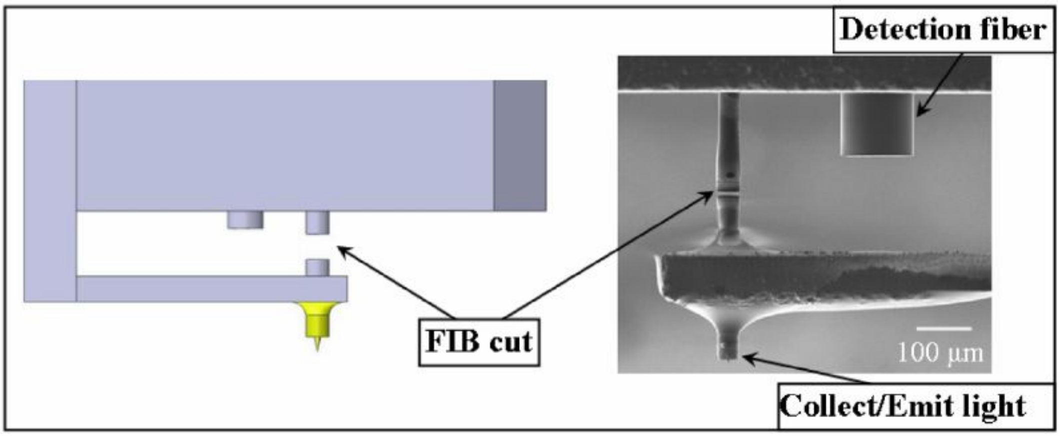

Figure 11.6: (Left)Schematic of modified ferrule-top cantilever probe with focused ion beam (FIB) cut; (Right) scanning electron microscopy (SEM) image of the probe.

11.1.5 Combined AFM and optical transmission microscopy

Scanning near field optical microscopy (SNOM/NSOM)[180, 181] is considered as one of the most important tools for optical characterization beyond the diffraction limit. Many techniques are proposed for near field imaging, of which use of optic fiber has gained wide acceptance due to its simplicity of operation and fabrication. In this technique an optic fiber is pulled or etched to obtain a sharp tip with subwavelength tip aperture. This optic fiber is then used to collect (or emit) light from the sample at distance much smaller then the wavelength of the light ($d \ll \lambda$) while scanning over the sample. To maintain a constant nanometer separation from the sample surface while scanning, the optic fiber tip needs to have a feedback on the distance between the tip and sample. To achieve this goal one typically uses tuning forks or bent optical fibers. In techniques using tuning forks, an etched (or pulled) optical fiber is glued to a tuning fork. The tuning fork has an excitation electrode to excite it at resonance frequency and a readout mechanism to monitor the shift in resonance frequency. As the optic fiber glued to the tuning fork approaches the sample surface, it experiences surface forces that cause a shift in its resonance peak. This shift is related to the distance from the surface, and can be used as feedback signal to maintain a constant distance from the sample surface. The feedback control system in this technique demands high quality factor to maintain the close loop while scanning. As a result, it becomes challenging to image samples in liquid, as the viscous damping causes drop in quality factor and makes it difficult for the control system to close the loop. Hence the tuning fork technique is not suitable for imaging in liquid. Also the shear force mode operation of tuning fork puts limitation on the speed of scanning. For the other widely used technique for SNOM, the pulled (or etched) optical fiber is bent (usually by heat) in form of a cantilever. This technique uses optical triangulation method to detect the deflection of the bent optical fiber while scanning. This technique does not depend on the high quality factor for its closed loop operation and hence can also be used for imaging samples submerged in liquid. However alignment of laser spot on bent fibers needs much expertise and the laser spot can interfere with the SNOM signal. Also the bent optic fiber probes have usually high stiffness making them unsuitable for imaging soft samples like cells, tissues and polymers. Considering these limitations of both the techniques used for near field optical microscopy, fiber-top technology can be an interesting substitute to consider.

In early 2010, some of us demonstrated the use of fiber-top cantilever probe for scanning near field optical microscopy [72]. The fiber-top cantilever probe has the advantage of having a lower spring constant (compared to bent fiber). Furthermore, it requires no optical triangulation (unlike bent fibers) and can be operated in liquids. However, fiber-top cantilever probes are fabricated by focused ion beam milling, which makes them extremely expensive and time intensive to fabricate. On the other hand, ferrule-top cantilever probes are easy to fabricate and the tip that scans over the sample to provide topological information, can also be used simultaneously for collecting/emitting light while scanning. To encompass this optical coupling from the tipped fiber, the ferrule-top probe fabrication process needs a small modification. During the fabrication of ferrule-top cantilever probe, at the process step shown in Fig. 11.1(V), the tipped fiber base is ablated off to release the cantilever. Instead of ablating off the tipped fiber, a focused ion beam cut needs to be made to release the cantilever and achieve optical coupling from the tip. The focused ion beam cut ensures optically smooth surfaces for optimum light coupling, which can not be achieved by laser ablation. The schematic of modified ferrule-top cantilever probe with focused ion beam cut is shown in Fig. 11.6.

As shown in Fig. 11.6, with the FIB cut on tipped fiber, light can be coupled in or collected from the tip. The FIB cut creates sufficient gap ($\sim 3\mu$m) to allow unrestricted bending of the cantilever and at the same time ensures adequate optical coupling. As the entire probe was coated with Cr+Au during the fabrication process, FIB was used to remove this metal coating from the tip aperture to ensure light transmission through the tip. Depending upon mode of operation, i.e. light collection or emission, the tipped fiber can be connected to a photomultiplier tube (PMT) or to a laser source respectively. The detection fiber (shown in Fig. 11.6) is connected to readout to monitor the cantilever deflection while scanning. The schematic of the setup used for combined AFM and optical transmission microscopy is shown in Fig. 11.7. To demonstrate the feasibility of combined AFM and optical transmission microscopy, the tipped fiber was connected to a laser source (λ = 470 nm). A calibration grating (SNG01, NT-MDT) with periodic rhomboidal patches of

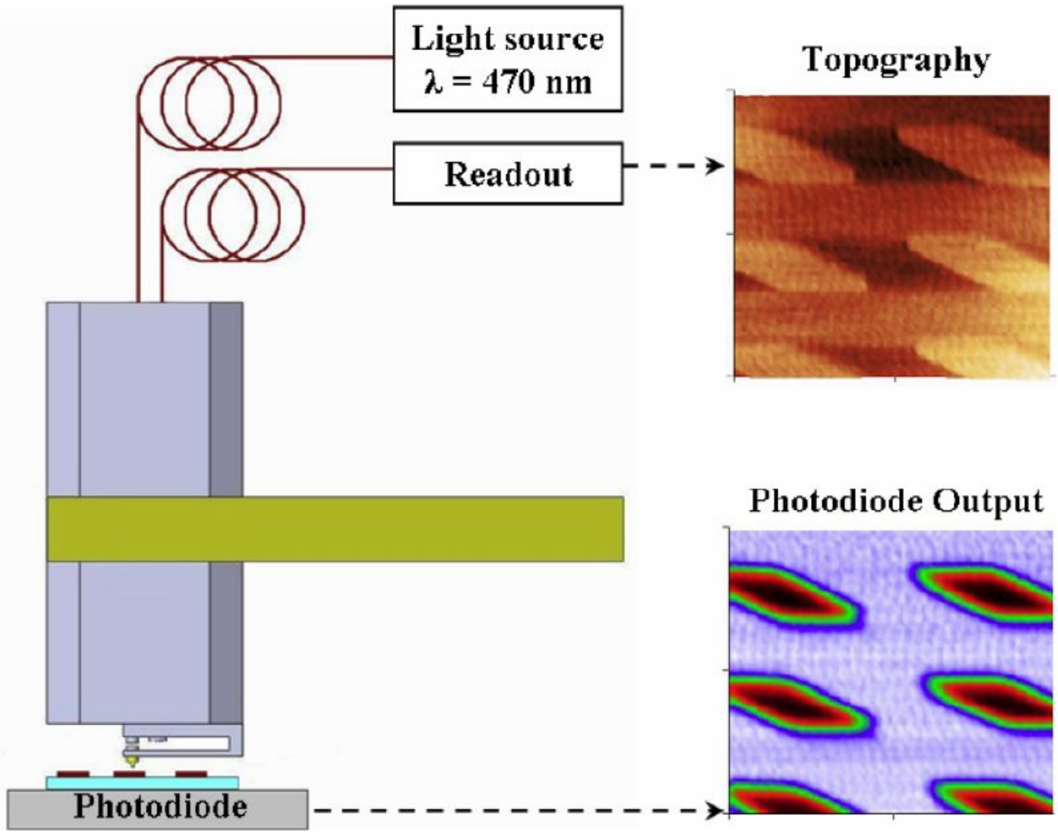

Figure 11.7: Schematic of the setup for combined AFM and optical transmission microscopy.

vanadium (20-30 nm) on quartz substrate, was mounted on a photodiode. The output of the photodiode after amplification was acquired as an auxiliary data channel. The probe was scanned over the grating sample in contact mode, with the detection fiber monitoring the deflection of the cantilever and the tipped fiber illuminating the sample with 470 nm laser light. The sample topography image acquired during the scan and simultaneous optical transmission measured by the photodiode are shown in Fig. 11.7. It can be seen from the two images (topography and photodiode output) that, when the tip is scanning over the vanadium metal coating, the optical transmission to photodiode is almost blocked. On the other hand, when the tip is scanning over the quartz surface, the photodiode records the highest transmission signal. At the edges of the metal coating, the tip aperture size and the distance of the grating from the photodiode surface, determine the optical transmission. The lateral resolution of optical transmission can be improved through optimizing the ferrule-top probe fabrication process. One can achieve this by avoiding the metal deposition (Cr+Au) on tip of the fiber during the fabrication process and hence avoid the use of FIB to remove the metal at the tip aperture. To further improve the optical signal quality, one can consider use of a multimode optical fiber to enhance the transmission in the visible wavelength range.

11.1.6 Conclusions

We have demonstrated a novel all-optical device for atomic force microscopy in air, liquid and at low temperature. The images obtained are consistent in quality and comparable to images obtained using commercial cantilever probes. The device is virtually plug-and-play and can adapt to any commercial atomic force microscopes. The combined optical imaging with the modified ferrule-top probe opens new possibilities for simultaneous material property mapping in demanding environments, which is not possible with currently available instruments.

Acknowledgements – This work was supported by the European Research Council under the European Communitys Seventh Framework Programme (FP7/2007-2013)/ERC grant agreement number 201739.

11.2 Development of fiber optic ferrule-top cantilevers for sensing and beam-steering applications

Ferrule-top (FT) cantilevers are a new generation of all-optical micromechanical sensors obtained by carving microstructures on the top of ferrule terminated fibers. In this paper, we will demonstrate how this plug-and-play design can be used for the development of a new generation of sensors and actuators for harsh environments, where commercially available devices would be prone to failure. Ferrule-top sensors can work in two main modes : static and dynamic. The static mode is based on recording elastic deflections of the cantilever; the dynamic mode relies on tracking changes in its mechanical properties (resonance frequency, quality factor). Depending on the application, one can choose which mode is most suitable or combine both to achieve best performance. We will illustrate the relation between a specific measured quantity (humidity, flow) and the behavior of the sensor. Further, we will show the setup in which the sensor can be actuated using light, giving the possibility to excite the cantilever without any electronics on the sensing head. This technique might be used for the development of fully optical beamsteering microdevices.

This part is based on paper:

G. Gruca, D. Chavan, A. Cipullo, K. Babaei Gavan, F. De Filippis, A. Minardo, J. Rector, K. Heek, L. Zeni and D. Iannuzzi, *Proc. SPIE, Optical Sensing and Detection II* **8439**, 84390E, (2012)

11.2.1 Introduction

Over the last decade optical fiber sensors (OFS) have been increasing their position as one of the important measurement platforms in science and industry. They are being used to explore new ideas in measurement techniques and to optimize existing solutions. Thanks to their advantages (e.g. high sensitivity and high resistance to harsh environments) they have been recognized as the most effective solution to many crucial metrological problems [182–185]. Moreover, a growing need of multiple point measurements with characteristic for OFS simplicity and possibility of building remote sensing networks makes them very interesting also beyond industrial applications. Since a few years, contribution of fiber sensors in medical diagnosis, therapies and health monitoring has been noticed [186–188]. The market for such sensors is rapidly growing, accompanied by strong support from a continuous progress in the development of new light sources and measurement techniques. All that clearly shows that there is still need to explore new ideas and optimize existing solutions. Based on that, in 2009 we have introduced a new type of all-optical device : the ferrule-top (FT) sensor [100]. A ferrule-top sensor is a monolithic micromechanical structure fabricated at the top of ferruled optical fiber by various techniques (e.g. laser ablation). The movement of the structure can be monitored by means of laser light coupled into the fiber from the opposite end. According to the same principle, it is also possible to excite the vibrations of the structure using an additional source of light. This unique feature, makes FT sensors extremely compact and insensitive to high electric and magnetic fields. The geometry of the sensor can be changed depending on the application. In most of the cases the micromechanical element located at the top of the ferrule is a simple beam clamped on one side. The sensor is small and robust and does not require any alignment (a very important advantage for applications in harsh environments, both in air, liquid and vacuum). Its monolithic design in connection with the low thermal expansion coefficient of the ferrule material minimizes thermal drifts and improves accuracy. Ferrule-top sensors are extremely versatile and can be used as humidity [76], wind velocity [73] or surface topography [52] sensors.

Fabrication of the ferrule-top sensors

A standard ferrule-top sensor is fabricated from a $3 \times 3 \times 8$ mm^3 borosilicate (Tab. 11.1) glass ferrule equipped with a 125 μm hole in the middle. During the fabrication procedure [51], where a picoseconds laser ablation system is involved, a micromechanical cantilever (or any other desired geometry) is created on the top of the ferrule Fig. 11.8. Typical dimensions of the fabricated micromechanical beam are $2800 \times 220 \times 35$ μm^3. As a next step, a precisely cleaved single mode fiber (typically SMF-28 [189]) is inserted in the central hole of the ferrule and fixed by gluing. The part of the cantilever just

Density	2,23 g/cm^3
Young Modulus	62.7 GPa
Poisson ratio	0.20
Softening point	821^{o}C
Refractive index	1.54
Thermal expansion coefficient	$3{\cdot}10^{-6}K^{-1}$

Table 11.1: Typical borosilicate glass properties.

in the opposite of the measurement fiber has to be filled with a highly reflective layer. This step creates a cavity between the fiber end and the cantilever surface. Using the technique described in the next subsection, it is then possible to determine changes in the cavity size due to movement of the cantilever with subnanometre resolution.

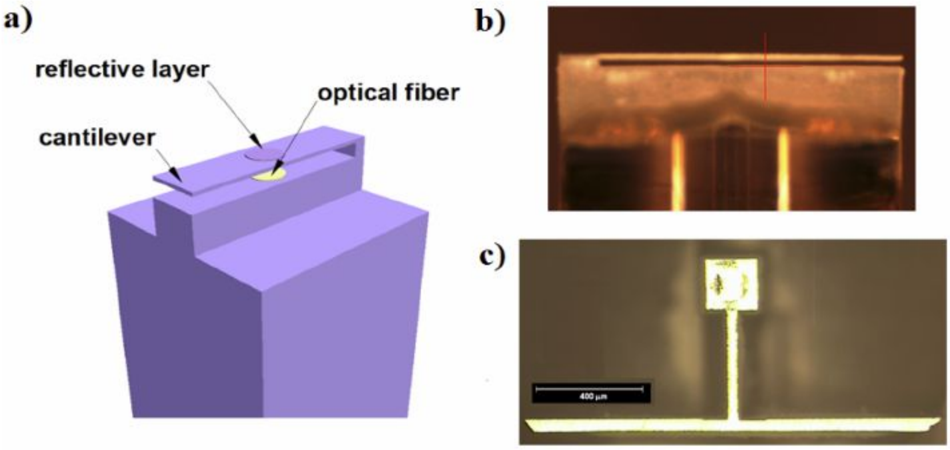

Figure 11.8: Three dimensional visualization of the ferrule-top cantilever sensor (a) and its optical microscope image (b). It is also possible to fabricate different geometries than a simple cantilever on the top of the ferrule – microscope image of torsional cantilever (c)

Readout

The low finesse Fabry-Perot fiber cavity created between the fiber-to-air interface, where reflection is of the order of 4%, and the reflective surface of the cantilever allows the user to determine the movements of the cantilever [43]. The output of such interferometer can be expressed as:

$$I\left(d\right) = I_0\left[1 + V cos\left(\frac{4\pi d}{\lambda} + \varphi_0\right)\right] \tag{11.2}$$

where ϕ_0 is a constant that comes from the initial geometrical conditions, λ is the wavelength of the readout laser and d is the bending distance of the cantilever. Parameters V and I_0 are calculated as follows:

$$I_0 = \frac{I_+ - I_-}{2}; V = \frac{I_+ - I_-}{I_+ + I_-}, \tag{11.3}$$

where I_+ and I_- are equal to maximum and minimum signal level on the photodetector. The readout part of the setup (Fig. 11.9) is based on a tunable laser which operates at the C band (1529–1564 nm), an optical 90/10 fiber coupler and an InGaAs photodiode. The tunable laser is tuned to the point of maximal sensitivity the quadrature. The bending resolution of the setup is typically lower than 1 nm in 100 kHz bandwidth.

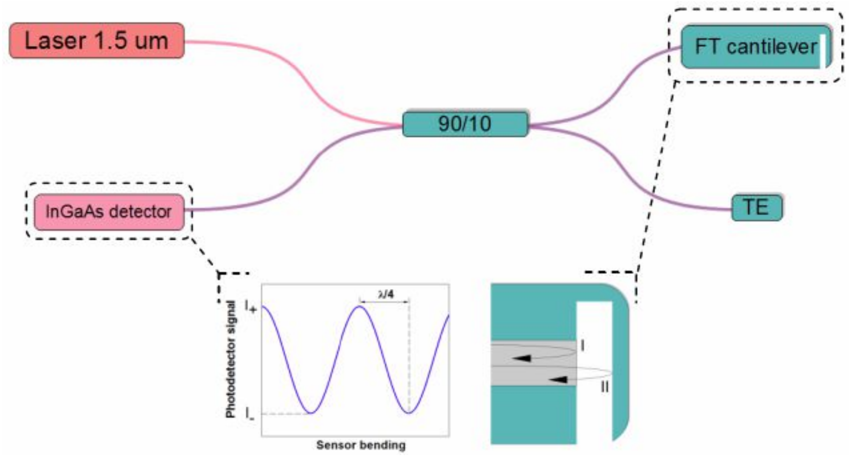

Figure 11.9: Schematic view of the readout (TE terminated end of the fiber). Light reflected from interface I and II creates the interference pattern on the photodetector.

11.2.2 Static and dynamic measurement modes

The basic working principle of FT sensors is based on optically monitoring the mechanical response of the microstructures. Ferrule-top sensors are capable of operating in two different modes: static and dynamic. One can choose the more appropriate for the particular application or combine the two to get additional information about the measured quantity. Both the static bending and the mechanical frequency response can be caused by a change in one or more physical parameters i.e. pressure, mass or surface stress variations.

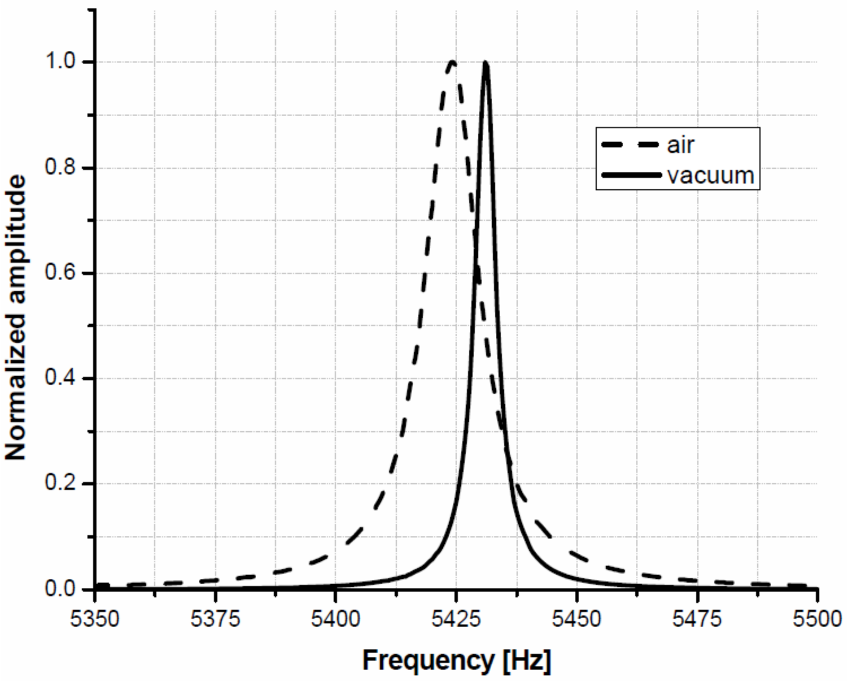

Figure 11.10: Frequency response of a FT sensor in air and vacuum (10-5 mbar). The quality factor and resonance frequency are f_a=5424.1 Hz; Q_a=402 in air and f_v=5431.1 Hz; Q_v=1018 in vacuum.

Dynamic mode

Dynamic behavior of the ferrule-top cantilever can be modeled as a simple harmonic oscillator:

$$\frac{\partial^2 x(t)}{\partial t^2} + 2\xi \frac{dx}{dt} + \omega_0^2 x = \frac{1}{m} F_0 cos(\omega t) \tag{11.4}$$

where ω_0, k, Q, $x(t)$, ξ indicate respectively: resonance pulsation, spring constant, quality factor, bending of the cantilever and damping coefficient. The right term of the equation describes the periodic driving force that excites the vibrations of the cantilever. As one can suspect, the dynamical response is strongly connected with the properties of the surrounding media: its density and its viscosity (Fig. 11.10). This fact can be easily explained by different damping coefficients, in air and vacuum, which are related with the quality factor. This effect can be used to build sensors that are able to distinguish different type of gases. It can be also shown that the FT cantilever is not only sensitive to rheological properties of the medium in which it is immersed. It is also sensitive to a mass variation and to surface stress modification. To prove that, the cantilever was enclosed inside a measurement chamber where the humidity level was precisely controlled. For each level of humidity a single resonance curve was recorded (Fig. 11.11). During the experiment temperature variations were less than 0.2^{o}C. As one can notice, both the quality factor and

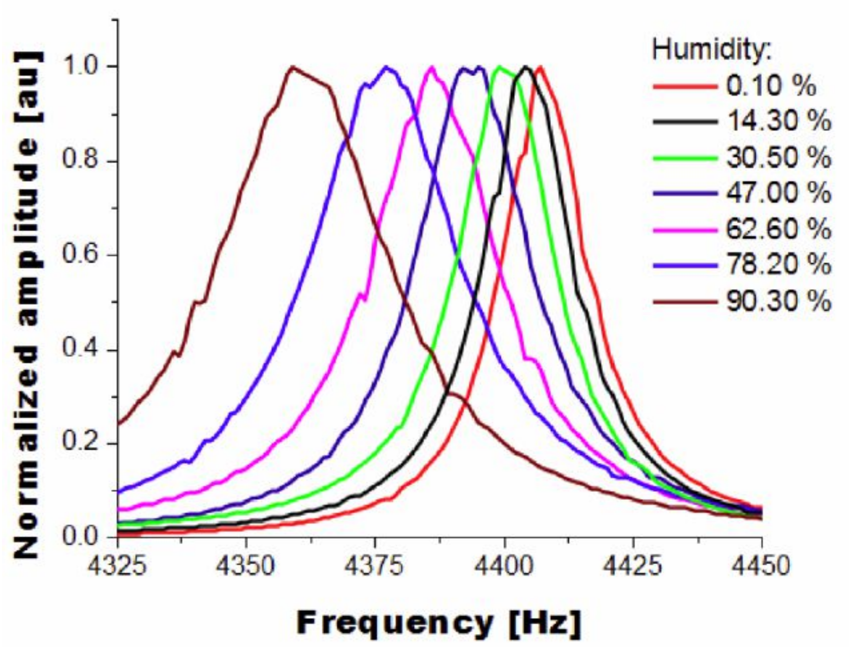

Figure 11.11: Frequency response of ferrule-top sensor to different humidity levels. Cantilever was forced to vibrations by means of piezo excitation.

resonance frequency are decreasing while humidity increases. This effect is due to water condensation on the surface of the cantilever. Water is introducing additional mass, modifying surface stress, thus affecting the overall frequency response. During the experiment a static bending of the cantilever was also observed.

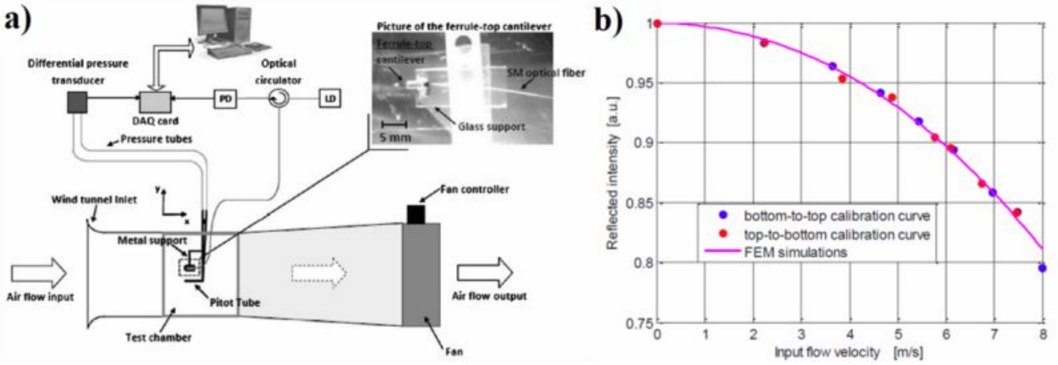

Figure 11.12: Schematic view of the setup used in wind tunnel experiment (a). Cantilever bending (b) agrees with the FEM simulation data and proves that FT sensors can be used as flow monitoring devices [73].

Static mode

In some cases the overall performance offered by dynamic mode measurements is not sufficient. When the quality factor of the FT sensor is low (e.g. in liquids) the accuracy and the sensitivity achieved in dynamic measurements are strongly limited. To overcome this issue one can record the static bending of the cantilever, which can be caused by two mechanisms: surface stress modification and external force acting on the sensor. When there is a difference in surface stress $\Delta\sigma$ between top and bottom of the sensor, the bending Δx

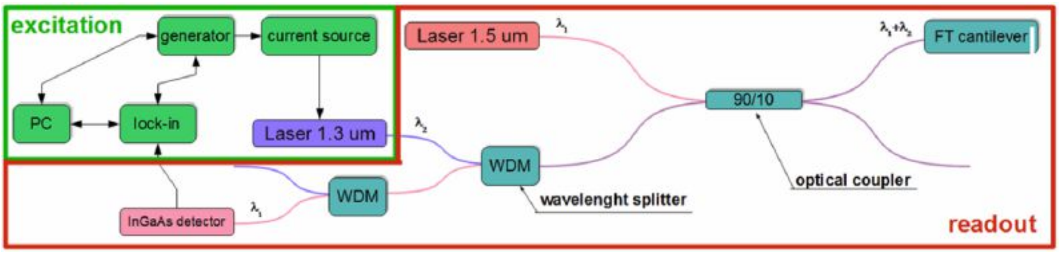

Figure 11.13: A proposed schematic of the additional photoexcitation circuit. WDM splitters are used to separate the excitation and readout wavelength.

can be described as [44]:

$$\Delta x = \frac{3l^2(1-\upsilon)}{Eh^2}\Delta\sigma \tag{11.5}$$

where l, ν, E, h are respectively the length, Poisson's ratio, Young's modulus and thickness of the cantilever. Additionally, to increase the response of the sensor its surface can be coated by an active layer. Moreover, if the layer is able to capture specific molecules from the sensor surroundings one can build highly selective biosensors. In the second case, where a direct force $F(x)$ is acting on the cantilever of a width w, its bending fulfills the equation:

$$\Delta x = 4\frac{F(x)}{Ew} \cdot \frac{l^3}{h^3} \tag{11.6}$$

As a practical illustration, an experiment in a laboratory wind tunnel was performed. An FT sensor was placed inside the wind tunnel where airflow was controlled. The bending of the cantilever was recorded as a function of air velocity from 0 to 8 m/s (Fig. 11.12). All results were compared with a reference sensor. The nonlinear behavior of the presented signal is caused by quadratic relation between velocity and pressure difference (force) acting on the sensor. Nonetheless, the achieved resolution and minimum detectable velocity in the order of 0.07 m/s confirmed the practical value of the FT cantilever as a miniature, fully optical wind velocity sensor.

11.2.3 Photoexcitation

Measurement capabilities of FT sensors in dynamic mode are hampered by the need of an external mechanical excitation. A typical excitation scheme (e.g. piezo or electrostatic excitation) involves additional device attached to the cantilever or requires further cantilever modifications. Moreover, it is very difficult to use it in liquids. To overcome these issues and in order to take full advantage of the all-optical readout, we propose to implement an excitation scheme consisting of an additional laser source (Fig. 11.13). By means of local heating and due to the stress induced across the cantilever, it is possible to excite the vibrations without any modifications of the sensor. Photothermal excitation has a lot of advantages. It is simple and allows to obtain clear frequency response, without any spurious effects which are present in case of use other excitation schemes e.g. piezo actuation in liquids. Some preliminary experiments using the scheme above were already performed (paper under preparation).

11.2.4 Towards smaller dimensions

FT cantilevers are considered as micromechanical sensors, but in some applications there is still a strong need to further decrease the dimensions. To meet these expectations and to overcome some fabrication limits we have proposed a top-down approach in fiber-top [7] cantilevers fabrication. A fiber-top sensor is smaller than its ferrule-top counterpart. The typical length of the fiber-top cantilever is less than 100 μm. It can be made out of glass or metal and uses exactly the same readout scheme as explained above. Thanks to smaller dimensions its sensitivity in some applications can by higher than that of FT sensors (about 5 ag/Hz). We refer the reader to reference [190] for further details.

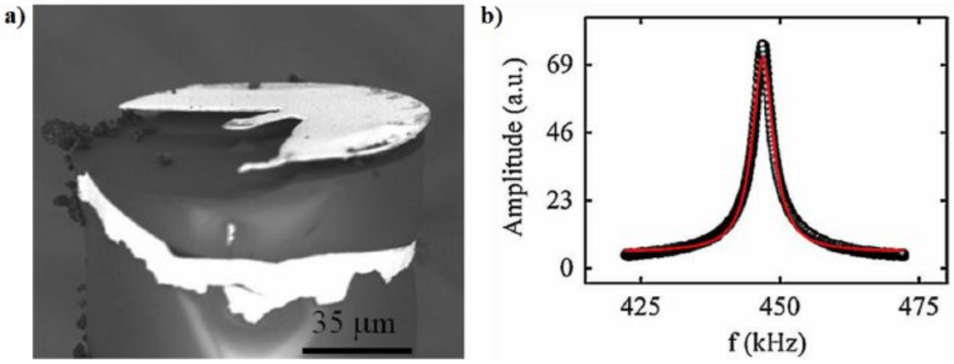

Figure 11.14: A fiber-top sensor can be used if further decrease in dimensions is required. The dimensions of the cantilever shown on scanning electron micrograph (a) are 11μm x 7 μm x 360 nm (length x width x thickness). The cantilever resonance frequency (b) is equal f_R=447 kHz [190].

11.2.5 Conclusions

Ferrule-top devices are new family of transducers that offer all the advantages of fiber optic sensors (e.g. remote sensing, insensitivity to EM noise, resistivity to harsh environments). They are small and, because they do not require any aligning procedure, easy to use. By monitoring the static bending or/and the frequency shift of FT cantilevers one can build a wide variety of sensors (e.g. pressure, velocity, humidity, surface topography). The only limitation is the presence of physical phenomena that might influence the mechanical properties of the sensor. To additionally extend their functionality, simple photoexcitation circuits attached to the readout can be implemented. Due to the unique combination of fully optical readout and excitation, FT sensors can become a significant sensing platform among already existing solutions.

Acknowledgements – The authors acknowledge support from the European COST action TD1001 OFSESA and the European Research Council under the

European Communitys Seventh Framework Program (FP7/2007-2013)/ERC grant agreement number 207139.

Appendix A

List of papers, achievements and other activities

A.1 List of papers

1. **G. Gruca**, S. de Man, M. Slaman, J. H. Rector, and D. Iannuzzi. Ferrule-top micromachined devices: a new approach to fibre-top technology. Proc. SPIE, 7503:750381, 2009.
2. **G. Gruca**, S. de Man, M. Slaman, J. H. Rector, and D. Iannuzzi. Ferrule-top micromachined devices: design, fabrication, performance. Measurement Science and Technology, **21(9)**:094033, 2010.
3. D. Chavan, **G. Gruca**, S. de Man, M. Slaman, J. H. Rector, K. Heeck, and D. Iannuzzi. Ferrule-top atomic force microscope. Review of Scientific Instruments, **81(12)**:123702, 2010.
4. P. Zuurbier, S. de Man, **G. Gruca**, K. Heeck, and D. Iannuzzi. Measurement of the casimir force with a ferrule-top sensor. New Journal of Physics, **13(2)**:023027, 2011.
5. **G. Gruca**, J. H. Rector, K Heeck, and D. Iannuzzi. Optical fiber ferrule-top sensor for humidity measurements. 21st International Conference on Optical Fiber Sensors SPIE, 7753: 775358, 2011.
6. K. Babaei Gavan, J. H. Rector, K. Heeck, D. Chavan, **G. Gruca**, T. H. Oosterkamp, and D. Iannuzzi. Top-down approach to fiber-top cantilevers. Opt. Lett., **36(15)**:2898–2900, Aug 2011.
7. A. Cipullo, **G. Gruca**, K. Heeck, F. De Filippis, D. Iannuzzi, and L. Zeni, Ferrule-top cantilever optical fiber sensor for velocity measurements of low speed air flows. 21st International Conference on Optical Fiber Sensors, 7753:77534O, 2011.

8. **G. Gruca**, D. Chavan, A. Cipullo, K. Babaei Gavan, F. De Filippis, A. Minardo, J. Rector, K. Heek, L. Zeni, and D. Iannuzzi. Development of fiber optic ferrule-top cantilevers for sensing and beam-steering applications. SPIE Optical Sensing and Detection II, 8439:84390E, 2012.

9. **G. Gruca**, D. Chavan, T. van de Watering, J. Rector, K. Heeck, and D. Iannuzzi. Ferrule-top cantilevers for measurements in harsh environments. SPIE Newsroom. 10.1117/ 2.120120 6.004225:3, 2012.

10. L. Schenato, L. Palmieri, **G. Gruca**, D. Iannuzzi, G. Marcato, A. Pasuto, and A. Galtarossa. Fiber optic sensors for precursory acoustic signals detection in rockfall events. Journal of the European Optical Society - Rapid publications, **7(0)**, 2012.

11. D. Chavan, T. C. van de Watering, **G. Gruca**, J. H. Rector, K. Heeck, M. Slaman, and D. Iannuzzi. Ferrule-top nanoindenter: An optomechanical fiber sensor for nanoindentation. Review of Scientific Instruments, **83(11)**:115110, 2012.

12. D. Chavan, **G. Gruca**, T. van de Watering, K. Heeck, J. Rector, M. Slaman, D. Andres, B. Tiribilli, G. Margheri, and D. Iannuzzi. Fiber-top and ferrule-top cantilevers for atomic force microscopy and scanning near field optical microscopy. Optical Micro- and Nanometrology IV, 8430:84300Z, 2012.

13. A. Cipullo, **G. Gruca**, K. Heeck, F. De Filippis, D. Iannuzzi, A. Minardo, and L. Zeni, Numerical study of a ferrule-top cantilever optical fiber sensor for wind-tunnel applications and comparison with experimental results. Sensors and Actuators A: Physical, **178(0)**:17–25, 2012.

14. **G. Gruca**, D. Chavan, J. Rector, K. Heeck, and D. Iannuzzi. Demonstration of an optically actuated ferrule-top device for pressure and humidity sensing. Sensors and Actuators A: Physical, **190(0)**:77–83, 2013.

15. **G. Gruca**, K.Heeck, J. Rector, and D. Iannuzzi, Demonstration of a miniature all-optical photoacoustic spectrometer based on ferrule-top technology. Opt. Lett., **38(10)**:1672–1674, 2013.

16. N. Horiuchi. Sensors: Rock-fall warning. Nat Photon, **7(3)**:167167,2013. Research highlights - sensors.

17. **G. Gruca** and K. Heeck and J. Rector and D. Iannuzzi, Demonstration of a miniature all-optical photoacoustic spectrometer based on ferrule-top technology, The Virtual Journal for Biomedical Optics, **8(6)**, 2013.

A.2 Patent applications

1. Patent application : D. Iannuzzi, **G. Gruca**, S. de Man: ”Optical Fiber, method of preparation thereof and device”, Pending: US 61/204,541, US 61/302,235, PCT/NL2010/050569

A.3 Contribution to conferences

1. Invited talk at SPIE Photonics Europe, ”Development of fiber optic ferrule-top cantilevers for sensing and beam-steering applications”, Brussels, 2012
2. Poster presentation: ”Optical fiber ferrule-top sensor for humidity measurements”, OFS 21, Ottawa, 2011
3. Poster presentation: ”All-optical gas sensor based on ferrule-top and fiber-top photoacoustic spectroscopy”, Physics@FOM conference, Veldhoven, 2013
4. Poster presentation: ”Ferrule-top cantilevers: micromachined all-optical sensors”, Physics@FOM conference, Veldhoven, 2012

Summary

Over the last decade, optical fiber sensors (OFS) have become increasingly important measurement tools for science and industry. OFS employ an optical fiber either as a sensing element to measure temperature, strain, pressure, or other quantities, or as a means to relay a remote signal to a signal processor. OFS are small, require no electrical power at the measurement point, and can be multiplexed to record measurements over large and small distances.

Thanks to advantages such as high sensitivity and resistance to harsh environments, OFS solve many tricky metrological problems, including measurements inside oil wells and jet engines. A growing need for multiple point measurements with characteristic OFS simplicity and suitability for remote sensing networks makes OFS also very interesting for non-industrial applications. OFS are increasingly used for medical diagnoses, therapies, and health monitoring. The market for these sensors is rapidly growing, accompanied by strong support from continuous development of new light sources and measurement techniques. Now that more people rely on OFS than ever before, new ideas and optimized solutions for existing problems are needed.

Ferrule-top (FT) cantilevers are a new generation of all optical micromechanical sensors. They are made by carving microstructures on top of a glass sleeve, or ferrule, that terminates many optical fibers. The structure's movement can be monitored with laser light coupled into the fiber from the opposite end. Using the same principle, it is also possible to excite vibrations in the structure using an additional light source. This unique dual-optical feature makes FT sensors ideal for applications where simplicity and compact design are important. Because of their insensitivity to high electric and magnetic fields, FT cantilevers have attracted interest as alternative tools for accelerometers and optical microphones. The geometry of the sensor can be tailored to the application. However, in most cases the micromechanical element topping the ferrule is a simple beam clamped on one side.

FT sensing is based on optical monitoring of the microstructure's mechanical response to stimuli. The structure is fabricated directly in front of the end-face of the fiber, and as a result, the sensor does not require any alignment, unlike most cantilever-based sensors.The bending resolution of the readout is typically subnanometer, which accommodates the demanding sensitivity requirements of applications such as atomic force microscopy (AFM) measurements. Ferrule-top sensors operate in two different modes: static and dynamic. One can choose the appropriate mode for the particular application or combine the two to get additional information about the measured quantity. Both the static bending and the mechanical frequency respond to changes in one or more parameters, including humidity, velocity, and surface topography. The only limitation is that physical phenomena such as water condensation or viscosity damping can potentially influence the mechanical properties of the sensor.

The FT cantilever is small, robust, and does not require any alignment, which gives the sensor an advantage in harsh environments, be they air, liquid, or vacuum. Its monolithic design and the low thermal expansion coefficient of the ferrule material minimize temperature-induced drifts of the microstructure with respect to the fiber, improving measurement accuracy in applications where temperature variations are present. This feature can be used to build transducers where high thermal stability is important. The unique combination of fully optical readout and excitation gives FT sensors the potential to become a significant sensing platform.

Samenvatting

Optische fiber sensors (OFS) zijn in de wetenschap en industrie de laatste decennia steeds belangrijkere meetinstrumenten geworden. OFS gebruiken een optische vezel als sensor om temperatuur, spanning, druk of andere grootheden te meten, of om het signaal van een remote sensor door te sturen naar een detector. OFS zijn klein, gebruiken geen elektriciteit bij het meetpunt en signalen kunnen worden versterkt om metingen over zowel grote en kleine afstanden mogelijk te maken.

Dankzij de hoge gevoeligheid en robuustheid tegen de elementen, lossen OFS vele metrologische problemen op, zelfs metingen in olie reservoirs van jet motoren zijn mogelijk. Door een groeiend tekort aan multiple point metingen en OFS voor metingen op moeilijk bereikbare plaatsen maken OFSs ook heel geschikt voor de particuliere markt. Daarnaast worden OFSs steeds meer gebruikt voor medische toepassingen voor het stellen van diagnoses, ondersteuning bij therapien en continue gezondheidsmonitoring. Nu steeds meer mensen vertrouwen hebben in OFS, is er ruimte om nieuwe ideen en oplossingen voor bestaande vraagstukken te ontwikkelen.

Ferrule-top (FT) sensors zijn een nieuwe generatie van geheel optische sensors. Ze worden gemaakt door een microstructuur op het uiteinde van een glazen staafje, een ferrule, te fabriceren. Door de montage van een optische vezel kunnen de beweging van deze cantilever kan worden gemeten doormiddel van een laser die verbonden is met het andere uiteinde van de optische vezel. Door hetzelfde principe te gebruiken is het ook mogelijk om een mechanische frequentie van de structuur aan te slaan met een tweede lichtbron. Deze unieke eigenschap maakt FT sensors ideaal voor toepassingen waar gebruiksgemak en compact ontwerp belangrijk zijn. Doordat ze niet gevoelig zijn voor sterke elektrische of magnetische velden hebben ze de aandacht getrokken als alternatieve versnellingsmeter of een optische microfoon. Het ontwerp kan worden aangepast aan de toepassing, echter heeft het micro mechanische element meestal de vorm van een rechthoekige cantilever.

FT metingen zijn gebaseerd op het optisch monitoren van de mechanische beweging van de cantilever die reageert op stimuli. De structuur is gefixeerd direct voor de optische vezel die de beweging meet, daardoor is het niet nodig om het instrument uit te lijnen zoals bij de meeste cantilever gebaseerde instrumenten het geval is. De buigingsgevoeligheid van de detector is normaal gesproken sub-nanometer, wat voldoet aan de eisen voor veel gebruikte toepassing zoals atoom kracht microscopie (AFM). FT sensors kunnen op twee verschillende manieren worden gebruikt, statisch en dynamisch. Er kan worden gekozen voor een van de twee configuraties, ook kunnen deze twee manieren gecombineerd worden om meer informatie over de te meten grootheid te krijgen. Zowel de statische buiging als de mechanische frequentie reageren op omstandigheden zoals luchtvochtigheid, snelheid of oppervlakte topografie. Het enige nadeel van deze sensor is dat watercondensatie of viscositeit de mechanische eigenschappen van de sensor zouden kunnen benvloeden.

FT cantilevers zijn kleine robuuste meetinstrumenten die niet hoeven te worden uitgelijnd wat ze uitermate geschikt maakt voor uiteenlopende meetomstandigheden als lucht, water en vacum. Het monolithische ontwerp en het materiaal van de ferrule met een heel lage expansie cofficint zorgen ervoor dat de drift door temperatuur veranderingen minimaal blijft, dit verhoogt de meet nauwkeurigheid in omgevingen waar temperatuursveranderingen een rol spelen. Deze eigenschap kan worden gebruikt in toepassingen waar hoge temperatuur stabiliteit belangrijk is. De unieke combinatie van geheel optische detectie en excitatie maakt deze technologie in potentie tot een veelbelovend meetplatform.

Acknowledgment

During four years of my PhD journey through mysteries of physics, optics, electronics and mechanics I have met a lot of exceptional people. Being afraid to omit someone, hereby I would like to cordially thank every one of them for their help, support and ideas:

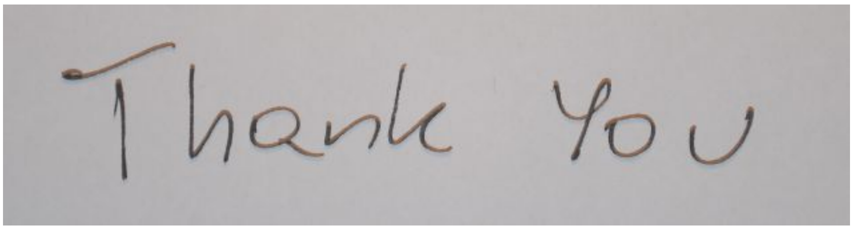

Thank You

Bibliography

[1] D. E. Berylne. A theory of human curiosity. *British Journal of Psychology. General Section*, 45(3):180–191, 1954.

[2] W. Heisenberg. Uber den anschaulichen inhalt der quantentheoretischen kinematik und mechanik. *Zeitschrift fur Physik*, 43(3-4):172–198, 1927.

[3] V. I. Busurin, A. S. Semenov, and N. P. Udalov. Optical and fiber-optic sensors (review). *Soviet Journal of Quantum Electronics*, 15(5):595, 1985.

[4] Otto S. Narayanaswamy, Ramaier; Wolfbeis, editor. *Optical Sensors : Industrial, Environmental and Diagnostic Applications.* Springer Series on Chemical Sensors and Biosensors, 2004.

[5] K. O. Hill, Y. Fujii, D. C. Johnson, and B. S. Kawasaki. Photosensitivity in optical fiber waveguides: Application to reflection filter fabrication. *Applied Physics Letters*, 32(10):647–649, 1978.

[6] D. Iannuzzi, S. Deladi, H. Schreuders, M. Slaman, J.H. Rector, and M.C. Elwenspoek. Fiber-top cantilever: a new generation of micromachined sensors for multipurpose applications. *18th International Optical Fiber Sensor Conference Technical Digest*, TuB2:1–4, 2006.

[7] D. Iannuzzi, S. Deladi, V. J. Gadgil, R. G. P. Sanders, H. Schreuders, and M. C. Elwenspoek. Monolithic fiber-top sensor for critical environments and standard applications. *Applied Physics Letters*, 88(5):053501, 2006.

[8] S. Deladi, D. Iannuzzi, V.J. Gadgil, H. Schreuders, and M.C. Elwenspoek. Carving fiber-top optomechanical transducers from an optical fiber. *Journal of micromechanics and microengineering*, 16:886–889, 2006.

[9] D. Iannuzzi, S. Deladi, J. W. Berenschot, S. de Man, K. Heeck, and M. C. Elwenspoek. Fiber-top atomic force microscope. *Review of Scientific Instruments*, 77(10):106105, 2006.

[10] D. Iannuzzi, S. Deladi, and M. Elwenspoek. Fiber-top cantilevers: A new sensor on the tip of a fiber. *Opticas and Photonics News*, 17(12):39–39, 2006.

[11] D. Iannuzzi, M. Slaman, J.H. Rector, H. Schreuders, S. Deladi, and M.C. Elwenspoek. A fiber-top cantilever for hydrogen detection. *Sensors and Actuators B: Chemical*, 121(2):706–708, 2007.

[12] C.J. Alberts, S. Man de, J.W. Berenschot, V.J. Gadgil, M.C. Elwenspoek, and D. Iannuzzi. Fiber-top refractometer. *Measurement Science and Technology*, 20(3):034005, 2009.

[13] A. A. Said, M. Dugan, S. de Man, and D. Iannuzzi. Carving fiber-top cantilevers with femtosecond laser micromachining. *Journal of Micromechanics and Microengineering*, 18(3):035005, 2008.

[14] A. Petrusis, J. H. Rector, K. Smith, S. de Man, and D. Iannuzzi. The align-and-shine technique for series production of photolithography patterns on optical fibres. *Journal of Micromechanics and Microengineering*, 19(4):047001, 2009.

[15] G. T. A. Kovacs. *Micromachined transducers sourcebook*. McGrawHill, Boston, 1998.

[16] G. Binnig, C. F. Quate, and Ch. Gerber. Atomic force microscope. *Physical Review Letters*, 56:930–933, 1986.

[17] N. V. Lavrik, M. J. Sepaniak, and P. G. Datskos. Cantilever transducers as a platform for chemical and biological sensors. *Review of Scientific Instruments*, 75(7):2229–2253, 2004.

[18] B. N. Johnson and R. Mutharasan. Biosensing using dynamic-mode cantilever sensors: A review. *Biosensors and Bioelectronics*, 32(1):1 – 18, 2012.

[19] L. A. Pinnaduwage, A. Wig, D. L. Hedden, A. Gehl, D. Yi, T. Thundat, and R. T. Lareau. Detection of trinitrotoluene via deflagration on a microcantilever. *Journal of Applied Physics*, 95(10):5871–5875, 2004.

[20] J. Fritz, M. K. Baller, H. P. Lang, H. Rothuizen, P. Vettiger, E. Meyer, H. J. Gntherodt, Ch. Gerber, and J. K. Gimzewski. Translating biomolecular recognition into nanomechanics. *Science*, 288(5464):316–318, 2000.

[21] G. Wu, R. H. Datar, K. M. Hansen, T. Thundat, R. J. Cote, and A. Majumdar. Bioassay of prostate-specific antigen (PSA) using microcantilevers. *Nature Biotechnology*, 19(9):856–860, 2001.

[22] A. Subramanian, P. I. Oden, S. J. Kennel, K. B. Jacobson, R. J. Warmack, T. Thundat, and M. J. Doktycz. Glucose biosensing using an enzyme-coated microcantilever. *Applied Physics Letters*, 81(2):385–387, 2002.

[23] H. Liu, S. Zhang, R. Kathiresan, T. Kobayashi, and C. Lee. Development of piezoelectric microcantilever flow sensor with wind-driven energy harvesting capability. *Applied Physics Letters*, 100(22):223905, 2012.

[24] C. Riesch, E. K. Reichel, F. Keplinger, and B. Jakoby. Characterizing vibrating cantilevers for liquid viscosity and density sensing, 2008.

[25] E. Finot, A. Passian, and T. Thundat. Measurement of mechanical properties of cantilever shaped materials. *Sensors*, 8(5):3497–3541, 2008.

[26] A. Boisen, S. Dohn, S. S. Keller, S. S., and M. Tenje. Cantilever-like micromechanical sensors. *Reports on Progress in Physics*, 74(3):036101, 2011.

[27] R. Raiteri, M. Grattarola, H.-J. Butt, and P. Skladal. Micromechanical cantilever-based biosensors. *Sensors and Actuators B: Chemical*, 79(23):115 – 126, 2001.

[28] J. Fritz. Cantilever biosensors. *Analyst*, 133:855–863, 2008.

[29] G. Gerald Stoney. The tension of metallic films deposited by electrolysis. *Proceedings of the Royal Society of London. Series A*, 82(553):172–175, 1909.

[30] J. Tamayo, J. J. Ruz, V. Pini, P. Kosaka, and M. Calleja. Quantification of the surface stress in microcantilever biosensors: revisiting stoneys equation. *Nanotechnology*, 23(47):475702, 2012.

[31] D. J.Gorman. *Free Vibration Analysis of Beams and Shafts*. Wiley, New York, 1975.

[32] G. Meyer and N. M. Amer. Novel optical approach to atomic force microscopy. *Applied Physics Letters*, 53(12):1045–1047, 1988.

[33] N. P. D'Costa and J. H. Hoh. Calibration of optical lever sensitivity for atomic force microscopy. *Review of Scientific Instruments*, 66(10):5096–5097, 1995.

[34] H. Xie, J. Vitard, S. Haliyo, and S. Regnier. Optical lever calibration in atomic force microscope with a mechanical lever. *Review of Scientific Instruments*, 79(9):096101, 2008.

[35] Y.-J. Rao. Recent progress in fiber-optic extrinsic fabry-perot interferometric sensors. *Optical Fiber Technology*, 12(3):227 – 237, 2006.

[36] E. Hecht. *Optics - 4th edition.* Addison Wesley, 2001.

[37] F.T.S. Yu and S. Yin. *Fiber Optic Sensors.* Marcel Dekker, 2002.

[38] C. Fabry and A. Perot. Sur les franges des lames minces argentees et leur application a la mesure de petites epaisseurs dair. *Annales de chimie et de physique*, 12:459–501, 1897.

[39] C. Fabry and A. Perot. Theorie et applications dune nouvelle methode de spectroscopie interferentielle. *Annales de chimie et de physique*, 16:115, 1899.

[40] B. Yu, D. W. Kim, J. Deng, H. Xiao, and A. Wang. Fiber fabry-perot sensors for detection of partial discharges in power transformers. *Applied Optics*, 42(16):3241–3250, 2003.

[41] C. M. Miller, S. C. Mettler, and I. A. White. *Optical Fiber Splices and Connectors.* Marcel Dekker, New York, 1986.

[42] P. G. Jia and D. H. Wang. Self-calibrated non-contact fibre-optic fabry-perot interferometric vibration displacement sensor system using laser emission frequency modulated phase generated carrier demodulation scheme. *Measurement Science and Technology*, 23(11):115201, 2012.

[43] D. Rugar, H. J. Mamin, and P. Guethner. Improved fiber-optic interferometer for atomic force microscopy. *Applied Physics Letters*, 55(25):2588–2590, 1989.

[44] S. M. Han, H. Benaroya, and T. Wei. Dynamics of transversely vibrating beams using four engineering theories. *Journal of Sound and Vibration*, 225(5):935 – 988, 1999.

[45] http://www.duran group.com and http://www.us.schott.com. 12.2009.

[46] T. Gotszalk, P. Grabiec, and I. W. Rangelow. Calibration and examination of piezoresistive wheatstone bridge cantilevers for scanning probe microscopy. *Ultramicroscopy*, 97:385 – 389, 2003.

[47] E. Radeva, V. Georgiev, L. Spassov, N. Koprinarov, and St. Kanev. Humidity adsorptive properties of thin fullerene layers studied by means of quartz micro-balance. *Sensors and Actuators B: Chemical*, 42(1):11 – 13, 1997.

[48] D. W. Galipeau, P. R. Story, K. A. Vetelino, and R. D. Mileham. Surface acoustic wave microsensors and applications. *Smart Materials and Structures*, 6:658, 1997.

[49] F. Mitschke. Fiber-optic sensor for humidity. *Optics Letters*, 14(17):967–969, 1989.

[50] Z. M. Rittersma, W. J. Zaagman, M. Zetstra, and W. Benecke. A monitoring instrument with capacitive porous silicon humidity sensors. *Smart Materials and Structures*, 9(3):351, 2000.

[51] G. Gruca, S. de Man, M. Slaman, J. H. Rector, and D. Iannuzzi. Ferrule-top micromachined devices: design, fabrication, performance. *Measurement Science and Technology*, 21(9):094033, 2010.

[52] D. Chavan, G. Gruca, S. de Man, M. Slaman, J. H. Rector, K. Heeck, and D. Iannuzzi. Ferrule-top atomic force microscope. *Review of Scientific Instruments*, 81(12):123702, 2010.

[53] P. Zuurbier, S. de Man, G. Gruca, K. Heeck, and D. Iannuzzi. Measurement of the casimir force with a ferrule-top sensor. *New Journal of Physics*, 13(2):023027, 2011.

[54] R. R. Dils. High-temperature optical fiber thermometer. *Journal of Applied Physics*, 54:1198–1201, 1983.

[55] S. J. Mihailov. Fiber bragg grating sensors for harsh environments. *Journal of Sensors*, 12(2):1898–1918, 2012.

[56] M.G Xu, L. Reekie, Y.T. Chow, and J.P. Dakin. Optical in-fibre grating high pressure sensor. *Electronics Letters*, 29:398–399, 1993.

[57] Y. Zhu, K.L. Cooper, G.R. Pickrell, and A. Wang. Miniature fiber-tip pressure sensor for high-temperature applications. *Journal of Lightwave Technology*, 24:861–869, 2006.

[58] J. Rouhet, P. Graindorge, L. Laloux, M. Girault, P. Martin, H.C. Lefevre, and F.X. Desforges. Application of fiber optic sensors to cryogenic spacecraft engines. *SPIE*, 3000:29–36, 1997.

[59] M. El-Sherif, L. Bansal, and J. Yuan. Fiber optic sensors for detection of toxic and biological threats. *Journal of Sensors*, 7:3100–3118, 2007.

[60] A. Stefani, S. Andresen, W. Yuan, N. Herholdt-Rasmussen, and O. Bang. High sensitivity polymer optical fiber-bragg-grating-based accelerometer. *IEEE Photonics Technology Letters*, 24(9):763–765, 2012.

[61] L. Thevenaz. *Advanced Fiber Optics Concepts and Technology.* Lausanne, EFPL Press, 2011.

[62] C. C. Lai, Jacob C. P. Kam, David C. C. Leung, and et al. Development of a fiber-optic sensing system for train vibration and train weight measurements in hong kong. *Journal of Sensors*, 2012:365165, 2012.

[63] F. Pirotte. Optical fibre sensors embedded into technical textile for healthcare. *Proceedings of Textile Trends Berlin*, 2007.

[64] M. Becker, M. Rothhardt, H. Bartelt, and et all. Characterization of fiber bragg grating based sensor array for high resolution manometry. *Proceedings of SPIE*, 8439:843902–5, 2012.

[65] A.G. Mignani and F. Baldini. Biomedical sensors using optical fibres. *Reports on Progress in Physics*, 59:1–28, 1996.

[66] F. Baldini, A. Falai, A.R. De Gaudio, D. Landi, A. Lueger, A. Mencaglia, D. Scherr, and W. Trettnak. Continuous monitoring of gastric carbon dioxide with optical fibres. *Sensors and Actuators B: Chemical*, 90(13):132 – 138, 2003. Proceedings of the 6th European Conference on Optical Chemical Sensors and Biosensors EUROPT(R)ODE VI.

[67] S. Pirozzi. Multi-point force sensor based on crossed optical fibers. *Sensors and Actuators A: Physical*, 183(0):1 – 10, 2012.

[68] A.M. Cao-Paz, J. Marcos-Acevedo, A. Del RioVazquez, C. Martinez-Penalver, A. Lago-Ferreiro, A. Nogueiras-Melandez, and J. Doval-Gandoy. A multi-point sensor based on optical fiber for the measurement of electrolyte density in lead-acid batteries. *Sensors*, 10(4):2587–2608, 2010.

[69] D. S. Greywall. Micromachined optical-interference microphone. *Sensors and Actuators A: Physical*, 75(3):257 – 268, 1999.

[70] H. Bae and M. Yu. Miniature Fabry-Perot pressure sensor created by using uv-molding process with an optical fiber based mold. *Optics Express*, 20(13):14573–14583, 2012.

[71] D. Chavan, D. Andres, and D. Iannuzzi. Note: Ferrule-top atomic force microscope. ii. imaging in tapping mode and at low temperature. *Review of Scientific Instruments*, 82(4):046107, 2011.

[72] B. Tiribilli, G. Margheri, P. Baschieri, C. Menozzi, D. Chavan, and D. Iannuzzi. Fibre-top atomic force microscope probe with optical near-field detection capabilities. *Journal of Microscopy*, 242(1):10–14, 2011.

[73] A. Cipullo, G. Gruca, K. Heeck, F. De Filippis, D. Iannuzzi, A. Minardo, and L. Zeni. Numerical study of a ferrule-top cantilever optical fiber sensor for wind-tunnel applications and comparison with experimental results. *Sensors and Actuators A: Physical*, 178(0):17 – 25, 2012.

[74] L. Schenato, L. Palmieri, G. Gruca, D. Iannuzzi, G. Marcato, A. Pasuto, and A. Galtarossa. Fiber optic sensors for precursory acoustic signals detection in rockfall events. *Journal of the European Optical Society - Rapid publications*, 7(0), 2012.

[75] T. Poczsny, K.Prokopczuk, and A.W. Domaski. Comparison of macrobend seismic optical fiber accelerometer and ferrule-top cantilever fiber sensor for vibration monitoring. *SPIE Photonic Europe*, 8439:84392N–5, 2012.

[76] G. Gruca, J. H. Rector, K Heeck, and D. Iannuzzi. Optical fiber ferrule-top sensor for humidity measurements. *21st International Conference on Optical Fiber Sensors SPIE*, 7753:775358, 2011.

[77] A.V. Churenkov. Photothermal excitation and self-excitation of silicon microresonators. *Sensors and Actuators A: Physical*, 39(2):141 – 148, 1993.

[78] D. Kiracofe, K. Kobayashi, A.Labuda, A. Raman, and H. Yamada. High efficiency laser photothermal excitation of microcantilever vibrations in air and liquids. *Review of Scientific Instruments*, 82(1):013702, 2011.

[79] S. Nishida, D. Kobayashi, H. Kawakatsu, and Y. Nishimori. Photothermal excitation of a single-crystalline silicon cantilever for higher vibration modes in liquid. 27(2):964–968, 2009.

[80] G. Gruca, D. Chavan, A. Cipullo, K. Babaei Gavan, F. De Filippis, A. Minardo, J. Rector, K. Heek, L. Zeni, and D. Iannuzzi. Development of fiber optic ferrule-top cantilevers for sensing and beam-steering applications. *SPIE Optical Sensing and Detection II*, 8439:84390E, 2012.

[81] D. A. Mendels, M. Lowe, A. Cuenat, M. G. Cain, E. Vallejo, D. Ellis, and F. Mendels. Dynamic properties of AFM cantilevers and the calibration of their spring constants. *Journal of Micromechanics and Microengineering*, 16(8):1720, 2006.

[82] S. Barhen. Analytic and numerical modeling of the transient dynamics of a microcantilever sensor. *Physics Letters A*, 372(7):947 – 957, 2008.

[83] T. L. Yeo, T. Sun, and K.T.V. Grattan. Fibre-optic sensor technologies for humidity and moisture measurement. *Sensors and Actuators A: Physical*, 144(2):280 – 295, 2008.

[84] S. F. H. Correia, P. Antunes, E. Pecoraro, P. Lima, H. Varum, L. D. Carlos, R. A. S.Ferreira, and P. S. Anda. Optical fiber relative humidity sensor based on a fbg with a di-ureasil coating. *Sensors*, 12(7):8847–8860, 2012.

[85] L. H. Chen, T. Li, C. C. Chan, R. Menon, P. Balamurali, M. Shaillender, B. Neu, X.M. Ang, P. Zu, W. C. Wong, and K. C. Leong. Chitosan based fiber-optic fabry-perot humidity sensor. *Sensors and Actuators B: Chemical*, 169(0):167 – 172, 2012.

[86] M. Penza and G. Cassano. Relative humidity sensing by PVA-coated dual resonator SAW oscillator. *Sensors and Actuators B: Chemical*, 68(13):300 – 306, 2000.

[87] W. Yuan, L.Khan, D. J. Webb, K. Kalli, H. K. Rasmussen, A. Stefani, and O. Bang. Humidity insensitive topas polymer fiber bragg grating sensor. *Optics Express*, 19(20):19731–19739, 2011.

[88] F. J. Arregui, Z. Ciaurriz, M. Oneca, and I. R. Matias. An experimental study about hydrogels for the fabrication of optical fiber humidity sensors. *Sensors and Actuators B: Chemical*, 96(12):165 – 172, 2003.

[89] X. Wang, B. Li, O. L. Russo, H. T. Roman, K. K. Chin, and K. R. Farmer. Diaphragm design guidelines and an optical pressure sensor based on mems technique. *Microelectronics Journal*, 37(1):50 – 56, 2006.

[90] E. Cibula, S. Pevec, B. Lenardic, E. Pinet, and D. Donlagic. Miniature all-glass robust pressure sensor. *Optics Express*, 17(7):5098–5106, 2009.

[91] H. Ahmad, S.W. Harun, W.Y. Chong, M. Z. Zulkifli, M.M. Thant, Z. Yusof, and P. Poopalan. High-sensitivity pressure sensor using a polymer-embedded fbg. *Microwave and Optical Technology Letters*, 50(1):60–61, 2008.

[92] W. Zhang, F. Li, and Y. Liu. FBG pressure sensor based on the double shell cylinder with temperature compensation. *Measurement*, 42(3):408 – 411, 2009.

[93] O. Pfeiffer, R. Bennewitz, A. Baratoff, E. Meyer, and P. Grütter. Lateral-force measurements in dynamic force microscopy. *Physical Review B*, 65:161403, 2002.

[94] T. Kasai, B. Bhushan, L. Huang, and C. Su. Topography and phase imaging using the torsional resonance mode. *Nanotechnology*, 15(7):731, 2004.

[95] Y. Su, A. Brunnschweiler, A. G. R. Evans, and G. Ensell. Piezoresistive silicon V-AFM cantilevers for high-speed imaging. *Sensors and Actuators A: Physical*, 76:139 – 144, 1999.

[96] G. Schitter, P. Menold, H. F. Knapp, F. Allgower, and A. Stemmer. High performance feedback for fast scanning atomic force microscopes. *Review of Scientific Instruments*, 72(8):3320–3327, 2001.

[97] J. K. H. Hrber and M. J. Miles. Scanning probe evolution in biology. *Science*, 302(5647):1002–1005, 2003.

[98] J. P. Howard-Knight and J. K. Hobbs. Video rate atomic force microscopy using low stiffness, low resonant frequency cantilevers. *Applied Physics Letters*, 93(10):104101, 2008.

[99] R. Pedrak, Tzv. Ivanov, K. Ivanova, T. Gotszalk, N. Abedinov, I. W. Rangelow, K. Edinger, E. Tomerov, T. Schenkel, and P. Hudek. Micromachined atomic force microscopy sensor with integrated piezoresistive sensor and thermal bimorph actuator for high-speed tapping-mode atomic force microscopy phase-imaging in higher eigenmodes. *Journal of Vacuum Science & Technology B: Microelectronics and Nanometer Structures*, 21(6):3102–3107, 2003.

[100] G. Gruca, S. de Man, M. Slaman, J. H. Rector, and D. Iannuzzi. Ferrule-top micromachined devices: a new approach to fibre-top technology. *Proceedings of SPIE*, 7503:750381, 2009.

[101] P. Maivald, H. J. Butt, S. A. C. Gould, C. B. Prater, B. Drake, J. A. Gurley, V. B. Elings, and P. K. Hansma. Using force modulation to image surface elasticities with the atomic force microscope. *Nanotechnology*, 2(2):103, 1991.

[102] http://mesh.dl.sourceforge.net/project/gwyddion/user-guide/2009-11-11/gwyddion-user-guide-en-2009-11-11.pdf.

[103] H. B. G. Casimir. On the attraction between two perfectly conducting plates. *Proc. K. Ned. Akad. Wet.*, 51:793, 1948.

[104] F. Capasso, J. N. Munday, D. Iannuzzi, and H. B. Chan. Casimir forces and quantum electrodynamical torques: Physics and nanomechanics. *IEEE J. Sel. Top. Quantum Electron.*, 13(2):400–414, 2007.

[105] D. Iannuzzi, M. Lisanti, and F. Capasso. Effect of hydrogen-switchable mirrors on the Casimir force. *Proceedings of the National Academy of Sciences U.S.A.*, 101(12):4019–4023, 2004.

[106] M. Lisanti, D. Iannuzzi, and F. Capasso. Observation of the skin-depth effect on the Casimir force between metallic surfaces. *Proceedings of the National Academy of Sciences U.S.A.*, 102(34):11989–11992, 2005.

[107] F. Chen, G. L. Klimchitskaya, V. M. Mostepanenko, and U. Mohideen. Demonstration of the difference in the Casimir force for samples with different charge-carrier densities. *Physical Review Letters*, 97(17):170402, 2006.

[108] F. Chen, G. L. Klimchitskaya, V. M. Mostepanenko, and U. Mohideen. Control of the Casimir force by the modification of dielectric properties with light. *Physical Review B*, 76(3):035338, 2007.

[109] J. N. Munday, F. Capasso, and V. A. Parsegian. Measured long-range repulsive Casimir–Lifshitz forces. *Nature*, 457:170–173, 2009.

[110] S. de Man, K. Heeck, R. J. Wijngaarden, and D. Iannuzzi. Halving the Casimir force with conductive oxides. *Physical Review Letters*, 103(4):040402, 2009.

[111] H. B. Chan, Y. Bao, J. Zou, R. A. Cirelli, F. Klemens, W. M. Mansfield, and C. S. Pai. Measurement of the Casimir force between a gold sphere and a silicon surface with nanoscale trench arrays. *Physical Review Letters*, 101(3):30401, 2008.

[112] G.Torricelli, P. J. van Zwol, O. Shpak, C. Binns, G. Palasantzas, B. J. Kooi, V.B. Svetovoy, and M. Wuttig. Switching Casimir forces with phase-change materials. *Physical Review A*, 82:010101(R), 2010.

[113] S. Lee and W. M. Sigmund. Repulsive van der Waals forces for silica and alumina. *Journal of Colloid and Interface Science*, 243:365, 2001.

[114] V. A. Parsegian. *Van der Waals Forces.* Cambridge University Press, New York, 2006.

[115] S. K. Lamoreaux. Demonstration of the Casimir force in the 0.6 to 6 um range. *Physical Review Letters*, 78(1):5–8, 1997.

[116] W. J. Kim, A. O. Sushkov, D. A. R. Dalvit, and S. K. Lamoreaux. Measurement of the short-range attractive force between Ge plates using a torsion balance. *Physical Review Letters*, 103(6):60401, 2009.

[117] M. Masuda and M. Sasaki. Limits on nonstandard forces in the submicrometer range. *Physical Review Letters*, 102:171101, 2009.

[118] G. Bressi, G. Carugno, R. Onofrio, and G. Ruoso. Measurement of the Casimir force between parallel metallic surfaces. *Physical Review Letters*, 88(4):041804, 2002.

[119] H. B. Chan, V. A. Aksyuk, R. N. Kleiman, D. J. Bishop, and F. Capasso. Quantum mechanical actuation of microelectromechanical systems by the Casimir force. *Science*, 291(5510):1941–1944, 2001.

[120] H. B. Chan, V. A. Aksyuk, R. N. Kleiman, D. J. Bishop, and F. Capasso. Nonlinear micromechanical Casimir oscillator. *Physical Review Letters*, 87(21):211801, 2001.

[121] R. S. Decca, D. Lopez, E. Fischbach, and D. E. Krause. Measurement of the Casimir force between dissimilar metals. *Physical Review Letters*, 91(5):50402, 2003.

[122] U. Mohideen and A. Roy. Precision measurement of the Casimir force from 0.1 to 0.9 μm. *Physical Review Letters*, 81(21):4549–4552, 1998.

[123] G. Jourdan, A. Lambrecht, F. Comin, and J. Chevrier. Quantitative non-contact dynamic Casimir force measurements. *Europhysics Letters*, 85:31001, 2009.

[124] S. de Man, K. Heeck, R. J. Wijngaarden, and D. Iannuzzi. Casimir force experiments in air: Two birds with one stone. *International Journal of Modern Physics A*, 25:2231, 2010.

[125] M. Bao and H. Yang. Squeeze film air damping in mems. *Sensors and Actuators: A. Physical*, 136(1):3–27, 2007.

[126] S. de Man, K. Heeck, R. J. Wijngaarden, and D. Iannuzzi. Halving the Casimir force with conductive oxides. *Physical Review Letters*, 103(4):040402, 2009.

[127] S. de Man, K. Heeck, R. J. Wijngaarden, and D. Iannuzzi. Contact potentials in Casimir force setups: An experimental analysis. *Journal of Vacuum Science and Technology B*, 28(3):C4A25–C4A29, 2010.

[128] E. D. Palik. *Handbook of Optical Constants of Solids.* Academic Press, San Diego, 1998.

[129] A. Lambrecht and S. Reynaud. *European Physical Journal D*, 8:309, 2000.

[130] V. B. Svetovoy, P. J. van Zwol, G. Palasantzas, and J. T. M. De Hosson. Optical properties of gold films and the Casimir force. *Physical Review B*, 77(3):35439, 2008.

[131] S. de Man, K. Heeck, and D. Iannuzzi. Halving the Casimir force with conductive oxides: Experimental details. *Physical Review A*, 82:062512, 2010.

[132] T. Arts, H. Boerrigter, M. Carbonaro, J. M. Charbonnier, G. Degrez, D. Olivari, M. L. Riethmuller, and R. A. Van den Braembussche. *Measurement Techniques in Fluid Dynamics. An introduction.* Von Karman Institute for Fluid Dynamics, 2001.

[133] R. Zhu, P. Liu, X.D. Liu, F.X. Zhang, and Z.Y. Zhou. A low-cost flexible hot-film sensor system for flow sensing and its application to aircraft. *Digest Tech. Papers IEEE MEMS09 Conference*, 1084-6999:527–530, 2009.

[134] A. Cipullo, G. Gruca, K. Heeck, F. De Filippis, D. Iannuzzi, and L. Zeni. Ferrule-top cantilever optical fiber sensor for velocity measurements of low speed air flows. *21st International Conference on Optical Fiber Sensors*, 7753:775340–775340–4, 2011.

[135] S. de Man D. Iannuzzi, G. Gruca. Ferrule-top devices. *US Provisional Application*, US 61/204,541; US 61/302,235; PCT/NL 2010/050569.

[136] M. Born and E. Wolf. *Principles of optics: electromagnetic theory of propagation, interference and diffraction of light.* Cambrigde University Press, 2003.

[137] http://www.duran group.com and http://www.us.schott.com 12.2009.

[138] AIAA. Assessment of experimental uncertainty with application to wind tunnel testing. *AIAA S-071A*, 1999.

[139] S. H. Kim. M. G. Allen C. Song, A. R. Aiyar. Exploitation of aeroelastic effects for drift reduction, in an all-polymer air flow sensor. *Sensors and Actuators A: Physical*, 165:66–72, 2011.

[140] T. H. Erismann and G. Abele, editors. *Dynamics of Rockslides and Rockfalls.* Springer New York, 2001.

[141] D. Amitrano. Rupture by damage accumulation in rocks. *International Journal of Fracture*, 139:369–381, 2006.

[142] G. Manthei, J. Eisenbltter, and T. Spies. *Acoustic Emission in Rock Mechanics Studies in Acoustic Emission - Beyond the Millennium.* Elsevier London, 2000.

[143] N. Rosser, M. Lim, D. Petley, S. Dunning, and R. Allison. Patterns of precursory rockfall prior to slope failure. *Journal of Geophysical Research*, 112:F04014, 2007.

[144] A. Lavrov. The kaiser effect in rocks: principles and stress estimation techniques. *International Journal of Rock Mechanics and Mining Sciences*, 40:151–171, 2003.

[145] N. Dixon, R. Hill, and J. Kavanagh. Acoustic emission monitoring of slope instability: development of an active waveguide system. *Proceedings of the institution of civil engineers-geotechnical engineering*, 156:83–95, 2003.

[146] J. H. Cole, C. Kirkendall, A. Dandridge, G. Cogdell, and T. G. Giallorenzi. *Twenty-five years of interferometric fiber optic acoustic sensors at the Naval Research Laboratory.* 2004.

[147] L. Schenato, L. Palmieri, F. Chiarello, G. Marcato, G. Gruca, T. van de Watering, D. Iannuzzi, A. Pasuto, and A. Galtarossa. Experimental analysis of fiber optic sensor for detection of precursory acoustic signals in rockfall events. *Proceedings to Fotonica 2012 14th Convegno Nazionale delle Tecnologie Fotoniche*, 2012.

[148] L. Schenato, L. Palmieri, L. Vianello, G. Marcato, G. Gruca, T. van de Watering, D. Iannuzzi, A. Pasuto, and A. Galtarossa. Analysis of fiber optic sensor application to precursory acoustic signals detection in rockfall events. *Proceedings to 22nd International Conference on Optical Fiber Sensors, SPIE*, 2012.

[149] K. Kageyama, H. Murayama, K. Uzawa, I. Ohsawa, M. Kanai, Y. Akematsu, K. Nagata, and T. Ogawa. Doppler effect in flexible and expandable light waveguide and development of new fiberoptic vibration/acoustic sensor. *IEEE/OSA J. Lightw. Technol.*, 24:1768–1775, 2006.

[150] S. M. Han, H. Benaroya, and T. Wei. Dynamics of transversely vibrating beams using four engineering theories. *Journal of Sound and Vibration*, 225:935–988, 1999.

[151] F. R. Blom, S. Bouwstra, M. Elwenspoek, and J. H. J. Fluitman. Dependence of the quality factor of micromachined silicon beam resonators on pressure and geometry. *Journal of Vacuum Science and Technology B*, 10:19–26, 1992.

[152] J. Eisenblatter, C. U. Grosse, S. Kppel, J. H. Kurz, E. N. Landis, L. M. Linzer, G. Manthei, M. Ohtsu, B. Schechinger, B. Schechinger, T. Shiotani, and T. Vogel. *Acoustic Emission Testing.* Springer, New York, 2008.

[153] N. Carino. *The impact-echo method: an overview.* American Society of Civil Engineers Washington D.C., 2001.

[154] A. G. Bell. Production of sound by radiant energy. *The Manufacturer and Builder*, 13:156, 1881.

[155] T. H. Maugh. Photoacoustic spectroscopy: New uses for an old technique. *Science*, 188(4183):38–39, 1975.

[156] G. C. Wetsel and F. A. McDonald. Photoacoustic determination of absolute optical absorption coefficient. *Applied Physics Letters*, 30(5):252–254, 1977.

[157] A. Rosencwaig and A. Gersho. Theory of the photoacoustic effect with solids. *Journal of Applied Physics*, 47(1):64–69, 1976.

[158] F. Alan McDonald. Photoacoustic determination of small optical absorption coefficients: extended theory. *Applied Optics*, 18(9):1363–1367, 1979.

[159] F.J.M. Harren, G. Cotti, J. Oomens, and S. te Lintel Hekkert. *Encyclopedia of Analytical Chemistry - Photoacoustic spectroscopy in trace gas monitoring*. John Wiley & Sons Ltd, 2000.

[160] M. W. Sigrist. Trace gas monitoring by laser photoacoustic spectroscopy and related techniques. *Review of Scientific Instruments*, 74(1):486–490, 2003.

[161] J. Kauppinen, K. Wilcken, I. Kauppinen, and V. Koskinen. High sensitivity in gas analysis with photoacoustic detection. *Microchemical Journal*, 76(12):151 – 159, 2004.

[162] J. Breguet, J.P. Pellaux, and N. Gisin. Photoacoustic detection of trace gases with an optical microphone. *Sensors and Actuators A: Physical*, 48(1):29 – 35, 1995.

[163] Q. Wang, J. Wang, L. Li, and Q. Yu. An all-optical photoacoustic spectrometer for trace gas detection. *Sensors and Actuators B: Chemical*, 153(1):214 – 218, 2011.

[164] Y. Cao, W. Jin, H. L. Ho, and J. Ma. Miniature fiber-tip photoacoustic spectrometer for trace gas detection. *Optics Letters*, 38(4):434–436, 2013.

[165] S. Schilt and L. Thevenaz. Wavelength modulation photoacoustic spectroscopy: Theoretical description and experimental results. *Infrared Physics & Technology*, 48(2):154 – 162, 2006.

[166] A. M. Moulin, S. J. O'Shea, R. A. Badley, P. Doyle, and M. E. Welland. Measuring surface-induced conformational changes in proteins. *Langmuir*, 15(26):8776–8779, 1999.

[167] M. K. Baller, H.P. Lang, J. Fritz, Ch. Gerber, J.K. Gimzewski, U. Drechsler, H. Rothuizen, M. Despont, P. Vettiger, F.M. Battiston, J.P. Ramseyer, P. Fornaro, E. Meyer, and H. J. Gantherodt. A cantilever array-based artificial nose. *Ultramicroscopy*, 82(14):1 – 9, 2000.

[168] J. Fritz, M. K. Baller, H. P. Lang, H. Rothuizen, P. Vettiger, E. Meyer, H. J. Gntherodt, Ch. Gerber, and J. K. Gimzewski. Translating biomolecular recognition into nanomechanics. *Science*, 288(5464):316–318, 2000.

[169] J.L. Arlett, E.B. Myers, and M.L. Roukes. Comparative advantages of mechanical biosensors. *Nat Nano*, 6(4):203–215, 2011.

[170] G. Meyer and N. M. Amer. Novel optical approach to atomic force microscopy. *Applied Physics Letters*, 53:1045, 1988.

[171] M. Li, E. B. Myers, H. X. Tang, S. J. Aldridge, H. C. McCaig, J. J. Whiting, R. J. Simonson, N. S. Lewis, and M. L. Roukes. Nanoelectromechanical resonator arrays for ultrafast, gas-phase chromatographic chemical analysis. *Nano Letters*, 10(10):3899–3903, 2010.

[172] G. Shekhawat, Tark, and V. P. Dravid. MOSFET-embedded microcantilevers for measuring deflection in biomolecular sensors. *Science*, 311(5767):1592–1595, 2006.

[173] C. Ma and A.Wang. Optical fiber tip acoustic resonator for hydrogen sensing. *Optics Letters*, 35(12):2043–2045, 2010.

[174] P. S. Waggoner and H.G. Craighead. Micro- and nanomechanical sensors for environmental, chemical, and biological detection. *Lab Chip*, 7:1238–1255, 2007.

[175] K. Babaei Gavan, E. W. J. M. van der Drift, W. J. Venstra, M. R. Zuiddam, and H. S. J. van der Zant. Effect of undercut on the resonant behaviour of silicon nitride cantilevers. *Journal of Micromechanics and Microengineering*, 19(3):035003, 2009.

[176] H. Nasrallah, P.-E.l Mazeran, and O. Noel. Circular mode: A new scanning probe microscopy method for investigating surface properties at constant and continuous scanning velocities. *Review of Scientific Instruments*, 82(11):113703, 2011.

[177] A. G. Onaran, M. Balantekin, W. Lee, W. L. Hughes, B. A. Buchine, R. O. Guldiken, Z. Parlak, C. F. Quate, and F. L. Degertekin. A new atomic force microscope probe with force sensing integrated readout and active tip. *Review of Scientific Instruments*, 77(2):023501, 2006.

[178] M. Dong, S. Husale, and O. Sahin. Determination of protein structural flexibility by microsecond force spectroscopy. *Nature Nanotechnology*, 4(8):514–517, 2009.

[179] T. Pangaribuan, K. Yamada, S. Jiang, H. Ohsawa, and M. Ohtsu. Reproducible fabrication technique of nanometric tip diameter fiber probe for photon scanning tunneling microscope. *Japanese Journal of Applied Physics*, 31(Part 2, No. 9A):L1302–L1304, 1992.

[180] A. Lewis, M. Isaacson, A. Harootunian, and A. Muray. Development of a 500 $\mathring{A}$ spatial resolution light microscope: I. light is efficiently transmitted through /16 diameter apertures. *Ultramicroscopy*, 13(3):227 – 231, 1984.

[181] D. W. Pohl, W. Denk, and M. Lanz. Optical stethoscopy: Image recording with resolution lambda/20. *Applied Physics Letters*, 44(7):651–653, 1984.

[182] H. Xiao, Z. Wei, R. Lockhard, and A. Wang. Absolute sapphire optical fiber sensor for high temperature applications. *Proc. SPIE, Sensors and Controls for Advanced Manufacturing*, SPIE 3201:351, 1997.

[183] D. Kang and W. Chung. Integrated monitoring scheme for a maglev guideway using multiplexed fbg sensor arrays. *NDT & E International*, 42(4):260 – 266, 2009.

[184] C. Sonnenfeld, S. Sulejmani, T. Geernaert, S. Eve, N. Lammens, G. Luyckx, E. Voet, J Degrieck, W. Urbanczyk, P. Mergo, M. Becker, H. Bartelt, F. Berghmans, and H. Thienpont. Microstructured optical fiber sensors embedded in a laminate composite for smart material applications. *Sensors*, 11(3):2566–2579, 2011.

[185] H. Wu, Y. Rao, C. Tang, Y. Wu, and Y. Gong. A novel fbg-based security fence enabling to detect extremely weak intrusion signals from nonequivalent sensor nodes. *Sensors and Actuators A: Physical*, 167(2):548 – 555, 2011. Solid-State Sensors, Actuators and Microsystems Workshop.

[186] M. Zamadar, G. Ghosh, A. Mahendran, M. Minnis, B. Kruft, A. Ghogare, D. Aebisher, and A. Greer. Photosensitizer drug delivery via an optical fiber. *Journal of the American Chemical Society*, 133(20):7882–7891, 2011.

[187] X.D. Wang and O.S. Wolfbeis. Fiber-optic chemical sensors and biosensors (2008-2012). *Analytical Chemistry*, 85(2):487–508, 2013.

[188] G. T. Kanellos, G. Papaioannou, D. Tsiokos, C. Mitrogiannis, G. Nianios, and N. Pleros. Two dimensional polymer-embedded quasi-distributed fbg pressure sensor for biomedical applications. *Optics Express*, 18(1):179–186, 2010.

[189] *Corning SMF-28 http://www.corning.com (03.2012).*

[190] K. Babaei Gavan, J. H. Rector, K. Heeck, D. Chavan, G. Gruca, T. H. Oosterkamp, and D. Iannuzzi. Top-down approach to fiber-top cantilevers. *Optics Letters*, 36(15):2898–2900, Aug 2011.